SLAC-420
SLAC/SSRL 0037
UC-401, 408
(SSRL-M)

X-RAY ABSORPTION SPECTROSCOPIC STUDIES OF THE ACTIVE SITES OF NICKEL-AND COPPER-CONTAINING METALLOPROTEINS

Grace O. Tan

Stanford Linear Accelerator Center
Stanford Synchrotron Radiation Laboratory
Stanford University, Stanford, California 94309

June 1993

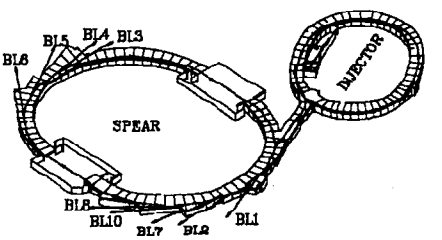

Prepared for the Department of Energy under contract number DE-AC03-76SF00515

Printed in the United States of America. Available from the National Technical Information Service, U.S. Department of Commerce, 5285 Port Royal Road, Springfield, Virginia 22161

---

* Ph.D. thesis

Abstract

X-ray absorption spectroscopy (XAS) is a useful tool for obtaining structural and chemical information about the active sites of metalloproteins and metalloenzymes.

Information may be obtained from both the edge region and the extended X-ray absorption fine structure (EXAFS) or post-edge region of the K-edge X-ray absorption spectrum of a metal center in a compound. The edge contains information about the valence electronic structure of the atom that absorbs the X-rays. It is possible in some systems to infer the redox state of the metal atom in question, as well as the geometry and nature of ligands connected to it, from the features in the edge in a straightforward manner. The EXAFS modulations, being produced by the backscattering of the ejected photoelectron from the atoms surrounding the metal atom, provide, when analyzed, information about the number and type of neighbouring atoms, and the distances at which they occur.

In this thesis, analysis of both the edge and EXAFS regions has been used to gain information about the active sites of various metalloproteins. The metalloproteins studied were plastocyanin (Pc), laccase and nickel carbon monoxide dehydrogenase (Ni CODH). Studies of Cu(I)-imidazole compounds, related to the protein hemocyanin, are also reported here.

Hemocyanin (Hc) is an oxygen transport protein containing two copper atoms in its active site. In oxy Hc (when dioxygen is bound), the EXAFS interaction between the two Cu atoms is readily seen, but in deoxy Hc (no O_2 is bound and both Cu ions are in the Cu(I) state) the Cu–Cu interaction is weak and difficult to distinguish from the strong EXAFS signal produced by imidazole rings (from histidine) ligated to both Cu. Some studies of Cu(I)-imidazole compounds were thus made, with a view towards accurately interpreting the EXAFS spectrum of hemocyanin in the reduced or deoxy state. The crystal structure of Cu(I)(*N*-methylimidazole)$_2$BF$_4$ was solved and is reported here. We also made an attempt to better characterize the EXAFS of Cu-imidazole by relating the EXAFS Debye-Waller factor from spectra of Cu(I)(*N*-methylimidazole)$_4$ClO$_4$ measured over 10–200 K to the vibrational frequencies of the Cu-imidazole interactions. We found that the EXAFS Debye-Waller factor is not determined with sufficient accuracy for us to solve an EXAFS temperature series for a unique value of a bond-stretch frequency or force constant.

Plastocyanin is a small (99-amino acid residue) protein, containing one copper atom, that functions as a electron carrier in the process of photosynthesis. This protein, along with other "blue copper" proteins, is of special interest to inorganic chemists because of its unique spectroscopic features, including an unusually intense blue colour, which arise from

an unusual tetrahedral Cu site, in which Cu is ligated with two histidines (N-ligands), a cysteine and a methionine (S-ligands). Crystal structures of this protein in both the oxidized and reduced states at several pH values have been obtained. These show that the Cu site in the reduced protein undergoes significant structural changes as the pH is varied. Most notably, the Cu–SMet bond, which is 2.90 Å at pH 7.8, shortens to 2.52 Å at pH 3.8. Our work attempted to obtain more accurately the Cu–ligand distances in the reduced protein at high and low pH's by measuring and analyzing EXAFS spectra on frozen solutions of reduced plastocyanin at pH 7.2 and pH 4.8. For both high and low pH, we found two fit minima, and while for both minima 1 S was found at 2.13–2.21 Å, the other S occurred at either 2.3–2.4 Å or greater than 2.7 Å from Cu, and for *both* high and low pH the short Cu–S' minimum fitted as well as or slightly better than the long Cu–S' minimum. This is unlikely to be a true representation of the actual Cu–SMet bond length, and most likely EXAFS is unable to resolve the weak long Cu–S contribution with sufficient accuracy given the quality and range of the data we were able to obtain.

The multicopper oxidases perform the four-electron reduction of dioxygen to water while concomitantly carrying out various other biochemical functions. Laccase is the simplest of the multicopper oxidases, containing four copper atoms, one of Type 1 (T1) copper ("blue copper", similar to the Cu in plastocyanin), one of Type 2 (T2) copper ("normal" copper) and two of Type 3 (T3) copper (in a coupled binuclear site). The T2 and T3 Cu ions occur close to each other, in a triangular array, and are jointly referred to as the trinuclear site. To aid in the elucidation of the complex chemistry of this protein, two derivatives of laccase can be prepared, one by removing the T2 Cu (Type 2-depleted or T2D laccase) and the other by replacing the T1 Cu with Hg (Type 1 Hg or T1Hg laccase). In this work, samples of T2D and T1Hg laccase were fully reduced under anaerobic conditions and then reoxidized by exposure to air. At various time points, aliquots were withdrawn and frozen, and XAS spectra were collected on the frozen samples. The edges of these XAS spectra were analyzed in order to quantitate the total redox state of the Cu in the samples. We were able to conclude that T1Hg laccase is totally oxidized when exposed to air, but in T2D laccase only the T1 Cu is oxidized while the T3 Cu remain reduced. Taken in the context of the known chemistry of laccase, this suggested that the trinuclear site is the minimum site required to perform reduction of dioxygen to water. Some studies of a similar nature on the oxygen intermediate in T1Hg laccase are also reported.

The nickel carbon monoxide dehydrogenase (Ni CODH) in *Rhodospirillum rubrum*, containing 1 Ni, ~8 Fe and ~8 inorganic S, carries out the oxidation of carbon monoxide to carbon dioxide in the presence of a one-electron reductant. It is known that CO binds at the

nickel atom, and EPR studies showed that the Fe atoms occurred as Fe_4S_4-type cubane clusters and that Ni was furthermore probably coupled with the cubane clusters in some way. Some structural possibilities were that Ni occurred in a $NiFe_3S_4$ cubane cluster, or that Ni was ligated to one or two Fe_4S_4 clusters. Ni K and Fe K edges of the oxidized and reduced protein both showed no significant shift in energy with the change in redox state, and thus we concluded that Ni does indeed reside in an electronically delocalized system such as a multinuclear cluster. Using EXAFS analysis, we were able to conclude beyond doubt that Ni was not in a $NiFe_3S_4$ cluster. We were able to fit the data with a weak Fe-wave at ~2.7 Å from Ni, but since S- and N-waves fitted the data equally well, we were not able to confirm the presence of Fe at ~2.7 Å. We also determined that the coordination environment of the nickel atom contained two N/O scatterers at 1.85–1.89 Å and two S-type scatterers at 2.23–2.25 Å. Comparisons of the Ni K edge of Ni CODH with edges of known model compounds showed that the geometry about Ni was intermediate between square-planar and tetrahedral.

Acknowledgements

I can hardly believe that the time has come for me to leave Stanford. I have been here almost seven years, and they have been extremely good years. This is not least because I had the good fortune to join the Hodgson Group.

An integral part of being in the Hodgson Group is the "beam time experience". Oddly enough, I have come to enjoy measuring spectra at the Stanford Synchrotron Radiation Laboratory (SSRL) at all hours of the day or night, for weeks on end. I think it must be because of the camaraderie fostered by the shared enterprise of running a beam line (or two), trying as that can sometimes be. I've also enjoyed the atmosphere of SSRL itself. SSRL is full of wonderful huge machines all humming together, and also lots of wonderful, friendly people who keep the machines going, assist hapless users and somehow carry out their own experiments as well. Science doesn't get more exciting than this! SSRL radiates the feeling of a community of people who really do believe in what they are doing and love doing it, and so it's been a congenial place to work, and I think I'll actually miss it when I'm gone.

I am deeply grateful to my advisor, Prof. Keith Hodgson, for his trust in me and his patient guidance and leadership. Under him, I learned not only the technique of X-ray absorption spectroscopy, but also how to motivate myself and to be responsible for the results of my research. I really value the opportunity he gave me to grow in this way.

I also owe a debt of gratitude to the two "secret weapons" of the Hodgson Group, Drs. Britt Hedman and Pat Frank, who incidentally are also about the nicest people you could get to know. Their inexhaustible stores of knowledge, and willingness to teach, help and encourage me have meant a great deal to me. I especially thank Pat for repeatedly shoring up my confidence in myself as a scientist. He's been a real friend to me, as well as a valued colleague.

I also want to thank the other people of the Hodgson Group : Chrisie Stanfel, David Eliezer, Susan Shadle, Kent Nakagawa, Lingling Chen, Isaac Liu, Tami Westre, Heather Bufford, Kendra Rose and Holly Zhang. It's been a pleasure to know all of them. I wish them all success in completing their degrees and in their careers thereafter! I would also like to remember some members of the group who have already graduated. Jane DeWitt graduated a few months before me, and her example and encouragement were very helpful to me in the final stretch of writing up and preparing to leave. I also greatly enjoyed knowing Trevor Tyson, Soichi Wakatsuki and Uwe Spann while they were here.

I would like to thank my collaborators in the various projects that are described in this thesis. Prof. Thomas Sorrell and Dr. Martha Garrity supplied the Cu(I)-imidazole compounds studied in Chapters 3 and 4. Prof. Hans C. Freeman came all the way from Australia with samples of plastocyanin (Chapter 5), and also brought with him Paul Ellis, whose flair for computer programming has made life easier for all of us. Prof. Edward I. Solomon and his hard-working team (Dr. Jim Cole, Ed Yang, Dr. Pat Clark and Brooke Hemming) provided the many laccase samples studied in Chapter 6. And Prof. Paul Ludden, Dr. Scott Ensign and Jeff Fox supplied the samples of Ni CODH for the study in Chapter 7. Several crucial Ni model compounds for this study were supplied by Prof. Richard H. Holm.

My time at Stanford has been important to me not only for the things I have learned about Chemistry and science. I have had such fun learning ballroom dancing from Robin Rebello, together with thoroughly nice people, especially Joe Kahn. I have also had the rich joy of singing great choral works with the Stanford Symphonic Choir under the batons of Profs. William Ramsey and Gregory Wait. There's nothing quite like the thrill of launching into the "Ode to Joy" at the end of Beethoven's 9th Symphony, together with 200 other voices and 100 orchestral instruments.

But best of all has been the joy of getting to know my God and Creator more intimately. In the Chemistry Department, I have had a true sister in Christ in Cynthia Jesudason, and also Christian brothers in Will Watkins, Jon Stocker and Tom Schoch. Many friends at Peninsula Bible Church have encouraged me and taught me how to live joyfully and richly as I walk with Christ and grow in Him. Doug Goins, Chip and Frederica Stearns, Greg Donoho, Steve and Erica Lawry, and Dick and Carol Haines are particularly dear to me for their faithfulness not only in encouraging and advising me, but also in generously giving of their time and resources when I really needed them. I also have many dear friends in the Chinese Christian Fellowship at Stanford, who taught me what it means to be in the family of God. Truly, they have been to me a family away from my family, and a home away from home. With them I have also learned the joy of giving back what I have received from them, in encouragement and practical help. I would particularly like to acknowledge June Loh, who for four years was the best house-mate I could ever have asked for, and who has been a wonderful sister and friend to me. Also Charmaine Wang, my house-mate this year, another dear sister in Christ.

As I think about my time at Stanford, I also want to remember my family in Singapore, who little knew when they sent me off how long I would be gone! I really want to thank them, especially my parents, Dr. N. C. Tan and Dr. Dixie Tan, and also my sister

Jacinta Lim (like me newly a doctor, albeit a medical one) for loving me from beginning to end, and supporting me in such a long absence from home.

Above and beyond all the wonderful people I have come to know at Stanford, and the rich and unforgettable experiences that I have shared with them, is the LORD God, Who has given me all of them. He brought me here, and stayed with me and guarded me as I got to know a strange and beautiful new country and a culture less familiar than it seemed. I knew no-one when I came, but He gave me better friends here than I have ever had before. Most of all, He gave me Himself. In all ways I have been loved and given so much more than I can ever repay. Now it is time for me to leave, and while I must leave all the wonderful people and places that I have come to know here, I know that the Lord will look after me just as wonderfully well wherever He may take me next.

All the way my Saviour leads me,
What have I to ask beside?
Can I doubt His tender mercy,
Who through life has been my guide?
Heavenly peace, divinest comfort,
Here by faith in Him to dwell!
For I know, whatever befall me,
Jesus doeth all things well.

Table of Contents

List of Tables

Chapter 3

Chapter 4

Chapter 5

Chapter 6

Chapter 7

List of Figures

Chapter 2

Chapter 3

Chapter 4

Chapter 5

Chapter 6

Chapter 7

Chapter 1

Introduction

(A) The Scope and Organization of this Thesis

This thesis presents results of a portion of the experiments in which I have been involved for the past six years. Except for the crystal structure reported in Chapter 3, all of these experiments utilized X-ray absorption spectroscopy (XAS) to extract structural and, to a lesser extent, chemical information about metalloproteins. The information was extracted by empirical comparison with small-molecule complexes of known structure (either direct visual comparison (for edges, *vide infra*) or curvefitting using empirical parameters extracted from known compounds (for EXAFS, *vide infra*), rather than through simulation of the XAS spectra by *ab initio* calculations. As such, there is also considerable discussion of the XAS spectra of these "model" compounds.

Chapter 2 gives an introduction to the technique of X-ray absorption spectroscopy. It explains in brief how it occurs, how the XAS data are measured, and how the data are analyzed. It is not possible to give a complete account of the technique in the space of one chapter, but hopefully sufficient background has been provided to render the rest of the thesis intelligible without recourse to outside references.

All the experiments described were undertaken in the context of continuing research into the chemistry of the metalloproteins studied by various methods. Since four different metalloprotein systems were studied, background information on the respective proteins (their chemistry and, where relevant, results from XAS studies undertaken by others) is briefly described at the beginning of the chapters dealing with results of XAS studies on them, rather than in this introduction. Once again, these reviews are not exhaustive, aiming only to provide a context for evaluation of the results discussed in that chapter.

Information from XAS studies may be subdivided into two major categories : information from the edge region, and information from the extended X-ray absorption fine structure (EXAFS) or post-edge region of the spectrum of a metal center in a compound. The edge region contains information about the valence electronic structure of the atom that absorbs the X-rays and so yields information of a chemical nature about the metal atom. On the other hand, the EXAFS region can yield metrical information about the environment of the metal atom, giving the number, type and distances of atoms surrounding the metal atom in question. Analyses in both categories are reported in this thesis.

Some portions of this thesis, as indicated by the references following, have already been published. Other portions, in particular most of Chapter 7, will be published soon. Chapters 3 and 4 describe crystallographic[1] and EXAFS studies undertaken on Cu(I)-imidazole compounds. These compounds were studied as models for the binuclear copper

protein hemocyanin. Chapter 5 describes an EXAFS study of poplar (*Populus nigra*, var. *italica*) plastocyanin, a small protein containing one copper atom. Chapter 6 describes some edge studies[2] of Japanese lacquer tree (*Rhus vernicifera*) laccase, which contains four copper atoms. Chapter 7 reports an extensive edge and EXAFS study[3] of the nickel site of *Rhodospirillum rubrum* (a photosynthetic bacterium) nickel carbon monoxide dehydrogenase (Ni CODH).

(B) The Usefulness of X-ray Absorption Spectroscopy in the Study of Metalloproteins

X-ray absorption spectroscopy provides information of a nature complementary to that from more widely used spectroscopic techniques such as UV-visible or EPR spectroscopy. Since it is an absorption spectroscopy, rather than a diffraction or scattering technique, it can also be performed on compounds in any physical state, whether crystalline, amorphous, in solution, in membranes, bound to a surface or even gaseous. For proteins, X-ray absorption spectra are usually measured on solutions.

Features in the XAS edge can be interpreted as bound-state electronic transitions, in a manner analogous to those in optical spectroscopy. However, since the transitions are from the core electron orbitals to the valence orbitals, rather than within the valence shell, different selection rules apply. For example, Cu(I), which is difficult to probe spectroscopically because of its filled 3d shell ($3d^{10}$), displays $1s \rightarrow 4p$ transitions which are easily interpreted for geometrical and electronic structural information (see Chapter 6).

EXAFS spectroscopy is one of the few techniques that directly yields metrical details (distances and numbers of atoms) about compounds being studied. As such, its value is obvious in the study of systems which cannot be, or have not yet been, crystallized for study by X-ray crystallography. Even for proteins for which the crystal structure has been solved, EXAFS analysis still has a contribution to make.

Protein crystallography gives a three-dimensional structure of the whole protein molecule. However, since the protein molecule is often extremely large, the accuracy with which it can do this is often limited. Interatomic distances are known with accuracies of 0.05 Å at best[4] for small proteins (such as plastocyanin). For large proteins (such as hemocyanin), the accuracy is considerably worse, being typically about ±0.2–0.4 Å.[5,6] Also, it can be hard to detect the presence of small moieties bound to the active site, such as water molecules or hydroxide ions, by crystallography, especially with lower resolution data.

On the other hand, EXAFS spectra give information only about the local environment for atoms of a specific type within a protein. If metal atoms of different types occur in a

protein (e.g. Ni and Fe in Ni CODH), XAS can be performed at different energies to give information on the environment around first one type of atom (say, Ni), then the other (say, Fe). Interatomic distances of up to about 4 Å from the metal atom (in protein systems) can be determined to an accuracy of ±0.03 Å or better.[7-9] This improvement in accuracy makes a great difference in the ability to understand and make models for the reactions at the active site of a protein. The numbers of atoms around the metal atom absorbing the X-rays can generally be determined with an accuracy of about 25%.[7-9] This also is often sufficient to resolve details that protein crystallography cannot. Chapter 5 reports work in which EXAFS spectroscopy was used on a protein for which the structure has already been determined by X-ray crystallography.

EXAFS spectroscopy is, however, limited in that where two or more atoms of the same type are found, it will give information about the averaged environment for all of them, regardless of their individual redox states or chemical environments. Also, whereas crystallography produces a three-dimensional structure, EXAFS spectroscopy on proteins in solution yields only one-dimensional information, simply giving the radial distance from the origin atom at which other atoms occur without giving any indication of the angles between them. Thus, if several different types of atoms occur at nearly the same distance from the origin atom, EXAFS analysis may not be able to resolve their positions. It also gives no direct information about the geometry around the origin atom, though it may be combined with observations made about the edge region to infer geometrical information. (This is done in Chapter 7.) Geometrical information can, however, be directly obtained if polarized EXAFS spectroscopy is performed on protein crystals.

X-ray absorption spectroscopy therefore occupies a unique place in the set of tools that we may bring to bear on a problem of chemistry. It is furthermore a relatively young technique, having been used to provide structural information for only about the past twenty years, and its full potential as a tool for structural analysis is still being explored. For example, analysis of multiple-scattering EXAFS interactions, besides obtaining more accurate distance information, can provide information about the angular distribution of the other atoms around the atom absorbing the X-rays. This technique is not yet fully reliable when applied to systems as complicated as proteins, but it is still evolving. This thesis does not include multiple-scattering analyses, but otherwise provides ample demonstration of both the strengths and limitations of X-ray absorption spectroscopy in its current state when applied to extract information about metalloproteins.

References

(1) Tan, G. O.; Hodgson, K. O.; Hedman, B.; Clark, G. R.; Garrity, M. L.; Sorrell, T. N. *Acta Cryst.* **1990**, *C46*, 1773-1775.

(2) Cole, J. L.; Tan, G. O.; Yang, E. K.; Hodgson, K. O.; Solomon, E. I. *J. Am. Chem. Soc.* **1990**, *112*, 2243-2249.

(3) Tan, G. O.; Ensign, S. A.; Ciurli, S.; Scott, M. J.; Hedman, B.; Holm, R. H.; Ludden, P. W.; Korszun, Z. R.; Stephens, P. J.; Hodgson, K. O. *Proc. Natl. Acad. Sci. USA* **1992**, *89*, 4427-4431.

(4) Guss, J. M.; Bartunik, H. D.; Freeman, H. C. *Acta Cryst.* **1992**, *B48*, 790-811.

(5) Magnus, K.; Ton-That, H. *J. Inorg. Biochem.* **1992**, *47*, 20.

(6) Volbeda, A.; Hol, W. G. J. *J. Mol. Biol.* **1989**, *209*, 249-279.

(7) Cramer, S. P.; Hodgson, K. O. *Prog. Inorg. Chem.* **1979**, *25*, 1-39.

(8) Cramer, S. P.; Hodgson, K. O.; Stiefel, E. I.; Newton, W. E. *J. Am. Chem. Soc.* **1978**, *100*, 2748-2761.

(9) Scott, R. A. *Methods Enzymol.* **1985**, *117*, 414-459.

Chapter 2

Methodology of X-ray Absorption Spectroscopy — Data Collection, Reduction and Analysis

(A) What is X-ray Absorption Spectroscopy?

X-ray absorption spectroscopy (XAS) involves the measurement of the absorption coefficient μ of a compound of interest as a function of energy. However, instead of probing the transitions among partially filled orbitals, X-rays have high enough energy (measured in eV) to excite electrons out of completely filled inner shell orbitals. An X-ray absorption spectrum has a general decreasing trend, interrupted by sharp upward steps (Figure 2.1(a)). These sharp rises in absorption, referred to as "edges", are observed when the monochromatized X-ray beam has an energy equal to or greater than the ionization energy of an electron being excited. Edges are labelled according to the orbital from which the electron has been excited, e.g. a Cu K edge refers to the excitation of an electron from the innermost (K) shell of Cu. Immediately after an edge, the absorption manifests a series of oscillations, or fine structure, of decreasing amplitude (Figure 2.1(b)). This region of the spectrum is called the extended X-ray absorption fine structure, or EXAFS, region. The region of the spectrum just before an edge is referred to as the pre-edge region.

(1) Information From Studying XAS Edges

If the "edge" is examined with good energy resolution, features within the "edge jump" can be discerned (Figure 2.1(c)), and these can be interpreted in terms of bound-state transitions. In particular, in K edge XAS on first-row transition metal systems, these "edge features" can be interpreted in terms of the promotion of a 1s electron to the partially filled 3d orbitals and vacant 4p orbitals, and so the appearance of the edge contains information about the valence electronic structure of the compound. The edge is thus a valuable tool for probing the geometry, oxidation state or nature of ligands for a sample in which these are not known. In some cases, ligand field arguments can be used to correlate features in the edge to the geometry of the compound in a straightforward manner. For example, the spike at ~8337 eV in Figure 2.1(c) indicates that the compound is a square-planar nickel compound. Work done along these lines in this thesis can be found in Chapter 6, Section (A.2) and Chapter 7, Sections (B.1) and (D.1) – (D.2).

(2) Information From Analyzing the EXAFS Region

The EXAFS region occurs at energies just above the edge. At these energies, the photoelectron escapes from the absorbing atom into the continuum. The photoelectron wave then scatters off neighbouring atoms and some of it returns to the absorbing atom, interfering with the outgoing wave and modulating the absorption μ of the compound. Thus, the EXAFS region contains information about the atoms surrounding the absorbing atom — the number of neighbours, the types of atoms and the distances at which they

occur.[1,2] The manner in which this information is encoded is explained in greater detail in the next section, and the manner in which the information is extracted is explained in the section after that.

(B) Interpreting EXAFS Spectra

(1) The EXAFS Equation

The photoelectron ejected from the atom absorbing the X-rays may be pictured as a spherical wave propagating outwards from the origin (Figure 2.2). This spherical wave impinges upon the atoms surrounding the absorbing atom and some of the wave is scattered back to the absorbing atom. (Hence, the neighbouring atoms are sometimes referred to as "scattering atoms" or "scatterers".) The energy of the ejected electron increases with the energy of the incident X-rays, and the wavelength of the photoelectron becomes shorter as we scan to higher energies. Thus the backscattered waves oscillate between constructive and destructive interference with the outgoing electron wave at the absorbing atom (Figures 2.2 (a) and (b) respectively), and we observe the sinusoidal modulations of the absorption spectrum that are characteristic of EXAFS.[1,2]

The amplitude of the EXAFS signal depends on the number and size (in terms of electron density) of scatterers, and the phase of the signal depends both on the types of the scatterers and the distance from the absorbing atom at which they occur. These relations are expressed in the EXAFS equation.[3] For the case where the outgoing wave is scattered only once before returning to the absorbing atom (called "single scattering"), the EXAFS equation takes the following form :

$$\chi(k) = \sum_s N_S \frac{|f_s(\pi,k)|}{kR_{as}^2} \exp(-2\sigma_{as}^2 k^2) \exp\left(\frac{-2R_{as}}{\lambda}\right) \sin[2kR_{as} + \alpha_{as}(k)] \quad \text{.....(2.1)}$$

where N_S is the number of scattering atoms of type S at an average distance R_{as} from the absorbing atom. $|f_S(\pi,k)|$ is the backscattering amplitude and $\alpha_{as}(k)$ is the phase shift of the scattering atom; both are dependent on backscattering atom type. λ is the mean free path which accounts for the finite lifetime of the photoelectron, and k is the photoelectron vector, explained below. The Debye-Waller factor, $\exp(-2\sigma^2_{as}k^2)$, accounts for thermal and structural disorder in a given coordination sphere, with σ^2_{as} defined as the root-means-square variation of atomic distances from the average R_{as}.

The EXAFS for any absorbing atom/scattering atom pair is represented as a damped sine wave with amplitude $\{N_S|f_S(\pi,k)|\exp(-2\sigma^2_{as}k^2)\exp(-2R_{as}/\lambda)]/[k(R^2_{as})]\}$, frequency $(2R_{as})$ and phase shift $(\alpha_{as}(k))$ characteristic of the atoms involved. The total EXAFS is

given by the summation of the individual sine waves which describe each absorbing atom/scattering atom interaction.

As shown above, the EXAFS signal is expressed as a function of k, the photoelectron vector, in units of $Å^{-1}$, but the absorption data are measured as a function of energy (in eV). The relationship between energy and k is given by :

$$k = \sqrt{\frac{2m_e(E - E_0)}{\hbar^2}} \qquad \text{.....(2.2)}$$

where m_e is the electron mass, E is the photon energy (of the incident X-rays), $\hbar$ is Planck's constant divided by 2π, and E_0 is the threshold energy (at which the photoelectron has just sufficient energy to escape the absorbing atom), where k is defined to be zero.

The observed modulation of the absorption coefficent μ is therefore the superposition of the various damped sine waves resulting from the interference of the outgoing photoelectron wave with the wave backscattered from the neighbouring atoms, as measured at the location of the absorbing atom. The types of scattering atoms surrounding the absorbing atom can be recognized by analyzing the EXAFS spectrum for the characteristic amplitude $|f_S(\pi,k)|$ and phase shift ($\alpha_{as}(k)$) , the number of scatterers by analyzing for N_S, and the distances at which the scatterers occur by analyzing for R_{as}.

(2) k-Weighting of EXAFS Data

The amplitude of the EXAFS weakens at higher values of k due to the $1/k$ dependence of the EXAFS expression, and also because of the damping by the exponential Debye-Waller and lifetime limit (mean free path) terms. This damping effect can be compensated for in the data analysis by k-weighting the EXAFS signal $\chi(k)$. Also, the characteristic amplitude $|f_S(\pi,k)|$ for each type of scattering atom has a maximum at some value of k, and this maximum occurs at higher k for heavy scatterers such as metal atoms. Therefore, k-weighting enhances the contribution the the EXAFS from heavier scatterers, and this is particularly desirable for analysis of metalloprotein EXAFS. Another reason to k-weight the EXAFS is that at higher values of k the single-scattering approximation holds more accurately, and so the simple form of the EXAFS equation shown above can be used to analyze the data. Therefore, all the EXAFS analysis reported in this thesis was carried out on EXAFS spectra weighted by k^3. This weighting scheme has proven to be the best compromise, enhancing the data at higher values of k without overemphasizing the increased noise level at higher k.

(3) Phase Shifts and Fourier Transforms

The contribution of each scatterer to the EXAFS can be conveniently visualized by applying a Fourier transform to the k-weighted data. However, the distances at which the Fourier transform peaks appear (denoted R') do not represent accurately the distances between absorber and scatterers. This is because the EXAFS signal for each scatterer includes a k-dependent phase shift ($\alpha_{as}(k)$ in Equation 2.1), which results in a sine-wave frequency of $[2R_{as} + \alpha_{as}(k)/k]$ or $[2R_{as} + a_1]$, shifting the Fourier peak by $a_1/2$ Å. The magnitude of the shift depends on the type of scatterer, but, generally, R' is about 0.4 Å shorter than the true distance R_{as} (which is simply designated R in later chapters).

The Fourier transform is also a valuable tool for separating contributions to the EXAFS at different R_{as} values, so that components of the EXAFS may be isolated and fitted separately, simplifying the analysis.

(4) Limitations of EXAFS Analysis

Since the EXAFS amplitude is proportional to $(R_{as})^2$, the same atom at longer distances would contribute less to the EXAFS than one nearby. Thus EXAFS analysis can only yield structural information within a limited radius of the absorbing atom. Also, in complex environments like those found in metalloproteins, disorder in the scatterer distances results in further reduction of the EXAFS signal, especially at higher k values. The result is that EXAFS on proteins is usually limited to providing information within 4 Å of the absorbing atom. Also, if metal atoms are found in two or more different environments in a metalloprotein, EXAFS will provide structural information averaged over all sites.

The analysis done in this thesis is also limited in that it takes no account of multiple scattering, wherein the outgoing photoelectron wave scatters from more than one neighbouring atom before returning to overlap with the outgoing wave at the origin. This effect is more significant at lower values of k, where the photoelectron may be pictured as travelling more slowly and more apt to be deflected by neighbouring atoms. Thus our EXAFS analysis does not include data below $k = 3$ Å^{-1}. However, even above $k = 3$ Å^{-1} significant multiple scattering occurs in rigid systems, in particular the imidazole ring of histidine, which is known to be a ligand in almost all the proteins studied in this thesis. Work is in progress to characterize the EXAFS of imidazole more accurately, but it is only now reaching a stage where it can be reliably applied to proteins. Bearing all this in mind, however, careful use of the single-scattering paradigm can still produce reliable results from EXAFS analysis.

(C) Details of Methodology — Experiment and Analysis

(1) Data Collection

(a) Sample Preparation

XAS data were collected on two types of samples for this thesis: protein solutions, and solid samples of small-molecule compounds which served as models for the metal environment in the protein.

Model compounds samples were prepared by grinding the solid sample together with boron nitride powder, which was used as a diluent. The uniformly mixed powder was packed into an aluminium spacer, made out of a piece of aluminium 1 mm thick with a slot 4×18 mm^2 in size cut through the thickness. The slot was covered with mylar tape both front and back, so that the sample was held between the tape windows, and the path length of the sample was 1 mm. The amount of sample considered optimum was calculated by estimating the absorption coefficient of the sample above and below the edge, and finding the amount of sample that would produce a significant absorption without decreasing the beam intensity too much.

All protein samples were run as dilute frozen solutions, in lucite or lexan cells with a front face of thin mylar or Kapton tape that allowed X-ray fluorescence to escape. A more concentrated sample gave a larger and less noisy fluorescence signal, but the concentrations achievable were limited by the viscosity of the protein and the tendency to denature above certain concentrations. The quality of data collected was also affected by the homogeneity of the sample. A clear frozen glass was most desirable, but not always achievable. Oftentimes the glass produced had cracks or bubbles in it, both of which increase noise in the fluorescence signal collected. Less often, a sample froze as ice instead of glass. Ice increases the noise in the data collected, and can sometimes produce diffraction peaks and larger background features which completely ruin an EXAFS scan. In order to avoid ice formation, glycerol or glycol was usually added to a sample. Unfortunately, glycerol also produces free radicals in the X-ray beam, which cause photoreduction in some susceptible proteins (such as T1Hg laccase, see Chapter 6).

(b) Synchrotron X-rays

All data were collected using synchrotron radiation, either at the Stanford Synchrotron Radiation Laboratory (SSRL) or at the National Synchrotron Light Source (NSLS) at Brookhaven National Laboratories. The high intensity of synchrotron radiation, especially at wiggler beam lines (which have an order of magnitude more flux than bending

magnet beamlines),[4] makes for better signal to noise in the data, especially when measuring the weak fluorescence signals produced by protein samples.

As produced by the synchrotron ring, synchrotron radiation is broad-spectrum, "white" light. For the purpose of collecting EXAFS spectra, it is normally monochromatized by Bragg diffraction at an angle θ from a crystal :

$$n\lambda = 2d\sin\theta \qquad \text{.....(2.3)}$$

For the data in this thesis, a double crystal monochromator was used. It consists of two silicon crystals mounted parallel so that the beam is diffracted twice, first from one, then from the other, so that the exit beam propagates in the same direction as the incident beam. For a flat crystal monochromator, the energy resolution δE of the monochromatized X-ray beam is given by[5] :

$$\delta E = E\cot\theta\,\delta\theta \qquad \text{.....(2.4)}$$

where θ is the angle for Bragg diffraction from the crystal, and $\delta\theta$ is the angular divergence of the X-ray beam. Sometimes, the [111] planes of the crystal are presented to the beam, and sometimes, the [220] planes are presented. In the latter case, the d-spacing of the lattice is smaller (therefore, for a given energy E or wavelength λ, the Bragg angle θ is larger), and so the monochromatized beam that emerges has a narrower bandpass, and spectra collected using this beam have a higher energy resolution than spectra collected using a Si[111] monochromator. Another factor in the monochromacity of the beam is the degree to which it has been collimated prior to diffraction from the monochromator crystals (represented by $\delta\theta$ in Equation 2.4). Thus, a beam passing through a 1-mm monochromator entrance slit has a higher energy resolution than one passing through a 2-mm slit. δE is also influenced by many other factors, such as the mosaicity of the crystal, which affect the rocking curve of the crystal.

Higher harmonics (at double or triple the energy) in the X-ray beam can be excluded either by using mirrors, which are designed to absorb rather than reflect all radiation above a cutoff energy, or by "detuning" the monochromator, that is, very slightly misaligning one of the two parallel monochromator crystals. The higher harmonics are excluded to a much greater extent than the fundamental because of their much narrower rocking curves. All the samples reported in this thesis were measured with 50% detuning, that is, the incident intensity was reduced 50% by detuning in order to exclude harmonics.

(c) Transmission Mode and Fluorescence Mode

As alluded to above, data were collected in either transmission mode or fluorescence mode (see Figure 2.3). The former was used for model compounds, where the absorption by the metal atom is large relative to the total flux, and the latter for the dilute protein samples, where the edge jump due to the metal atom is small, not only because the sample is dilute, but also in comparison with the total absorption by the large protein molecule. The X-ray fluorescence measured is emitted when electrons in higher orbitals of the absorbing atom descend to fill the vacancy in the 1s orbital.

In both cases, incident and transmitted flux were measured by using ionization chambers filled with flowing N_2 gas (I_0, I_1 and I_2 in Figure 2.3).[6] Internal calibration standards were collected simultaneously with each scan on every sample by placing a thin foil of the appropriate element (copper or nickel) behind the sample, between I_1 and I_2.[7] In transmission mode, the absorption spectrum of the compound is given by $[\ln(I_0/I_1)]$. In fluorescence mode, the spectrum is given by (I_F/I_0), and I_1 and I_2 are required only to measure the calibration standard.

The quality of data collected by fluorescence can be improved by using a more sensitive detector. Two types of detectors were used in collecting protein data. The first was an ionization chamber[8] filled with a flow of argon gas, and equipped with a filter (to exclude fluorescence background at energies below the signal of interest) and a Soller slit, which is a screen of silver vanes in a fanlike pattern (to minimize detection of randomly scattered radiation from sources other than the sample, in particular, fluorescence produced in the filter). This detector was suitable for more concentrated proteins, since it was less apt to reach saturation. For more dilute samples, a 13-element germanium solid-state detector array[9] was used. This detector was more sensitive, and could also be windowed to include only the energies of interest, i.e. the Kα fluorescence from copper or nickel.

(d) Temperature Used for Data Collection

Because the EXAFS signal is damped by thermal disorder in the scatterers (see Equation 2.1), data were collected at as low a sample temperature as possible in order to maximize the EXAFS signal. We used an Oxford Instruments CF1208 continuous-flow liquid helium cryostat with a temperature range of 4–200 K to collect all our data. Most of our EXAFS data were collected at 10 K, for which we reckoned that all atoms would be at or close to zero-point motion.

(e) EXAFS Data Range

When collecting data, every effort was made to collect EXAFS to as high a k value as possible. The greater the k-range of EXAFS data, the more information it contains. A longer k-range allows more accurate determination of scatterer distances, and the possibility of distinguishing scatterers that are at similar distances. For example, data to $k = 15$ Å^{-1} can be used to distinguish two scatterers of the same type with R_{as} differing by 0.1 Å. It also allows a more accurate determination of the number of scatterers N_S, because the effect on the amplitude of the linear term N_S and the exponential terms $\exp(-2\sigma^2_{as}k^2)$ (Debye-Waller factor) and $\exp(-2R_{as}/\lambda)$ (lifetime) can be better distinguished.

However, the range of protein EXAFS data collected is limited by two factors. Firstly, the metalloprotein solution is dilute, and so at a certain value of k the noise overwhelms the EXAFS signal. However, the signal-to-noise ratio in the data can be improved to a certain extent simply by collecting as many scans as time allows (up to 30 or 40) on the sample. In extremely favourable circumstances (a concentrated protein solution and/or a clear glass), data may be collected as far as k ~15 Å^{-1}. More usually, the scan-averaged EXAFS signal can only be traced out as far as k ~12 or 13 Å^{-1}. Secondly, many proteins contain more than one type of metal. In particular, most copper proteins contain some zinc. Thus, when scanning a copper protein, the EXAFS can be seen until the zinc edge is reached, and then the small copper EXAFS signal is swamped by the rising zinc edge, which occurs just above $k = 13$ Å^{-1}.

(2) Data Reduction

Data reduction and analysis were accomplished using the software package XFPAKG.[10]

First, each scan is subjected to a one-point energy calibration. The monochromator motorstep value at which a well-defined feature of the calibration standard (in this case the first inflection point of copper or nickel foil) occurs is set to be equal to a known energy value (8980.3 eV and 8331.6 eV for copper and nickel respectively), and all the other data points are assigned energy values relative to this one point.

The individual scans in a data set are each inspected and then averaged together. Monochromator glitches are then removed if necessary from the averaged data set. This data set is then subjected to background reduction and normalization, allowing the EXAFS to be extracted.

(a) Background Subtraction and Splining

EXAFS ($\chi(k)$) is defined as the modulation of the absorption coefficient, μ, and can be expressed as

$$\chi(k) = (\mu - \mu_0)/\mu_0 \quad \text{.....(2.5)}$$

where μ_0 is the free-atom absorption coefficient which would be observed if the sample contained only the absorbing atom without any neighbouring atoms. In Equation 2.5, the EXAFS modulations are isolated from, and normalized to, the free-atom absorption, effectively yielding information on a per-atom basis. In an XAS experiment, the absorption (or fluorescence) measured consists of the absorption coefficient, μ, plus a background contribution, μ_{back}, arising from absorption from lower Z atoms in the sample and scatter from the sample, as well as absorption by windows, tape or air path. The absorption background μ_{back} decreases monotonically with increasing energy. In principle, the absorption of a blank sample containing everything except the absorbing species of interest should be used to subtract μ_{back}. In practice, it is difficult to create an accurate blank. So μ_{back} is approximated by a polynomial, which is fitted to the data in either the pre-edge or the post-edge region, extrapolated through the rest of the data, and then subtracted. By this method, there is still some residual background, μ_{res}, left in the data, and this is removed in the next step.

The free-atom absorption μ_0 cannot be measured and so must be approximated in some way. Since μ_0 is a smooth curve on which the EXAFS oscillations are superimposed, it can be modelled by a polynomial spline fitted to the data in the post-edge or EXAFS region. This method also removes the residual background μ_{res}. A different value of μ_0 must be used in the denominator of Equation 2.5 because the spline approximation to μ_0 includes μ_{res}. The value of μ_0 used for normalization is usually calculated by using the Victoreen formula.[11]

The determination of μ_0 by the spline curve-fitting method is one of the most subjective parts of EXAFS data analysis. At the border of each spline region, polynomials are constrained to meet with equal value and equal slope. Beyond this, evaluation of a spline is guided by experience and common sense. For data ranges up to k = 15 Å^{-1}, a three-region spline was found to work best, for ranges longer than that a four-region spline was used.

Optimizing the spline involves changing the lengths of the regions and the orders of the polynomials in each region and observing the effect of such changes on the appearance of the spline, of the EXAFS that results after subtraction of the spline and of the Fourier

transform produced from the EXAFS. Care must be taken to insure that the curve used to mimic the background does not distort the resulting EXAFS when it is subtracted. A sound spline should flex with the background but not be susceptible to curving with the EXAFS oscillations. Thus, no spline regions should be made too short or too long (spline regions are usually of roughly equal length in *k*-space), nor should the order of the polynomial in each region be too high (orders 2 and 3 work well). The optimum spline representing $\mu_0+\mu_{res}$ should maximize the intensity of the peaks while minimizing the low-R noise in the Fourier transform, and the amplitude of the EXAFS above and below the zero line should show no ultra-low-frequency structure.

Improper background subtraction can result in errors in the structural information obtained by EXAFS analysis. Distortion of the EXAFS can be manifested as changes in both the frequency and the amplitude of the data, leading to erroneous determinations of distances and coordination numbers.

(b) Normalized Data

All the data discussed in this thesis have been normalized, that is, the edge jump has been scaled to one. The data can be then interpreted on a per atom basis and different samples can be compared with each other. The edge region is sensitive to the chemical environment, and so the point at which the data is scaled must lie above the edge region so that the normalization procedure is independent of the chemical nature of the sample. In practice the data are normalized at E_0, where the continuum begins, and at which $k = 0$ Å^{-1}. In reality, E_0 varies with the effective nuclear charge of each compound, but by convention it is set at 8350 eV for Ni and 9000 eV for Cu in all the work done in this thesis. The scale factor which is used to normalize the data corresponds to the difference between the spline fitted to the postedge region (mimicking μ_0) and the polynomial used to mimic and remove the absorption background μ_{back}, as measured at E_0.

(3) EXAFS Analysis

For each "shell" of scatterers of one type at the same distance, the form of the EXAFS Equation (Equation 2.1) utilized by XFPAKG is :

$$\chi_S(k) = \frac{N_S Scf_S Trf_S}{kR_{as}^2} Amp_S(k)\exp(-2\sigma_{as}^2 k^2)\sin[2kR_{as} + Phs_S(k)] \qquad .....(2.6)$$

where the amplitude factors characteristic of the scatterer *S* are now subsumed into $Amp_S(k)$, and there are two new empirical scaling factors Scf_S and Trf_S. A non-linear least-squares curvefitting algorithm is used to curve-fit the EXAFS data by varying certain parameters in Equation 2.6 in the manner described below.

$Amp_S(k)$ and $Phs_S(k)$ may be provided in a number of ways. They could be obtained by looking up tables of theoretical EXAFS amplitudes and phases. In this case, especially if plane-wave parameters[12] are used, Scf_S and Trf_S have to be varied to scale the theoretical signal to the experimental data. A second option is to extract the amplitude and phase shift as data files from a model compound with a known structure. A third option, and the one used throughout this thesis, is to parameterize $Amp_S(k)$ and $Phs_S(k)$ so :

$$Amp_S(k) = c_0[\exp(c_1 k + c_2 k^2)]k^{c_3} \quad \text{.....(2.7)}$$

$$Phs_S(k) = \frac{a_{-1}}{k} + a_0 + a_1 k + a_2 k^2 \quad \text{.....(2.8)}$$

(a) Fourier Filtering of EXAFS Data

In order to simplify the curve-fitting process, EXAFS "shells" of interest (that is, groups of scatterers occurring at the same distance from the absorbing atom) are isolated by Fourier-transforming the data to produce a Fourier transform of the spectrum with peaks in R-space (in Å), and then applying a Fourier transform again in the reverse direction, using a "Fourier transform window" to include only the peak(s) of interest, and producing a "filtered" EXAFS spectrum in k-space (in $Å^{-1}$) once more, which is then used for EXAFS curve-fitting analysis.

Fourier filtering distorts the data somewhat because of artifacts introduced by truncating the data. These truncation effects can be minimized by using a window smoothing function to taper the data to zero at the minimum and maximum limits of the Fourier transform window. Thus, throughout this thesis, a "Gaussian window" of width 0.1 $Å^{-1}$ (for forward transform from k-space to R-space) or 0.1 Å (for reverse transform) was used. That is, half-Gaussians of the appropriate width were used at both ends of the window to taper the data to zero for Fourier transform.

(b) Extraction of Parameters

The choice of the model compound from which to extract the parameters is critical. The assumption implicit in this method is that the parameters describe a describe a generic absorber/scatterer interaction that is transferable to other compounds. However, this is not always true. Thus, models from which parameters are extracted should bear a reasonable chemical similarity to the unknown system that they will be used to curve-fit. The model compound used for this purpose should have all the scatterers of interest occurring at the same distance from the absorbing atom, and no other atoms occurring at similar distances (within 0.5 Å) from the origin.

The values of c_1 and a_{-1} were always set to zero in the work described in this thesis. Values for the other six parameters were obtained in the following way. The EXAFS signal of interest (e.g. Cu–N) in the EXAFS spectrum of a compound of known structure was isolated by Fourier transform. The EXAFS equation in (2.6) was then used to fit it, with Scf_S and Trf_S being fixed at 1, and N_S and R_{as} fixed at the correct values. Initial values of c_0, c_2, c_3, a_0, a_1 and a_2 were obtained from parameters optimized for a similar absorber-scatterer pair (e.g. parameters optimized for Cu–N interactions were used as initial guesses for Ni–N interactions). The six parameters were then optimized in an iterative manner, with all the phase terms (a's) being varied for the best fit, then all the amplitude terms (c's), then the phase terms again. Two cycles between varying phase and amplitude terms was usually sufficient to produce a fit that was not improved upon further iteration. All six terms were then varied at once, and the resulting values of c_0, c_2, c_3, a_0, a_1 and a_2 — the "extracted parameters" — were saved for further use.

This process was repeated for all the absorber/scatterer interactions we wish to investigate in the EXAFS analysis of data from structurally unknown systems.

Parameters should be extracted from data covering the same k-range and similar Fourier transform ranges as the data for the unknown system, both to minimize truncation artifacts due to the Fourier-filtering technique, and because of the k-dependence of the parameters. Parameters extracted from the "first shell" (i.e. the atoms directly coordinated to the absorbing atom, at ~2 Å) are less reliable if used to fit the "outer shells" (atoms 3 Å or more from the absorbing atom).

(c) Parameterized Curve-Fitting of EXAFS Data

When parameters are used for fitting a compound of unknown structure, the parameters are held fixed, and variables are R_{as}, E_0, N_S and σ_{as}^2. Non-linear least-squares curve-fitting techniques are subject to correlation between variables, especially between R_{as} and E_0 (which affect the phase of the EXAFS) and N_S and σ_{as}^2 (which affect the amplitude). For the empirical method used here, the phase parameters already take the effective nuclear charge into account, and so E_0 is never varied. R_{as} and N_S (called the coordination number CN in later chapters) are varied at the same time, since there is little danger that they would correlate with each other.

Despite the the danger of correlation with N_S, it is necessary to vary σ_{as}^2, since different compounds containing the same absorber/scatterer pairs have bonds of differing length and stiffness, or with a different radial distribution, and so σ_{as}^2 is not transferable. Usually, when N_S is varied together with R_{as}, σ_{as}^2 is held at a fixed value, and vice versa.

Using this technique of curve-fitting on structurally characterized model compounds has yielded distances with an estimated accuracy of ±0.03 Å and coordination numbers with an estimated accuracy of about 25%.[1,2,13] Care must be taken to step through a sufficent range of distances and coordination numbers to identify a global, rather than a local, minimum corresponding to the best fit.

The more shells of scatterers are summed together to fit a given data file, the better the fit that can be achieved. This is always true, since there are always more parameters that can then be varied for a good fit. Therefore, a better fit with more "EXAFS waves" is not necessarily a more meaningful fit to the data. Also, when more waves are used to fit the same data, the danger of correlation of R_{as} with R_{as}', and N_S with N_S', etc. is increased. So the results of multiwave fits have to be examined with particular care to ensure that they make sense physically.

If the EXAFS signal of a compound is extremely complex, and the Fourier transform reveals two or more peaks corresponding to shells of scatterers at different distances, then each peak is windowed and Fourier backtransformed to be curvefitted in isolation with one or two waves. When a good fit has been achieved for each shell, then a wide Fourier window is used to include all the peaks, and all the waves are then combined to fit the data. In a well-behaved fit, the results for the filtered data from combined window should not differ much from the results obtained from fits to each shell in isolation. This procedure works best when the peaks in the Fourier transform are well-separated from each other. If there is overlap of Fourier transform peaks, then fits to isolated peaks will not give trustworthy results. They are still done to give a first approximation of the possible contributions to the EXAFS, but results from fits done to the data from the combined Fourier peaks are often different from the results of fits to isolated peaks.

(d) The Parameter c_2

As can be seen from Equations 2.6 and 2.7, the parameter c_2 occurs in the same functional form as the Debye-Waller factor, i.e, $\exp(xk^2)$, where $x = c_2$ or $x = -2\sigma^2_{as}$. Thus, a value of σ^2_{as} is already included in the value of c_2 in the parameters extracted from the model compound. Because of this, in practice, σ^2_{as} is set to zero and never varied, and c_2 is varied in its place. The absolute value of c_2 (always negative) cannot be directly correlated to σ^2_{as}, but, in comparing results from different sets of data, we may say that $\Delta c_2 = -2\Delta\sigma^2_{as}$. A more negative value of c_2 denotes a larger value of σ^2_{as} and so a weaker bond or a greater distribution of distances for scatterers, and a less negative value of c_2 denotes a stronger or stiffer bond, or else a narrow distribution of scatterer distances. As

will be seen in Chapters 5 and 7, scrutiny of c_2 values is important in the interpretation of fits to EXAFS data.

(e) The Fit Index F

The goodness-of-fit is evaluated by the minimization function value F, which is referred to as the fit index in later chapters.

$$F = \sqrt{\frac{\sum_{i}^{n}[k_i^3(EXAFS_{obs} - EXAFS_{calc})_i]^2}{n}}, \text{where } n = \text{no. of data points } i \quad \text{.....(2.9)}$$

F is thus evaluated over the entire range of data fitted, and it is weighted by k^3 to give due consideration to data at higher values of k. F is not, however, adjusted for the overall amplitude of the signal, so care must be taken when comparing F values for fits made to different data files. For fits made to the same data, a smaller value of F corresponds to a closer match of the calculated fit to the data. However, the closest match is not necessarily the best or most reasonable fit of the data. The distances, coordination numbers and Debye-Waller factors obtained must all also be taken into account in judging the best fit. Examples of the application of such fit criteria are presented in Chapters 5 and 7.

References

(1) Cramer, S. P.; Hodgson, K. O. *Prog. Inorg. Chem.* **1979**, *25*, 1-39.

(2) Scott, R. A. *Methods Enzymol.* **1985**, *117*, 414-459.

(3) Stern, E. A. In *X-ray Absorption: Principles, Applications, Techniques of EXAFS, SEXAFS and XANES*; 1st ed.; D. C. Koningsberger and R. Prins, Ed.; John Wiley and Sons: New York, 1988; Vol. 92; pp 3-51.

(4) Spencer, J. E.; Winick, H. In *Synchrotron Radiation Research*; 1st ed.; H. Winick and S. Doniach, Ed.; Plenum Press: New York, 1980; pp 663-716.

(5) Lee, P. A.; Citrin, P. H.; Eisenberger, P.; Kincaid, B. M. *Rev. Mod. Phys.* **1981**, *53*, 769-806.

(6) Heald, S. H. In *X-ray Absorption: Principles, Applications, Techniques of EXAFS, SEXAFS and XANES*; 1st ed.; D. C. Koningsberger and R. Prins, Ed.; John Wiley and Sons: New York, 1988; Vol. 92; pp 87-118.

(7) Scott, R. A.; Hahn, J. E.; Doniach, S.; Freeman, H. C.; Hodgson, K. O. *J. Am. Chem. Soc.* **1982**, *104*, 5364-5369.

(8) Stern, E. A.; Heald, S. M. *Rev. Sci. Instrum.* **1979**, *50*, 1579-1582.

(9) Cramer, S. P.; Tench, O.; Yocum, M.; George, G. N. *Nucl. Instr. Methods Phys. Res.* **1988**, *A266*, 586-591.

(10) Eccles, T. K. Ph. D. Thesis, Stanford University, 1978.

(11) In *International Tables for X-ray Crystallography, Vol. III*; C. H. MacGillavry and G. D. Rieck, Ed.; Kynoch Press: Birmingham, England, 1968; Vol. III; pp 157-200.

(12) Teo, B.-K.; Lee, P. A. *J. Am. Chem. Soc.* **1979**, *101*, 2815-2832.

(13) Cramer, S. P.; Hodgson, K. O.; Stiefel, E. I.; Newton, W. E. *J. Am. Chem. Soc.* **1978**, *100*, 2748-2761.

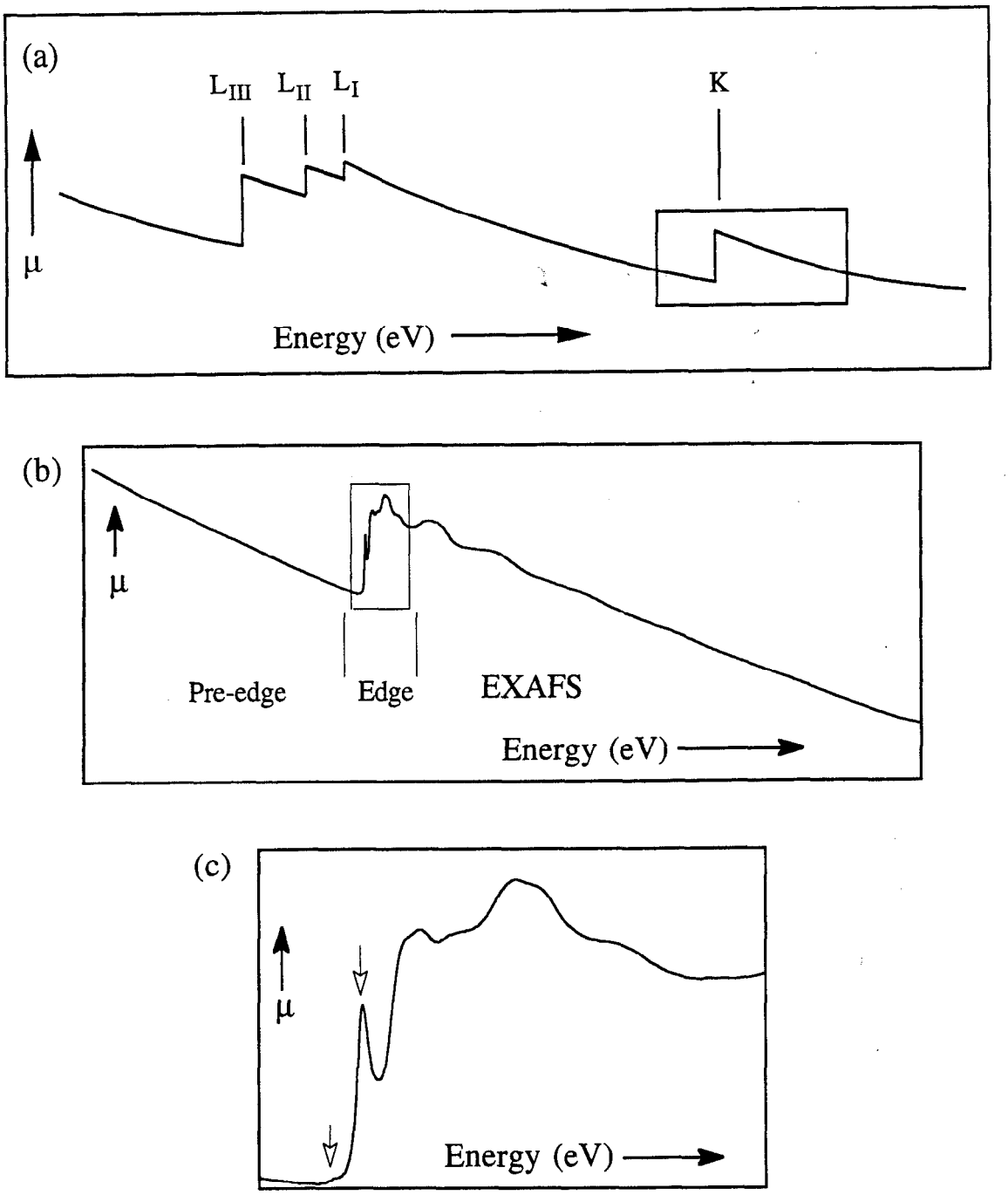

Figure 2.1. A typical X-ray absorption spectrum. (a) Generalized X-ray absorption spectrum, showing the K edge (1s→ continuum) and the L_I–L_{III} edges (2s,2p→continuum). (b) Inset from (a), showing the pre-edge, edge and EXAFS regions for a nickel compound. (c) Inset from (b), showing features in the edge which are diagnostic of a square-planar geometry.

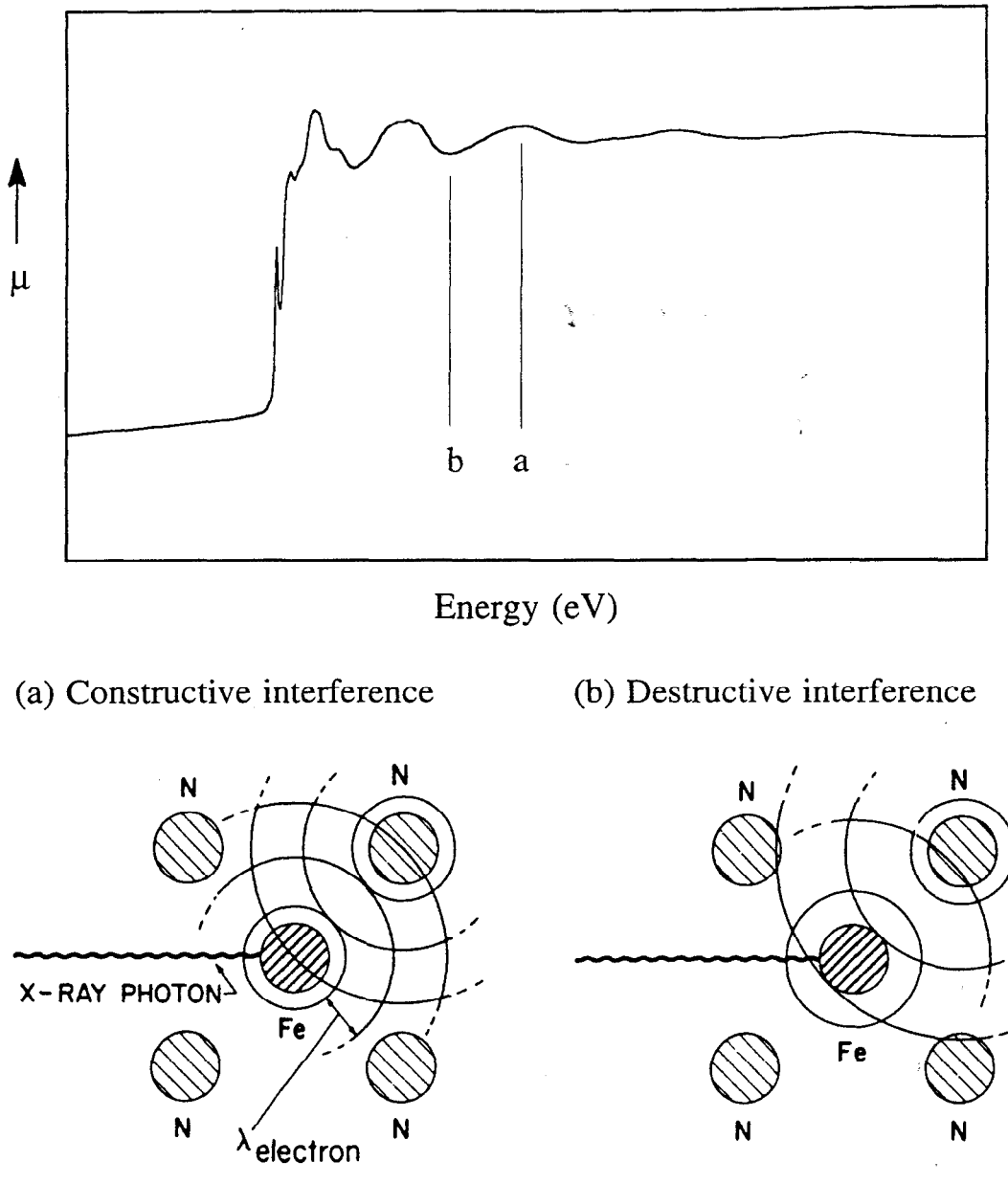

Figure 2.2. EXAFS of a compound where the absorbing atom is surrounded by four equidistant scatterers. (a) At this energy, the spherical photoelectron wave has a wavelength such that the amplitudes of the outgoing wave and of waves scattered back overlap constructively at the origin, producing a maximum in the absorption. (b) At this lower energy, the wavelength of the photoelectron wave is longer, and destructive interference between outgoing and backscattered waves occurs, producing a minimum in the absorption. (Wavefront schematic diagrams reproduced from *Prog. Inorg. Chem.* **1979**, *25*, 1–39, by courtesy of K. O. Hodgson.)

(a) Transmission Mode

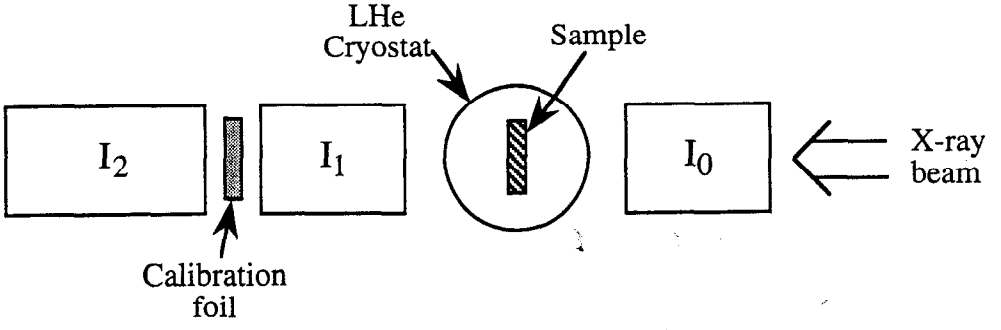

(b) Fluorescence Mode

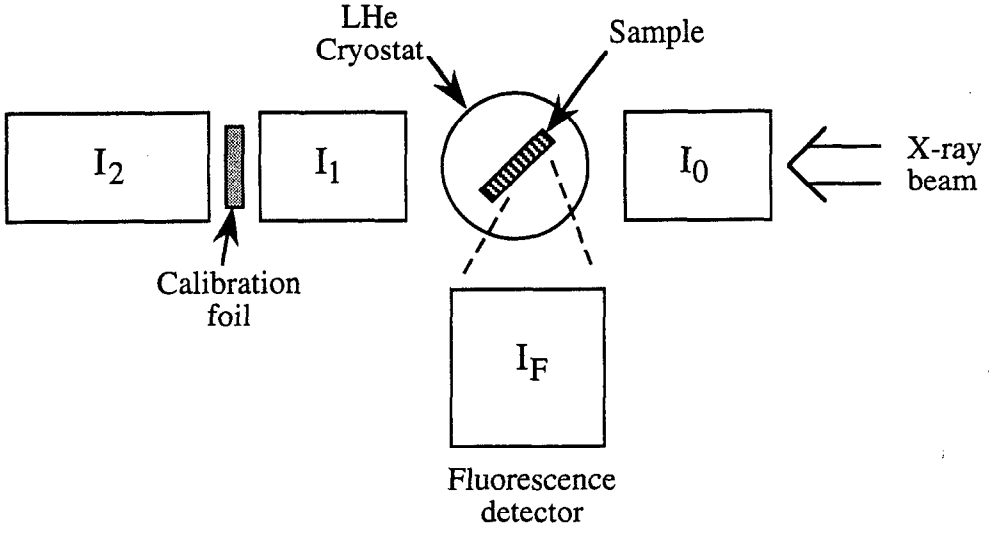

Figure 2.3. Schematic representation of the experimental setup used to collect XAS data in (a) transmission mode, (b) fluorescence mode. I_0, I_1 and I_2 are ionization chambers containing N_2 gas. A potential of 300 V is applied across each chamber. I_F is the fluorescence detector, which may be either an ionization chamber-type detector or a 13-element Ge solid-state array detector. The liquid helium cryostat for the samples has a temperature range of 4–200 K.

Chapter 3

Crystal Structure of

Bis(*N*-methylimidazole)copper(I) Tetrafluoroborate

(A) Relevance of Simple Cu-Imidazole Compounds to Biological Studies

Many vital biological functions (e.g., oxygen transport, electron transport and catalysis of biochemical reactions) are carried out by metalloproteins, that is, proteins or enzymes with one or more metal atoms located within the coils and sheets formed by the peptide sequence which comprise the bulk of the protein. Although these metal atoms occupy a small volume in the protein, their properties readily make them the focus of the function of the metalloprotein, with catalysis, binding or redox action occurring at or through the metal atoms. Thus, the metal atoms and their immediate environment merit particular study. For this purpose, metalloproteins may be thought of as particularly large coordination complexes of metals, which may be approximated by smaller complexes synthesized to model the immediate coordination sphere of the metal atoms. These smaller compounds are useful because they can be characterized with much greater accuracy, particularly by X-ray crystallography, than the large protein molecules.

Histidine is one of the amino acids that is commonly found coordinated to the metal atom in a metalloprotein. In the binuclear copper protein hemocyanin (see Chapter 4) and the trinuclear copper site of laccase (see Chapter 6), histidine is the primary ligand coordinated to the copper atoms. In the mononuclear "blue copper" site, found in plastocyanin (Chapter 5) and also the Type 1 site of laccase (Chapter 6), histidine again accounts for two out of four ligands to the copper atoms.

Histidine coordinates to a metal atom through the imidazole ring, and thus many model compounds have utilized imidazole as a ligand. Some model compounds attempt to mimic the metalloprotein active site in its entirety (e.g., binuclear copper compounds with bridging oxygen ligands to mimic the active site in hemocyanin), while others focus on one aspect of the site, in order to study that aspect in isolation.

Simple Cu-imidazole compounds play an essential role in the EXAFS analysis of copper metalloproteins like hemocyanin and plastocyanin. This is because the rigid imidazole ring produces a strong EXAFS signal that is perceived in Fourier transforms at ~2–4 Å from the metal atom, and there is a need to characterize and understand this complex signal on its own in order to reliably distinguish it from any signals due to other types of ligands, or neighbouring metal atoms within 4 Å, in the protein active site.

In the course of our study of deoxyhemocyanin (see Chapter 4), it became necessary for us to solve the crystal structure of Cu(I)(*N*-methylimidazole)$_2$BF$_4$. The structure we obtained was eventually published in *Acta Crystallographica.* as a short paper.[1]

(B) Experimental Details

Cu(I)(*N*-methylimidazole)$_2$BF$_4$ crystals were provided to us by Professor Thomas N. Sorrell of the University of North Carolina at Chapel Hill. The compound was prepared under an inert atmosphere by treating a solution of *N*-methylimidazole in dry methanol with a half equivalent of solid Cu(CH$_3$CN)$_4$BF$_4$.[2] Colourless parallelepipeds were obtained by slow cooling of a hot ethanol solution of the complex. The density of the crystals was not measured because of their extreme sensitivity to dioxygen.

A crystal measuring approximately $0.50 \times 0.25 \times 0.15$ mm^3 was mounted in a glass capillary and employed to collect X-ray intensity data on a Siemens $P2_1$ diffractometer, using graphite-monochromated Mo $K\overline{\alpha}$ radiation. Some crystal structure data are given in Table 3.1. Unit-cell dimensions were obtained from 50 reflections, with $2.9 < \theta < 18.6°$. There were no systematic absences, and the space group was determined to be $P\overline{1}$ by intensity statistics and satisfactory structure solution and refinement. 2796 unique reflections were collected, with $1.0 < \theta < 27.5°$; $[(\sin\theta)/\lambda]_{max} = 0.6497$ Å^{-1}, and $-10 \le h \le 10$, $-9 \le k \le 9$, $-11 \le l \le 11$. There were 1163 reflections with $I > 3\sigma(I)$. Three intensity standards checked every 50 reflections showed a small decline in intensity (maximum decline was 6%) during data collection; the data were scaled accordingly. Lorentz and polarization corrections were applied, but no absorption corrections were considered necessary for a crystal of this size and composition.

The copper atom was located from a Patterson map. All other non-hydrogen atoms were located from a subsequent difference Fourier map. Hydrogen atoms were included in calculated positions (C–H = 0.96 Å). The program used for F_{obs} refinement was *SHELX*76.[3] Final refinement values were $w = 1.0/[\sigma^2(F) + 2.05 \times 10^{-4}F^2]$ (for 165 parameters), $R = 0.060$, $wR = 0.056$, $S = 2.437$ and $\Delta_{max}/\sigma = 0.03$ for non-hydrogen atoms. In the final difference map, the maximum $\Delta\rho$ excursion was 0.62 e Å^{-3} (near $[BF_4]^-$) and the minimum $\Delta\rho$ was -0.41 e Å^{-3}.

Calculations were performed on a MicroVAX 3600 computer. Diagrams were produced using *ORTEP*II.[4] Atomic scattering factors used were those of Cromer and Mann[5] for F, O, N, C and B, the *International Tables for X-ray Crystallography*[6] for Cu and H, and Cromer and Liberman[7] (for all $\Delta f'$ and $\Delta f''$).

(C) Results and Discussion

Atomic positions are given in Table 3.2, and selected bond lengths and angles are listed in Table 3.3. The molecular geometry and atomic numbering are depicted in Figure 3.1.

Within each cation, the copper atom is nearly linearly coordinated to the two nitrogen donors on the two imidazole groups, with Cu–N(1) = 1.863(7) Å, Cu–N(3) = 1.855(7) Å and N(1)–Cu–N(3) = 173.6(3)°. The imidazole rings are disposed such that the two methyl substituents project to the same side of the molecule, rather than adopting the alternative centrosymmetric arrangement (see Figure 3.1).

This linear geometry contrasts with the geometry of tetrahedral Cu(I)(*N*-methylimidazole)$_4$ClO$_4$,[8] where Cu–N = 2.054(2) Å, but is quite similar to the geometries for other two-coordinated Cu(I)-heteroaromatic compounds. For example, Cu(I)(1-methylpyrazole)$_2^+$ and Cu(I)(1,3,5-trimethylpyrazole)$_2^+$, have Cu–N and N–Cu–N values of 1.873(3) Å, 1.879(3) Å, 178.2(2)° and 1.878(3) Å, 1.863(4) Å, 173.8(2)° respectively,[2] and Cu(I)(2,4-dimethylpyridine)$_2^+$ has Cu–N = 1.86(1) Å and N–Cu–N = 170(1)°.[9]

Each of these four linear complexes shows a different degree of aggregation in the solid state. In Cu(I)(2,4-dimethylpyridine)$_2^+$, there is a weak interaction with the perchlorate counterion (Cu··O = 2.72(4) Å) to form a pseudo three-coordinate structure. In Cu(I)(1,3,5-trimethylpyrazole)$_2^+$, there are no long-range interactions involving the copper atoms. In Cu(I)(1-methylpyrazole)$_2^+$, the flat molecules are partially overlapped in a weak dimeric structure, with copper in each molecule being almost directly opposite the middle of a C–C bond in the molecule that it is paired with (Cu··C(2a') = 3.150(4) Å, Cu··C(3a') = 3.221(4) Å). This is suggestive of a weak metal-π(alkene) type of interaction, giving a pseudo three-coordinated copper.

In the present complex, there is a more pronounced dimeric unit, with Cu··Cu = 3.198(2) Å, and completely overlapping stacked rings (see Figure 3.2). As shown in Figure 3.2, the deviation of the N(1)–Cu–N(3) angle from 180° is probably due at least in part to mutual repulsion between the stacked imidazole rings, indicating that there is indeed some weak Cu–Cu interaction and so a pseudo three-coordinate environment for copper.

References

(1) Tan, G. O.; Hodgson, K. O.; Hedman, B.; Clark, G. R.; Garrity, M. L.; Sorrell, T. N. *Acta Cryst.* **1990**, *C46*, 1773-1775.

(2) Sorrell, T. N.; Jameson, D. L. *J. Am. Chem. Soc.* **1983**, *105*, 6013-6018.

(3) Sheldrick, G. M. *SHELX*76. Program for crystal structure determination : University of Cambridge, England, 1976.

(4) Johnson, C. K. *ORTEP*II. Report ORNL-5138: Oak Ridge National Laboratory, Tennessee, USA, 1976.

(5) Cromer, D. T.; Mann, J. B. *Acta Cryst.* **1968**, *A24*, 321-324.

(6) *International Tables for X-ray Crystallography*; Kynoch Press (Present distributor Kluwer Academic Publishers, Dordrecht): Birmingham, 1974; Vol. IV, pp 99, 149.

(7) Cromer, D. T.; Liberman, D. *J. Chem. Phys.* **1970**, *53*, 1891-1898.

(8) Clegg, W.; Acott, S. R.; Garner, C. D. *Acta Cryst.* **1984**, *C40*, 768-769.

(9) Engelhardt, L. M.; Pakawatchai, C.; White, A. H.; Healy, P. C. *J. Chem. Soc. Dalton Trans.* **1985**, 117-123.

Table 3.1. Crystal data for Cu(I)(*N*-methylimidazole)$_2$BF$_4$

Formula	$C_8H_{12}N_4BF_4Cu$
Space group	$P\bar{1}$
a (Å)	7.811 (2)
b (Å)	8.993 (3)
c (Å)	10.136 (3)
α (°)	77.95 (2)
β (°)	77.91 (2)
γ (°)	72.11 (2)
V (Å^3)	654.5 (3)
Z	2
D_x (g cm^{-3})	1.60
λ(Mo $K\bar{\alpha}$) (Å)	0.71073
μ(Mo $K\bar{\alpha}$) (cm^{-1})	17.71
T (K)	293
Crystal size (mm^3)	0.50 × 0.25 × 0.15
Collection range	$\pm h$, $\pm k$, $\pm l$
	$1.0° < \theta < 27.5°$
	$[(\sin\theta)/\lambda]_{max}$ 0.6497 Å^{-1}
No. of unique reflections	2796
No. of reflections $I > 3\sigma(I)$	1163
$F(000)$	316
$R(F)$	0.060
$wR(F)$	0.056

Table 3.2. Atomic positions and equivalent isotropic displacement factors for non-hydrogen atoms.

$$U_{eq} = \frac{1}{3}\sum_{ij} U_{ij}\, a_i^* a_j^* \mathbf{a}_i.\mathbf{a}_j$$

	x	y	z	U_{eq} (Å^2)
Cu	0.1703(1)	0.0643(1)	0.4235(1)	0.102
N(1)	0.0437(9)	0.2167(9)	0.2968(7)	0.082
N(2)	-0.1326(8)	0.4415(9)	0.2112(8)	0.080
N(3)	0.3097(8)	-0.0711(9)	0.5503(8)	0.087
N(4)	0.4342(11)	-0.1530(13)	0.7377(8)	0.103
C(1)	-0.0493(12)	0.3618(13)	0.3174(8)	0.079
C(2)	0.0156(12)	0.2049(12)	0.1705(10)	0.086
C(3)	-0.0930(11)	0.3421(12)	0.1183(8)	0.079
C(4)	-0.2550(12)	0.6043(11)	0.2016(10)	0.135
C(5)	0.3180(13)	-0.0372(12)	0.6705(12)	0.105
C(6)	0.4255(13)	-0.2189(13)	0.5434(10)	0.100
C(7)	0.5023(12)	-0.2683(13)	0.6585(13)	0.113
C(8)	0.4742(15)	-0.1580(15)	0.8736(10)	0.160
B	-0.1821(21)	0.2783(17)	0.7621(14)	0.119
F(1)	-0.2734(8)	0.3991(7)	0.8329(6)	0.149
F(2)	-0.0535(8)	0.1837(8)	0.8450(8)	0.194
F(3)	-0.2916(8)	0.1832(7)	0.7634(6)	0.167
F(4)	-0.1087(16)	0.3192(12)	0.6448(7)	0.274

Table 3.3. Bond lengths (Å) and angles (°).

Cu–N(1)	1.863(7)	N(4)–C(5)	1.325(11)
Cu–N(3)	1.855(7)	N(4)–C(7)	1.354(11)
N(1)–C(1)	1.320(9)	N(4)–C(8)	1.463(11)
N(1)–C(2)	1.374(10)	C(2)–C(3)	1.340(10)
N(2)–C(1)	1.334(9)	C(6)–C(7)	1.353(11)
N(2)–C(3)	1.357(10)	B–F(1)	1.356(14)
N(2)–C(4)	1.478(10)	B–F(2)	1.404(12)
N(3)–C(5)	1.334(11)	B–F(3)	1.379(14)
N(3)–C(6)	1.365(10)	B–F(4)	1.240(14)

N(1)–Cu–N(3)	173.6(3)	N(1)–C(1)–N(2)	111.2(8)
Cu–N(1)–C(1)	124.6(7)	N(1)–C(2)–C(3)	109.3(8)
Cu–N(1)–C(2)	129.9(8)	N(2)–C(3)–C(2)	106.9(7)
C(1)–N(1)–C(2)	105.3(7)	N(3)–C(5)–N(4)	111.8(9)
C(1)–N(2)–C(3)	107.2(7)	N(3)–C(6)–C(7)	108.2(9)
C(1)–N(2)–C(4)	126.0(9)	N(4)–C(7)–C(6)	108.1(9)
C(3)–N(2)–C(4)	126.7(8)	F(1)–B–F(2)	103.0(9)
Cu–N(3)–C(5)	124.7(8)	F(1)–B–F(3)	110.8(12)
Cu–N(3)–C(6)	129.8(8)	F(1)–B–F(4)	114.7(12)
C(5)–N(3)–C(6)	105.5(8)	F(2)–B–F(3)	103.8(10)
C(5)–N(4)–C(7)	106.4(8)	F(2)–B–F(4)	111.8(14)
C(5)–N(4)–C(8)	126.7(12)	F(3)–B–F(4)	112.0(11)
C(7)–N(4)–C(8)	126.9(11)		

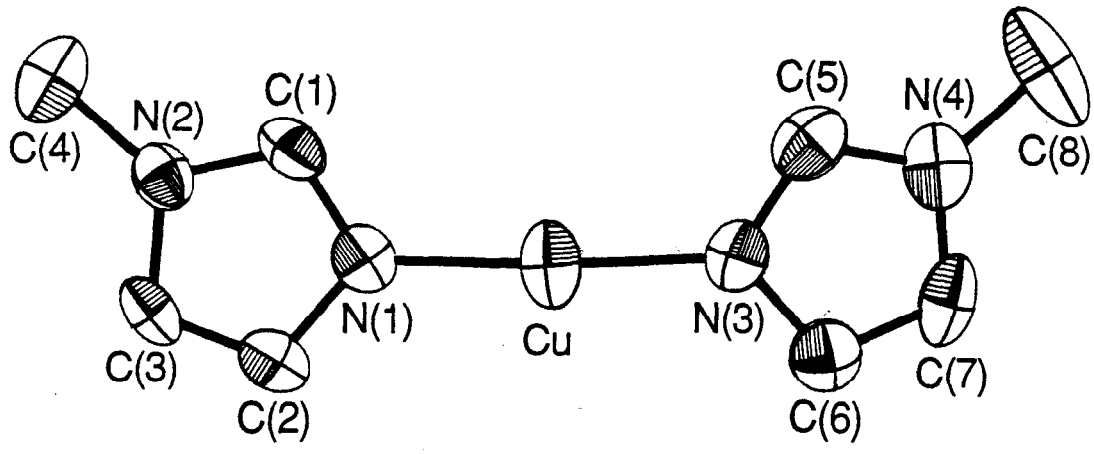

Figure 3.1. Molecular geometry and atomic numbering. Anisotropic ellipsoids represent 33% probability boundaries.

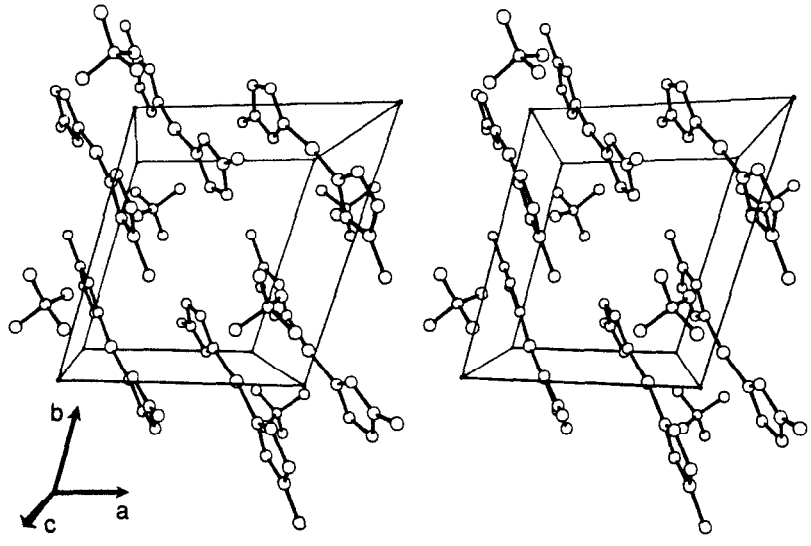

Figure 3.2. Stereographic projection of the unit-cell contents.

Chapter 4

Studies of the EXAFS of a Cu(I)-Imidazole Compound Over a Range of Temperatures

(A) Brief Overview of Hemocyanin Structure

To understand our interest in the EXAFS of Cu-imidazole compounds, we will look briefly at the copper metalloprotein hemocyanin, and at efforts to elucidate structural details of its active site.

Hemocyanin (Hc) is the oxygen transport protein in the blood of molluscs and arthropods.[1-3] Although it corresponds to hemoglobin in its biological function, the structure of its active site is completely different, containing two copper atoms, magnetically coupled to each other,[4] and ligated primarily with histidine.

When dioxygen is bound (this form is called oxyhemocyanin, or oxy Hc), both copper atoms are oxidized, and so the O_2 moiety is bound as a peroxide. However, this blue species is EPR-silent, indicating an antiferromagnetic coupling between the two Cu ($3d^9$) ions. When dioxygen is not bound to the protein (this form is called deoxy Hc), the protein is colourless, and the Cu ions are reduced ($3d^{10}$). This species is of course EPR-silent, and can only be indirectly probed by UV-visible spectroscopy through charge-transfer transitions in binding studies with exogenous ligands such as CO. Optical and EPR methods, while giving insight into the electronic structure of the active site, could not give metrical information. In particular, the distance between the two Cu ions, of vital importance for understanding the chemistry of hemocyanin, could not be ascertained.

Crystal structures have been solved on hexameric deoxy hemocyanin from *Panulirus interruptus* (spiny lobster) at a resolution of 3.2 Å,[5,6] and on oxy hemocyanin from *Limulus polyphemus* (horseshoe crab) at a resolution of 2.4 Å.[7] The crystal structure of deoxy Hc shows the two Cu atoms 2.9–3.8 Å apart, coordinated by six histidine ligands (three on each Cu) arranged in an antiprismatic fashion. Four histidine nitrogens lie in a plane with the two Cu atoms, and for these ligands Cu–N = 1.94–2.26 Å. The remaining two Cu–N(His) bonds, one on each Cu, project in opposite directions from this plane and are extremely weak, being 2.5–2.9 Å long. No ligand bridging the two Cu atoms could be found. Not all details of the oxy Hc structure have been published yet, but it is known that the distance between the two Cu atoms is 3.4 ± 0.2 Å, and that they are bridged by O_2 in an unusual side-on μ-η^2:η^2 configuration to form a planar, symmetrical, Cu–O_2–Cu core, where O–O provides two ligands to *both* the Cu atoms in the site.

.c2.(B) Using EXAFS to Examine the Structure of Hemocyanin — Multiple Scattering by Imidazole

Even though crystal structures have now been solved for both oxy and deoxy Hc, EXAFS spectroscopy is still a valuable means of obtaining more accurate structural

information about the active site. The exact distance between the two copper atoms also remains of particular interest.

In the early 1980's, a number of EXAFS studies on both oxy and deoxy hemocyanin, from various species of molluscs and arthropods, were published.[8-11] In the case of oxy Hc, all studies concurred in finding about four N/O scatterers coordinated to the copper ions (2 N at 2.0 Å and 2 O at 1.9 Å), and an unambiguous Cu–Cu interaction at 3.55–3.68 Å in Hc from all species measured.[8,10,11] However, the EXAFS spectra of deoxy Hc proved to be more difficult to interpret in an unambiguous way. All studies found about two N/O scatterers coordinated to the Cu ions at 1.90–2.00 Å. However, some studies (by Brown, *et al.* and Woolery, *et al.*) found a Cu–Cu interaction (which could also be modelled as a Cu–N interaction) at 3.39–3.48 Å,[8,11] while another study (Co, *et al.*) found no evidence of a Cu–Cu interaction within 4 Å.[9]

Conflicting results were obtained because of the difficulty in accurately accounting for the "outer shell" signal from the histidine imidazoles ligated to Cu. Most ligands display little significant EXAFS signal beyond the first shell. However, imidazole has a characteristic EXAFS signal which is manifested in Fourier transforms as a three-peak group over R = 2–4 Å (Figure 4.3). The significant imidazole EXAFS signal in the region of R = 3–4 Å must be accurately modelled in order to distinguish a weak metal-metal interaction occuring at this distance. Woolery, *et al.* and Co, *et al.* did employ techniques which fitted the EXAFS spectrum of imidazole as a unit. However, it was recognized that these models oversimplified the imidazole signal, taking no account of the multiple-scattering which occurs in imidazole.

The reason the "outer shell" imidazole EXAFS signal is so strong is that multiple-scattering significantly enhances the backscattering from imidazole atoms at 3–4 Å from Cu (see Figure 4.1 and Table 4.1). Thus, an outer shell atom such as C_1 is perceived not only through the single-scattering interaction Cu–C_1–Cu, but through the multiple-scattering interactions Cu–N_1–C_1–Cu (double-scattering) and Cu–N_1–C_1–N_1–Cu (triple-scattering). Multiple-scattering is only significant in rigid moieties such as imidazoles or porphyrin rings because each leg of the scattering path is subject to its own Debye-Waller factor, and so multiple-scattering signals are damped out in less rigid systems. Also, multiple-scattering occurs most strongly if the scattering path is linear, e.g. in Cu–C≡O. As the scattering path deviates from 180°, the amplitude of the multiple-scattering signal diminishes.[12] In Cu-imidazole, there are no linear scattering paths, but the two atoms at ~4 Å (N_2 and C_3 in Figure 4.1) do provide almost-linear scattering paths (e.g. Cu–N_1–N_2–Cu

or Cu–N_1–N_2–N_1–Cu), so that the EXAFS signal from these atoms is considerably enhanced.

Several studies have attempted to take into account multiple-scattering in modelling metal-imidazole EXAFS spectra.[13-16] However, these theoretical simulation methods cannot yet be relied upon to consistently model even compounds of known structure accurately, and they also suffer from having too many parameters that need to be varied for a fit. In particular, no satisfactory way has yet been found to determine Debye-Waller factors for the imidazole ring, and so these have thus far been varied in an entirely empirical fashion to fit the data, even in so-called theoretical simulations.

(C) The Temperature Behaviour of the Debye-Waller Factor as a Tool For Obtaining Physically Meaningful Results From EXAFS Curve-Fitting

In order to constrain at least some EXAFS modelling parameters in a physically meaningful way, there is a need to correlate the EXAFS Debye-Waller factor ($\exp(-2\sigma^2_{as}k^2)$, see Chapter 2) with the actual physical behaviour of the molecule, that is, with factors such as bond stiffness (σ^2_{vib}, vibrational or thermal disorder) and root-mean-square distribution of atom distances (σ^2_{stat}, static disorder).

$$\sigma^2_{as} = \sigma^2_{vib} + \sigma^2_{stat} \qquad \text{.....(4.1)}$$

An idea of the true thermal contribution to the Debye-Waller factor can be obtained from EXAFS data collected on the same compound over a wide range of temperatures. The temperature behaviour of thermal disorder for some types of material (mainly solid-state) has been described by various mathematical models. For solid samples of molecular compounds, it seems best to use the simple harmonic oscillator as an approximate model. The temperature dependence of σ^2_{vib} in this model is then

$$\sigma^2_{vib} = \left(\frac{h}{8\pi^2\mu\nu}\right)\coth\left(\frac{h\nu}{2kT}\right) \qquad \text{.....(4.2)}$$

where h is Planck's constant, ν is the stretching frequency of the bond in question, and reduced mass $\mu = \dfrac{m_1 m_2}{m_1 + m_2}$ in the case of a simplistic diatomic stretch model. For the Cu–imidazole or Cu–methylimidazole stretch, a value for m_1 = 63.5 a.m.u. (for Cu) and m_2 = ~70–80 a.m.u. (for imidazole) may be used to give $\mu \cong 35$ a.m.u. as a reasonable estimate.

For the temperatures at which we are making our study (10–200 K), the static disorder for a given compound should remain much the same, but the vibrational disorder will increase with temperature. Therefore, any change in σ^2_{as} should be due to changes in

σ^2_{vib}, not σ^2_{stat}. In principle, therefore, fits of the EXAFS of the same compound at different temperatures should be able to yield $\sigma^2_{vib}(\Delta T)$, which can then be solved for ν and μ in a known compound, and ν and μ can then be compared with literature values from vibrational (IR and Raman) studies. Once this relation is established, $\sigma^2_{vib}(\Delta T)$ can then be constrained to give a consistent (ν,μ) value in EXAFS curve-fitting of data at different temperatures simultaneously, and ν and μ can be checked to make sure they are reasonable for a given system.

(D) Experimental Details

(1) Preparation of Samples

Cu(I) model compounds were ground with boron nitride and packed into aluminum spacers in the manner described in Chapter 2.

(2) Data Collection

Data for Cu(I) models were collected at the Stanford Synchrotron Radiation Laboratory at the unfocussed 8-pole wiggler beam line 7-3 in transmission mode at 10, 45, 80, 130 and 200 K, using an Oxford Instruments CF1208 continuous-flow liquid helium cryostat, to k = 17 Å^{-1}. For a temperature series on one compound, the cryostat was stepped from one temperature to the other without disturbing the sample.

(3) Data Analysis

Data were reduced and analyzed using XFPAKG, in the manner described in Chapter 2. Scans were calibrated using copper foil as an internal standard, taking the first inflection point of the foil as 8980.3 eV. Subtraction of the background was done by fitting a polynomial to the EXAFS region and then applying this at the bottom of the "edge step" and extending this into the pre-edge region. The same four-region spline to k = 17 Å^{-1} was used for data at all temperatures for one compound. For all data analyzed in this chapter, a data range of k = 3.5–16.5 Å^{-1} was used for the forward Fourier transform (Figure 4.3), and the data were then backtransformed to k = 4–16 Å^{-1} for curvefitting. Parameters were also extracted over the same data ranges.

(E) Results and Discussion

The EXAFS temperature series for Cu(I)(*N*-methylimidazole)$_4$ClO$_4$ was examined. As shown in Figures 4.2 and 4.3, this series displays an extremely regular trend, with EXAFS and FT magnitudes for all features decreasing in a monotonic fashion with increasing temperature. For each of the first (FT window R' = 1.00–2.00 (0.1) Å), second

(R' = 2.10–3.20 (0.1) Å) and third (R' = 3.00–4.10 (0.1) Å) shells, amplitude and phase parameters (c_0, c_2, c_3, a_0, a_1 and a_2) were extracted from the data collected at 10 K in the manner described in Chapter 2. On the principle that only σ^2_{as} should vary as the temperature changed, the parameters were then applied to the data collected at 45, 80, 130 and 200 K and only c_2 was varied (c_2 varies as σ^2_{as}, see Chapter 2). The trend in c_2 with temperature is shown in Table 4.2. At each temperature, after the c_2 result was obtained, R only was then varied to check that the fit was good. For all three shells there was indeed little shift in R with temperature. It is extremely interesting to note that the c_2 values are less negative (i.e., σ^2_{as} is smaller) for the third shell than they are for the second shell. This is consistent with our expectation that multiple-scattering magnitudes are greater for the almost linear paths to the third shell.

An error was made in extracting the parameters at 10 K for the first shell. The phase parameter a_{-1} was not set to zero when the other three phase parameters (a_0, a_1 and a_2, see Chapter 2) were varied. However, since the phase parameters and the amplitude parameters (including c_2) do not interact much, and the values of all phase parameters were the same for fits to data at all temperatures, this should not have a significant effect on the results for c_2.

An additional step was also performed in the fits to the first-, second- and third-shell data. All the characteristic amplitude and phase parameters (c_0, c_2, c_3, a_0, a_1 and a_2) extracted from the data collected at 10 K were varied for the best fit to data collected at each temperature. The results for the amplitude parameters (c_0, c_2 and c_3) are listed in Table 4.3. It can be seen that, while in principle only c_2 should change, in fact the best fit is achieved with significant changes in all three amplitude parameters (the c_0–c_3 values). Since c_2 is affected by correlation with c_0 and c_3, c_2 by this method is less reliable than c_2 obtained by the simpler method above. Indeed, it can be seen that the trend in c_2 is not so regular as that in Table 4.2, especially for the second shell.

These results show that the variation of the EXAFS with temperature is accounted for by changes in c_2 or σ^2_{as} with good, but not complete accuracy. This is not surprising for the second and third shells, since they in fact contain several contributions from both single- and multiple-scattering paths. The fact that correlation occurs even in the first shell most probably simply shows the limit of accuracy achievable by the Fourier filtering/least-squares curve-fitting approach to EXAFS analysis within the large degree of freedom chosen.

In order to correlate the temperature trends observed for c_2 with possible ν and μ values for Cu(I)(*N*-methylimidazole)$_4$ClO$_4$, a comparison was made between the value of

$\Delta\sigma^2_{vib}(T)$, as calculated from Equation 4.2, and the observed $\Delta c_2(T)$, as calculated from the values in Table 4.2. The best fit with the experimental c_2 values were determined by evaluating

$$F(\mu,\nu)=\sum_{T_1,T_2}\left\{\left[\frac{h}{8\pi^2\mu\nu}\left(\coth\left(\frac{h\nu}{2kT_2}\right)-\coth\left(\frac{h\nu}{2kT_1}\right)\right)\right]-\left(-\frac{1}{2}\right)[c_2(T_2)-c_2(T_1)]\right\}^2 \quad \text{.....(4.3)}$$

over a grid of (μ ,ν) values. The (-1/2) factor is included since $\Delta c_2 = -2\Delta\sigma^2_{as}$ (see Chapter 2). Since there were c_2 values for five temperatures, $F(\mu,\nu)$ was summed over four sets of $\Delta(T_1,T_2)$ values at each (μ ,ν) point.

Given the precision to which c_2 values are trusted (~1×10^{-3} Å^2, or ~5×10^{-4} Å^2 for $c_2/2$), all values of (μ ,ν) for which $[F(\mu,\nu)-F(\mu,\nu)_{min}] < \sim 5 \times 10^{-7}$ Å^4 fall in the solution space. As shown in Figures 4.4, 4.5 and 4.6, the solution space turned out to cover a rather large range of (μ ,ν) values in a narrow valley along a "1/x line".

The summation was made by evaluating [f(45)–f(10)], [f(80)–f(45)], [f(130)–f(80)] and [f(200)–f(130)] and adding these terms. This gives the most weight to the c_2 values of the three temperatures in the middle (45 K, 80 K and 130 K). A narrower minimum could be obtained by maximizing the [$f(T_1)$–$f(T_2)$] terms in the expression for $F(\mu,\nu)$. This was done by taking all (T_1,T_2) differences with respect to 10 K, i.e. [f(45)–f(10)], [f(80)–f(10)], [f(130)–f(10)] and [f(200)–f(10)]. This gives much more weight to the c_2 value at 10 K than at the other temperatures, which is not entirely inappropriate, since the EXAFS amplitude at low temperatures is larger, and c_2 values obtained from low-temperature data should then in fact be more accurate. Changing the weighting of the c_2 values from different temperatures, though it made the minimum narrower, did not change the location of the minimum, and the minimum still included a large range of (μ ,ν) values along the "1/x line".

The results then show that, for the first shell (Figure 4.4), ν may be anywhere between 50–200 cm^{-1}, with most of the (μ ,ν) solutions occurring along ν ~50–100 cm^{-1}, and μ may be anywhere above 20 a.m.u. They are related to one another along the "1/x line", but the "valley" for which $F(\mu,\nu) < \sim 5 \times 10^{-7}$ Å^4 is ~50 cm^{-1} wide, and so there is considerable latitude in the possible solutions. The value of μ ($\cong$ 35 a m.u.) estimated above for a Cu–N(imidazole) stretch lies within the solution space, but not in the center of it. Better fits are obtained with $\mu > 60$ a.m.u. The values of ν from far-infrared studies of Cu(II)-imidazole compounds[17-19] (not Cu(I)) are 271–307 cm^{-1}, with one tentative assignment at 237 cm^{-1}, while those for Zn(II)-imidazole compounds[17,19,20] (since Zn(II)

is isoelectronic with Cu(I)) are 232–261 cm^{-1}. For the proteins hemocyanin and tyrosinase,[21,22] ν(Cu(II)–N(His)) has been assigned at 220–320 cm^{-1}. Even though, from chemical considerations, Cu(I)–imidazole bonds are expected to be weaker than either Cu(II)– or Zn(II)–imidazole bonds, they would be expected to have a frequency nearer to 200 cm^{-1} (about 170–220 cm^{-1}) than to 100 cm^{-1}.[23] It may be that, for this particular compound, Cu(I)(*N*-methylimidazole)$_4ClO_4$, where Cu(I)–N is longer than usual (2.054(2) Å),[24] ν is indeed ~100 cm^{-1}. On the other hand, if we use $\mu \cong 35$ a.m.u. as a constraint, then ν ~170 cm^{-1}, which is more reasonable, though it occurs at one end of the minimum "valley" and not in the center. If infrared spectroscopy is undertaken on this compound, a comparison of the ν value obtained will help to show whether it is useful to constrain μ.

It can be seen from Figures 4.5 and 4.6 that the $F(\mu, \nu)$ minima obtained for the second and third shells are narrower than that for the first shell. This is rather surprising, since with the many scattering interactions contributing to the EXAFS from these shells, we would have expected the temperature trend to deviate more from the harmonic oscillator model and produce broader minima. Also, despite the difference in the c_2 values for the second and third shells, the $F(\mu, \nu)$ minima for both shells occur over the same values of (μ, ν), with ν being between 30–200 cm^{-1}, but mostly occurring between 30–100 cm^{-1}, and μ being once again anywhere above 20 a.m.u. Closer inspection of Table 4.2 shows that similarity in the $F(\mu, \nu)$ minima is because Δc_2 actually turns out to be rather similar for both shells. Only the components of c_2 due to the intrinsic amplitude envelope (see Equation 2.7 in Chapter 2) and σ^2_{stat} (Equation 4.1) differ. The similarity in Δc_2 for the second and third shells is unexpected; we would have expected a shell at longer distance, and more affected by multiple-scattering, to be more susceptible to thermal damping than a nearer shell. At present we have no explanation for this result. Constraining μ to be ~35 a.m.u. once again gives a higher ν value (~150 cm^{-1}) at one extreme of the solution space. As before, the value of ν should be compared with IR studies on this compound, followed by a normal coordinate analysis.

Relative to the value of ν for the first shell, the value of ν obtained for the second and third shells is similar and only slightly lower. This probably shows that, while Cu–N–C bending modes are now convoluted with the Cu–N stretch in the observed EXAFS Debye-Waller factor, the imidazole ring can still be treated as a rigid unit in EXAFS analysis. Also, even in a Cu(I)-imidazole compound with a relatively long Cu–N bond, wagging or rotating motions about the Cu–N bond by the ring as a whole do not seem to have a major impact on the EXAFS Debye-Waller factor.

(F) Conclusion

For all three shells, it can be seen that c_2 is not very useful for obtaining a good value of μ. However, a physically correct value of μ, if a good estimate can be made, may possibly be useful in constraining c_2 values in fits to EXAFS data. At present we cannot explain why a reasonable value for μ should occur at the extreme end rather than the center of the solution space. The stretching frequency ν could be more useful in constraining c_2 values, but it still remains to be proven that the ranges of values for ν we obtained correctly bracket the true values of ν as it would be measured in an IR experiment. In the absence of such results, some indication of the reliability of these results could be obtained by fitting the EXAFS temperature series of a similar compound such as Cu(I)(*N*-methylimidazole)$_2$BF$_4$ (for which the appropriate data have already been collected). Since the Cu(I)–N bond is shorter (avg. 1.859(7) Å, see previous chapter) and presumably stiffer, the ν value obtained should be closer to 200 cm^{-1}. If this does indeed turn out to be the result, then it may be worth trying a value of ν as a constraint on the variation of c_2 in a temperature series of data.

This analysis has also shown that imidazole rings can to a good approximation be treated as rigid bodies for EXAFS analysis, ignoring their ring vibrational modes. Similarly, that wagging or rotation of the imidazole ring as a whole about the Cu–N bond does not occur to a sufficient degree to have much impact on the EXAFS Debye-Waller factor.

All this is still a long way from our goal of fitting the imidazole EXAFS accurately in a system, such as hemocyanin, for which scatterer distances and vibrational data are not accurately known, and for which imidazoles as well as other scatterers occur with greater spreads of distances and angles. Furthermore, it is not often that there will be data at multiple temperatures available for trying this fitting procedure. All the same, in the process, much insight into the EXAFS behaviour of imidazole will be gained, and this cannot but lead us closer to our final goal.

References

(1) Lontie, R.; Vanquickenborne, L. In *Metal Ions in Biological Systems*; 1st ed.; H. Siegel, Ed.; Marcel Dekker: New York, 1974; Vol. 3; pp 183-200.

(2) Ghiretti, F., ed. *Physiology and Biochemistry of Hemocyanins;* 1st ed.; Academic Press: New York, 1968.

(3) Van Holde, K. E.; Van Bruggen, E. F. J. In *Subunits in Biological Systems*; 1st ed.; S. N. Timasheff and E. D. Fasman, Ed.; Marcel Dekker: New York, 1971; Vol. Part A; pp 1-53.

(4) Solomon, E. I. In *Copper Proteins*; 1st ed.; T. G. Spiro, Ed.; John Wiley and Sons: New York, 1981; pp 41-108.

(5) Volbeda, A.; Hol, W. G. J. *J. Mol. Biol.* **1989**, *209*, 249-279.

(6) Gaykema, W. P. J.; Volbeda, A.; Hol, W. G. J. *J. Mol. Biol.* **1985**, *187*, 255-275.

(7) Magnus, K.; Ton-That, H. *J. Inorg. Biochem.* **1992**, *47*, 20.

(8) Brown, J. M.; Powers, L.; Kincaid, B.; Larrabee, J. A.; Spiro, T. G. *J. Am. Chem. Soc.* **1980**, *102*, 4210-4216.

(9) Co, M. S.; Hodgson, K. O. *J. Am. Chem. Soc.* **1981**, *103*, 3200-3201.

(10) Co, M. S.; Hodgson, K. O.; Eccles, T. K.; Lontie, R. *J. Am. Chem. Soc.* **1981**, *103*, 984-986.

(11) Woolery, G. L.; Powers, L.; Winkler, M.; Solomon, E. I.; Spiro, T. G. *J. Am. Chem. Soc.* **1984**, *106*, 86-92.

(12) Co, M. S.; Hendrickson, W. A.; Hodgson, K. O.; Doniach, S. *J. Am. Chem. Soc.* **1983**, *105*, 1144-1150.

(13) Pettifer, R. F.; Foulis, D. L.; Hermes, C. *J. de Physique* **1986**, *47*, C8545-C8550.

(14) Feiters, M. C.; Navaratnam, S.; Al-Hakim, M.; Allen, J. C.; Spek, A. L.; Veldink, G. A.; Vliegenthart, J. F. G. *J. Am. Chem. Soc.* **1988**, *110*, 7746-7750.

(15) Strange, R. W.; Blackburn, N. J.; Knowles, P. F.; Hasnain, S. S. *J. Am. Chem. Soc.* **1987**, *109*, 7157-7162.

(16) Natoli, C. R.; Benfatto, M.; Filipponi, A., Frascati National Laboratory, Italy, personal communication.

(17) Goodgame, D. M. L.; Goodgame, M.; Rayner-Canham, G. W. *Inorg. Chim. Acta* **1969**, *3*, 399-405.

(18) Eilbeck, W. J.; Holmes, F.; Taylor, C. E.; Underhill, A. E. *J. Chem. Soc. (A), Inorg. Phys. Theor.* **1968**, 128-132.

(19) Cornilsen, B. C.; Nakamoto, K. *J. Inorg. Nucl. Chem.* **1974**, *36*, 2467-2471.

(20) Goodgame, D. M. L.; Goodgame, M.; Hayward, P. J.; Rayner-Canham, G. W. *Inorg. Chem.* **1968**, *7*, 2447-2451.

(21) Eickman, N. C.; Solomon, E. I.; Larrabee, J. A.; Spiro, T. G.; Lerch, K. *J. Am. Chem. Soc.* **1978**, *100*, 6529-6531.

(22) Freedman, T. B.; Loehr, J. S.; Loehr, T. M. *J. Am. Chem. Soc.* **1976**, *98*, 2809-2815.

(23) Loehr, T., Oregon Graduate Institute, USA, personal communication.

(24) Clegg, W.; Acott, S. R.; Garner, C. D. *Acta Cryst.* **1984**, *C40*, 768-769.

Table 4.1. Some of the more probable scattering paths for a Cu-imidazole system. Similar paths involving C_2 and C_3 also occur.

Single-scattering	Double-scattering	Triple-scattering
$Cu–N_1–Cu$	$Cu–N_1–C_1–Cu$	$Cu–N_1–C_1–N_1–Cu$
$Cu–C_1–Cu$	$Cu–C_1–N_2–Cu$	$Cu–C_1–N_2–C_1–Cu$
$Cu–N_2–Cu$	$Cu–N_1–N_2–Cu$	$Cu–N_1–N_2–N_1–Cu$
		$Cu–N_1–N_2–C_1–Cu$

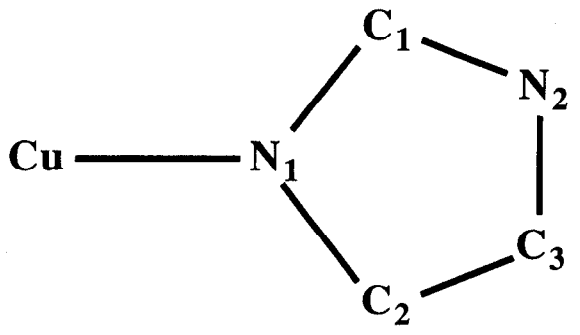

Figure 4.1. Schematic of a Cu–imidazole ring. N_1 is in the first shell, C_1 and C_2 are in the second shell and N_2 and C_3 are in the third shell. The second and third shell together are also referred to as the outer shells.

Table 4.2. Values of c_2 obtained by using parameters extracted from data collected at 10 K and varying c_2 only.

Temperature	Value of c_2 (Å^2)		
	First Shell	Second Shell	Third Shell
10 K	-0.01231	-0.03589	-0.02374
45 K	-0.01235	-0 03636	-0.02427
80 K	-0.01293	-0.03768	-0.02526
130 K	-0.01495	-0.04006	-0.02768
200 K	-0.01713	-0.04323	-0.03076

Table 4.3. Amplitude parameters obtained by varying six amplitude and phase parameters (c_0, c_2, c_3, a_0, a_1 and a_2) for the closest fit to data at each temperature.

Temperature		c_0	c_2	c_3
First Shell†	10 K	0.98428	-0.01231	-1.07515
	45 K	0.83541	-0.01285	-0.97802
	80 K	0.90618	-0.01312	-1.02831
	130 K	0.73034	-0.01570	-0.90375
	200 K	0.97287	-0.01503	-1.14167
Second Shell	10 K	0.00192	-0.03589	+2.40278
	45 K	0.00111	-0.04150	+2.84896
	80 K	0.00043	-0.04887	+3.50962
	130 K	0.01191	-0.03065	+1.21972
	200 K	0.01096	-0.03424	+1.28778
Third Shell	10 K	0.40400	-0.02374	-0.51130
	45 K	0.39316	-0.02430	-0.49638
	80 K	0.19256	-0.02997	+0.00494
	130 K	0.09958	-0.03666	+0.46615
	200 K	0.06515	-0.04180	+0.74227

† — These values may be slightly erroneous because there was an error in setting the value of the phase parameter a_{-1} (a_{-1} = 16.33 instead of 0) while extracting these parameter sets.

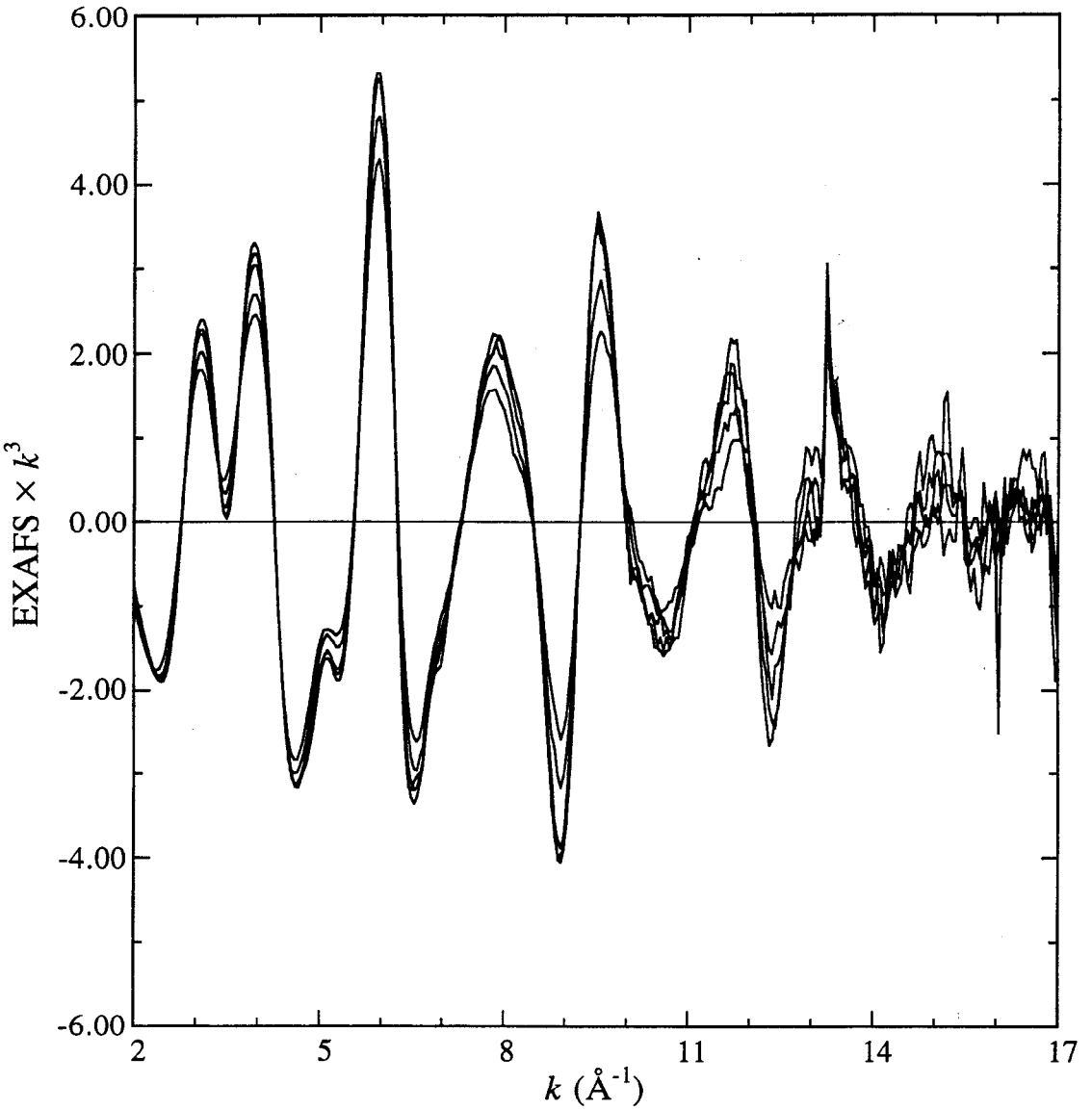

Figure 4.2. Averaged EXAFS spectra of Cu(I)(*N*-methylimidazole)$_4$ClO$_4$, measured at 10, 45, 80, 130 and 200 K to k = 17 Å^{-1}. There is a monotonic decrease in the overall amplitude of the EXAFS signal as the temperature is raised.

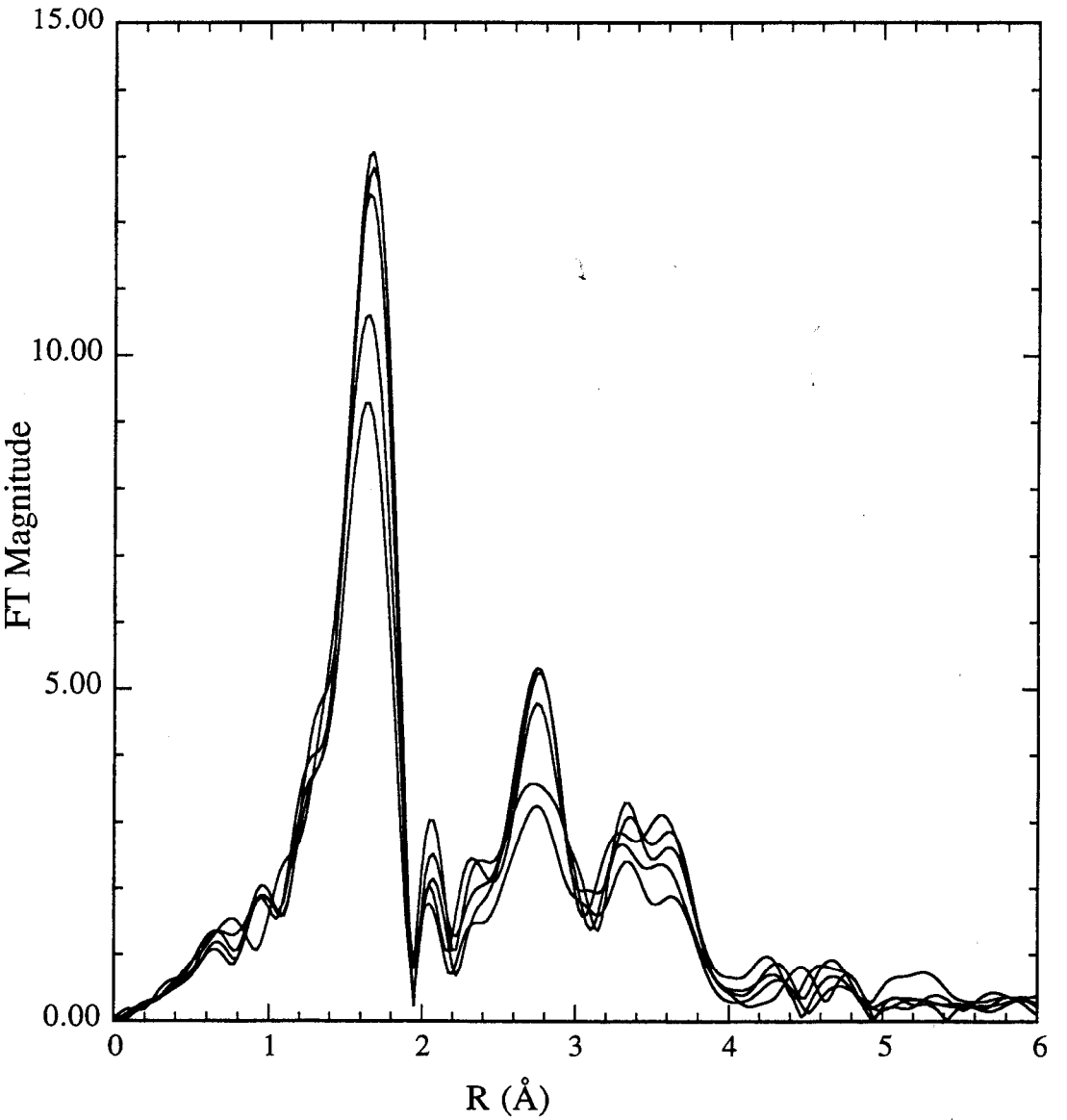

Figure 4.3. Fourier transforms over k = 3.5–16.5 (0.1) $Å^{-1}$ of the averaged EXAFS spectra of Cu(I)(*N*-methylimidazole)$_4ClO_4$, measured at 10, 45, 80, 130 and 200 K, shown in Figure 4.2. There is a monotonic decrease in the Fourier transform magnitude as the temperature is raised.

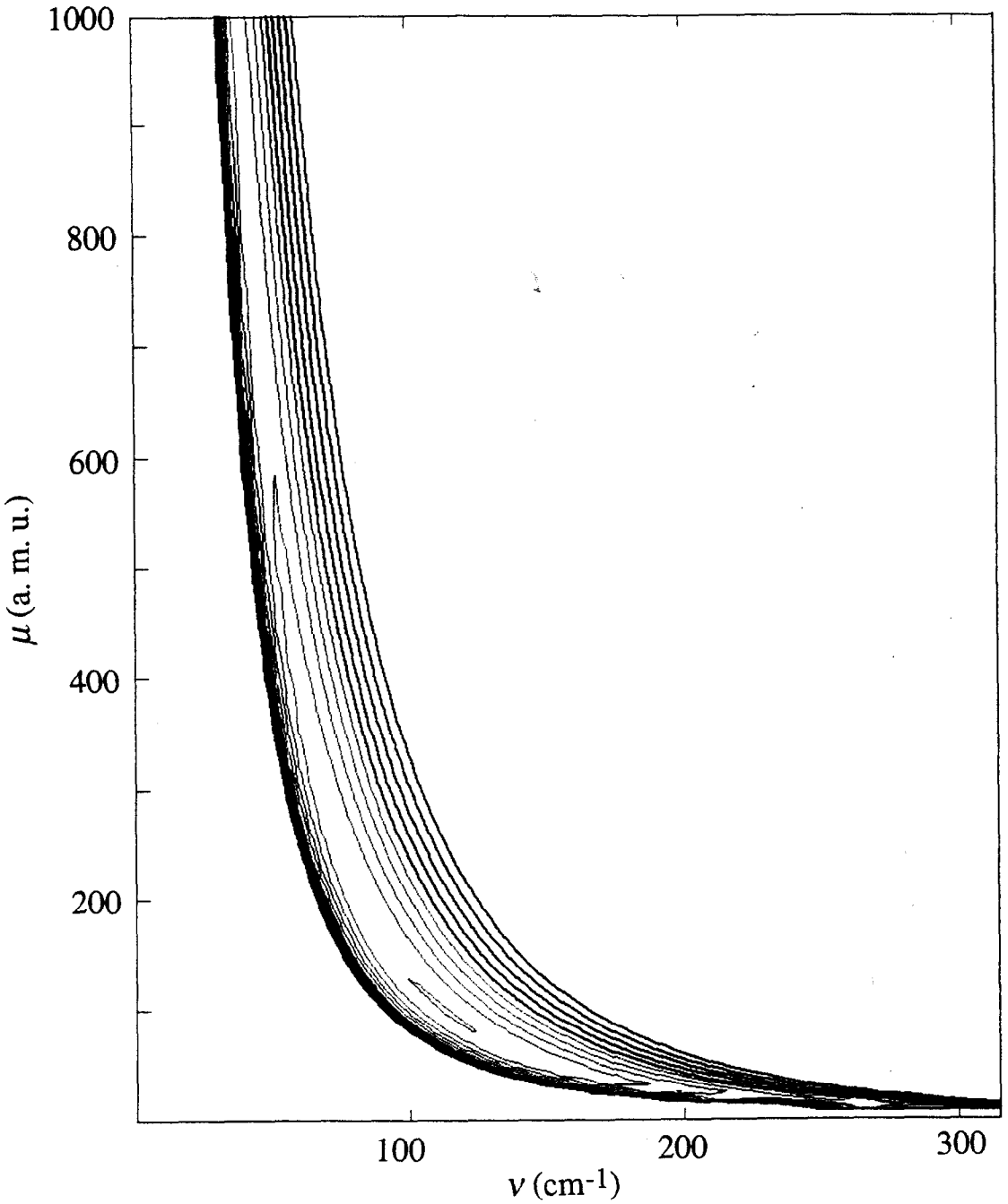

Figure 4.4. Contour plot of $F(\mu, \nu)$ for c_2 values (listed in Table 4.2) from fits to the first shell. $F(\mu, \nu)$ was evaluated by taking differences between adjacent temperatures (i.e., [f(45)–f(10)], [f(80)–f(45)], [f(130)–f(80)] and [f(200)–f(130)]. The thin lines show where $F(\mu, \nu) < 5\times10^{-7}$ Å^4, and the heavy lines show where $F(\mu, \nu) < 1\times10^{-6}$ Å^4.

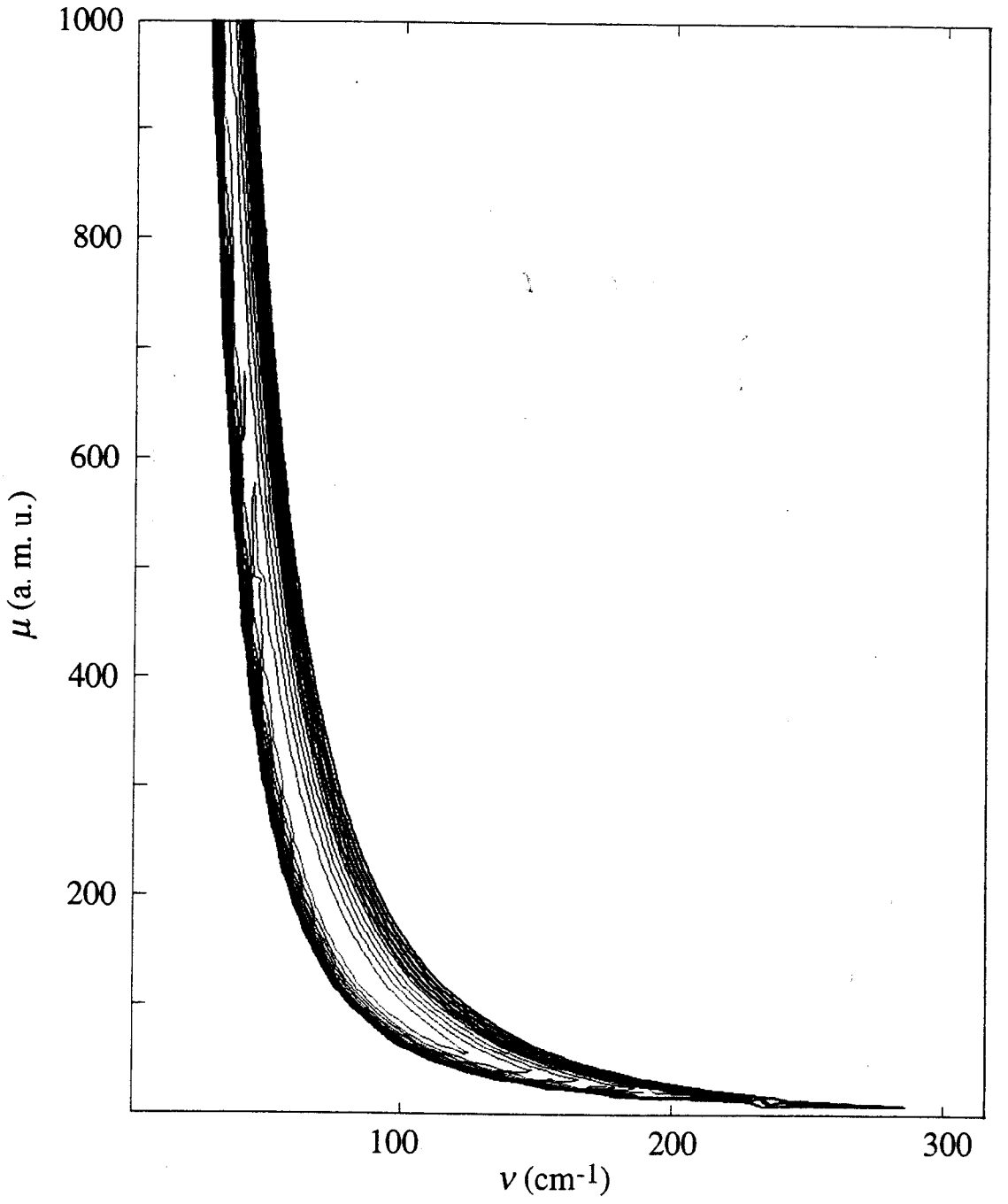

Figure 4.5. Contour plot of $F(\mu, \nu)$ for c_2 values (listed in Table 4.2) from fits to the second shell. $F(\mu, \nu)$ was evaluated by taking differences between adjacent temperatures (i.e., [f(45)–f(10)], [f(80)–f(45)], [f(130)–f(80)] and [f(200)–f(130)]. The thin lines show where $F(\mu, \nu) < 5\times10^{-7}$ Å^4, and the heavy lines show where $F(\mu, \nu) < 1\times10^{-6}$ Å^4.

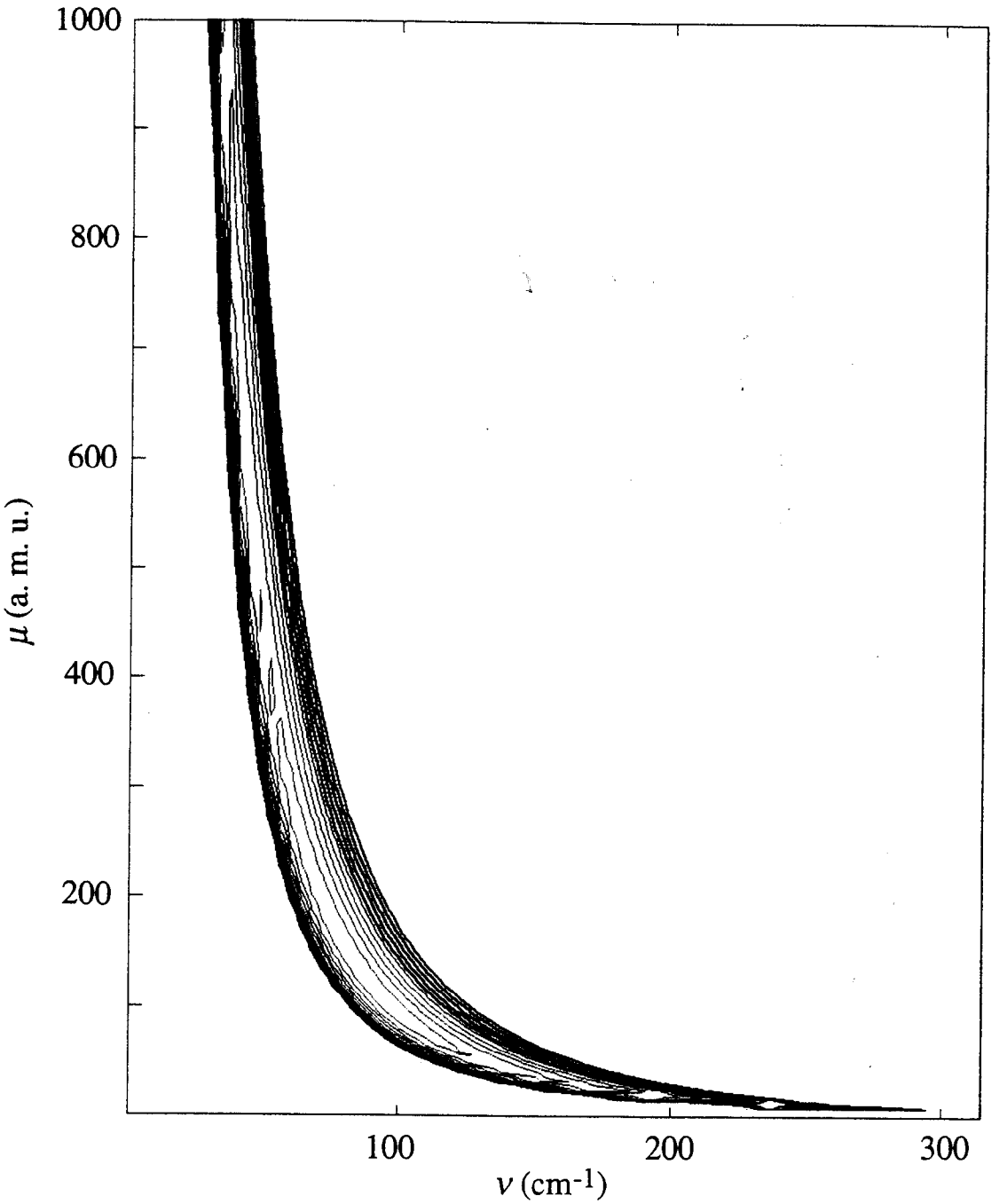

Figure 4.6. Contour plot of $F(\mu, \nu)$ for c_2 values (listed in Table 4.2) from fits to the third shell. $F(\mu, \nu)$ was evaluated by taking differences between adjacent temperatures (i.e., [f(45)–f(10)], [f(80)–f(45)], [f(130)–f(80)] and [f(200)–f(130)]. The thin lines show where $F(\mu, \nu) < 5\times10^{-7}$ Å^4, and the heavy lines show where $F(\mu, \nu) < 1\times10^{-6}$ Å^4.

Chapter 5

EXAFS Studies of Reduced Poplar Plastocyanin at High and Low pH

(A) Structure and Function of Plastocyanin

(1) Overall Structure of Plastocyanin

Plastocyanin is a small protein, containing one copper atom, that functions as a electron carrier in the process of photosynthesis.[1] It is the last carrier in a chain of electron transport from Photosystem II to Photosystem I, transferring one electron between the membrane-bound proteins cytochrome *f* and P700 (Photosystem I). This protein, along with other "blue copper" proteins, is also of special interest to inorganic chemists because of its unique spectroscopic features, including an unusually intense blue colour and a very small EPR hyperfine splitting in the $g_{\|}$ region, which are not easily matched in any small-molecule copper compound.[2-5]

The crystal structure of Poplar plastocyanin (*Populus nigra*, var. *italica*, henceforth Pc) has been determined (Figure 5.1(a)), in both oxidized and reduced forms, at various pH's, at resolutions ranging from 1.33 Å to 2.15 Å.[6-8] This protein has 99 amino acid residues, and takes the form of a slightly flattened β-barrel, with almost no α-helix structure. The copper atom is found near one end of the barrel, ligated by two histidines (residues 37 and 87), a cysteine (residue 84) and a methionine (residue 92). The intense blue colour of the protein is ascribed to ligand-to-metal charge transfer from S(cysteine) to Cu. Recently, X-ray absorption spectroscopy at the sulfur K edge has shown that the small hyperfine splitting in the $g_{\|}$ region is due to the highly covalent nature of the Cu–Cys84 bond.[9] Histidine 87 protrudes from the surface of the protein at one end, and may provide a redox pathway to or from the copper.

(2) Structure of the Copper Site and Its pH Dependence

The geometry of the copper atom is unusual, being a distorted tetrahedron rather than tetragonal (Figure 5.1(b)). Another distinctive feature is the Cu–Met92 bond, which is 2.82 Å long in the oxidized protein.[8] As confirmed by the high reduction potential of 370 mV,[10] this unusual geometry optimizes the Cu for electron transfer, facilitating oxidation and reduction with little change in geometry.

The redox potential of Pc is strongly pH dependent below pH 5.4.[10] The presence of a protonated redox-inactive form of Pc at low pH has been suggested.[11] Crystal structures determined at two pH's on oxidized Pc[6] show that the structure of oxidized Pc is essentially unchanged between pH 4.2 and pH 6.0. However, crystal structure determinations of reduced Pc[7] at six pH's between 3.8 and 7.8 show that the copper site changes significantly while the rest of the protein remains much the same. Between pH 7.8 and pH 3.8, the Cu–Met92 bond in the crystal structures changes from 2.90 Å to 2.52 Å,

while the Cu–His87 bond breaks, and the coordination of the Cu becomes trigonal planar (Figure 5.1(c)). At pH 3.8, the distance between Cu and the nearest atom of His87 is 3.15 Å, and the imidazole ring of His87 has actually rotated 180° so that carbon rather than nitrogen is the nearest atom to Cu. This suggests that His87 has been protonated and that Pc at pH 3.8 may indeed be inactive. The lengths of the Cu–His37 and Cu–Cys84 bonds do not change significantly with pH.

(3) Some Questions About the Copper Site

Although the crystal structure of Pc has been solved, questions about the structure and function of the copper site remain, some of which may be addressed by X-ray absorption spectroscopy. One such question is whether the gradual changes observed in the Cu site geometry are really due to a gradual shifting with pH, or to a shifting equilibrium between two extreme positions. The latter is more chemically reasonable. However, the crystallographic data alone were not sufficient to rule out either possibility, and while evidence from the pH-dependent reduction potential and reactivity of Pc was suggestive of an equilibrium, it was not conclusive.

While X-ray crystallography reveals the position of the Met92 sulfur equally well whether it is 2.90 Å or 2.52 Å from Cu, in EXAFS the Cu–S contribution would be stronger for a shorter and stiffer Cu–S bond. Thus, S at 2.5 Å from Cu will be much more easily detected than S at 2.9 Å. So, if the variation in Cu–S bond length is truly due to a gradual change in Cu–S bond length, we would find S at intermediate bond lengths for intermediate pH's. On the other hand, if it is due to a shifting equilibrium, EXAFS would perceive a partial atom at the shorter bond length.

Another major reason to perform an EXAFS study of reduced Pc is that EXAFS is capable of giving bond lengths to a precision of 0.03 Å or better, while the crystal structures of Pc have Cu–ligand bond lengths with standard deviations varying from 0.04 Å to more than 0.07 Å.[8] In particular, the resolutions of the crystal structures at pH 3.8 and pH 7.8, which would give the best view of the two extreme geometries, are such that the standard deviations are greater than 0.07 Å. Thus, the extra precision afforded by EXAFS would be valuable in helping to understand the chemistry of plastocyanin. Also, we wished to see if the structure of reduced Pc in solution, especially at low pH, was the same as in the crystal structure.

(B) Experimental Details

(1) Preparation of Samples

Two samples of Poplar plastocyanin (at pH 7.2 and 4.8) were provided by Professor Hans C. Freeman of the University of Sydney, Australia. Two bands of plastocyanin were separated by ion-exchange chromatography of the reduced Pc on DEAE resin or Q-Sephadex using a NaCl gradient column.[12] The pH 7.2 sample was taken from Band 1, and dialyzed with a 0.1 M sodium phosphate buffer with 0.05 M sodium ascorbate to keep the sample reduced. The solution was made 40% in glycerol by dialysis, and the final concentration was 4–4.2 mM. The pH 4.8 sample was from Band 2, in a 0.1 M sodium acetate buffer with 0.05 M sodium ascorbate, which was added as ascorbic acid. The pH was adjusted to 4.8 by addition of sodium hydroxide solution. This solution was also made 40% in glycerol. The concentration of the pH 4.8 sample is not precisely known since some precipitation of the protein occurred as the pH was lowered, but it is estimated to be ~3 mM.

Each solution was loaded into an EXAFS cell made of lucite (outer dimensions $2 \times 4 \times 28$ mm^3, volume ~180 µl) with an X-ray-transparent front face of 60 µm Mylar tape for X-ray fluorescence measurements. The samples were stored in liquid nitrogen and also mounted for data collection under liquid nitrogen.

Cu(I) model compounds were ground with boron nitride and packed into aluminum spacers in the manner described in Chapter 2.

(2) Data Collection

Protein data were collected at the Stanford Synchrotron Radiation Laboratory at the unfocussed 8-pole wiggler beam line 4-2 in fluorescence mode, using a Lytle detector[13] with a nickel filter, and argon gas in the chamber. Ring current was between 25 and 49 mA. The temperature of the samples during data collection was 10–12 K. No photoreduction or oxidation of either sample was observed during data collection, but in both cases, when the samples were removed from the X-ray beam, the originally clear and colourless frozen glass had turned brown where the beam had passed through it. Data for Cu(I) models were collected in transmission mode at 10 K.

(3) Data Analysis

Data were reduced and analyzed using XFPAKG, using the approach described in Chapter 2. Scans were calibrated using copper foil as an internal standard, taking the first inflection point of the foil as 8980.3 eV. Twenty-one scans were averaged together for the

high pH sample, and 29 scans for the low pH sample. A major glitch was removed from both the averaged data sets at k = 10.9 Å^{-1}. Subtraction of the background was done by fitting a polynomial to the EXAFS region and then applying this at the bottom of the "edge step" and extending this into the pre-edge region. The same three-region spline to k = 13 Å^{-1} was used for both data sets (Figure 5.3). For all data analyzed in this chapter, a data range of k = 3.5–12.5 Å^{-1} was used for the forward Fourier transform (Figures 5.2 and 5.4), and the data were then backtransformed to k = 4–12 Å^{-1} for curvefitting. Phase and amplitude parameters were also extracted over the same data ranges.

(C) EXAFS Fits to the Data — Results and Discussion

(1) Extraction of Parameters and Testing on a Cu(I)–N_2S_2 Model

Using the method for parameter extraction described in Chapter 2, Cu(I)–N parameters were extracted from data collected at 10 K on Cu^I(*N*-methylimidazole)$_4ClO_4$,[14] which has four crystallographically equivalent methylimidazoles ligated about Cu(I) in a tetrahedral geometry. The Cu(I)–N distance in this compound is 2.054 Å. Similarly, Cu(I)-S parameters were extracted from $[Cu^I(diethylthiourea)_3]_2SO_4$,[15] which has three crystallographically equivalent diethylthioureas ligated at a Cu(I)–S distance of 2.241 Å. Data collected on $Cu^I_2((CH_3NCH_2CH_2SSCH_2CH_2N(CH_3)_2)_2(BF_4)_2$[16] (Figure 5.2), a compound with Cu(I)–N_2S_2 ligation, were used to test these parameters. The two Cu atoms in this dimer are not crystallographically equivalent, but they have very similar bond lengths. Cu(I)–N bond lengths range between 2.089–2.184 Å, and Cu(I)–S bonds between 2.283–2.326 Å.

A Fourier window over 1.35–2.35 Å was used to filter out the main peak of the data on the Cu(I)–N_2S_2 compound (henceforth referred to as CUNS2) for data analysis (Figure 5.2). It was not possible to widen the window in a manner analogous to the treatment of the protein data *(vide infra)* without including contributions from second-shell carbon atoms, so this was not done. One-, two- and three-wave fits were performed on the filtered data, as shown in Table 5.1. (See also Appendix I for complete fit results.)

The relative Debye-Waller factor is represented by the parameter c_2, which is always negative (see Chapter 2). A larger negative value of c_2 indicates more disorder in the distances of scatterers, or more vibrational disorder and a weaker Cu–X bond. Coordination numbers and c_2 values were evaluated together to determine the most reasonable fit to a data set.

Fits were done either by floating coordination numbers and fixing c_2 (Type 2 fits), or varying c_2 and fixing coordination numbers (Type 3 fits), or occasionally by varying both

coordination numbers and Debye-Waller factors (Type 1 fits). In all fits, the Cu–X distances of all waves were varied. In two- or three-wave Type 1 fits, there is considerable correlation between the coordination numbers and c_2 values, and so these fits do not have much physical significance as such. However, they can be useful in finding out what minimum the data tend towards.

As can be seen from Table 5.1, fits were done not only for scatterer combinations that we expected to find (such as Cu to N and S), but also for site geometries that we did not expect to find (such as Cu–N only or Cu–S only). How closely such "incorrect" or "negative" fits can model the data gives an indication of how significant the "correct" fits are. Table 5.2 summarizes the results for Type 2 fits. From it we can see that the two-wave fit which has the smallest fit function (fit index F = 0.134) is indeed the physically correct one, namely N+S with 1.6 N at 2.11 Å and 1.4 S at 2.28 Å. Two other minima were found for the N+S fit. However, these not only fit much more poorly (fit index F = 0.665 and 0.301 respectively), but they are physically quite implausible, having an unreasonably high coordination number for N and a very long Cu–S bond in one case, and an unreasonably long Cu–N bond in the other. Also, fits with N+N' and S+S' waves either fitted the data very poorly or gave manifestly unphysical results (such as negative coordination numbers).

Fits of Type 3 behaved in a similar fashion, that is, N+S fits fitted the data much better than either N+N' or S+S' fits. The Type 3 fit with the lowest fit index was achieved using 1N at 2.14 Å with 2S at 2.27 Å rather than 2N at 2.17 Å with 2S at 2.26 Å, which proved to have the next closest fit. However, the Debye-Waller factor for the N-wave in the 2N+2S fit ($\Delta\sigma^2$ = +0.001) makes better physical sense than that in the 1N+2S fit ($\Delta\sigma^2$ = -0.003), because the Cu(I)–N length has increased relative to that in Cu^I(*N*-methylimidazole)$_4ClO_4$, and this should be accompanied by an increase in the Debye-Waller factor. Therefore, the 2N+2S fit may still be considered the most plausible fit.

A couple of three-wave fits (N+N'+S) were tried, but they yielded either totally unphysical results or the very same minimum that was achieved with the N+S fit.

Thus, we may conclude that the most reasonable fit to CUNS2 (2N+2S) is the one that we know to be physically correct, and that the parameters we extracted are working as they should and giving us the right answers. We also gain a good idea of the precision of coordination numbers obtained using these parameters.

(2) Fits to Reduced Plastocyanin at pH 7.2 and 4.8

(a) Fourier Transform Windows and Types of Fits Done

The averaged data sets for the two protein samples were curvefitted in parallel. By and large, a fit that was done on the high pH data (hereafter PCHI) was also done on the low pH data (PCLO) and vice versa. Our working assumption was that the solution structure of reduced Pc at pH 7.2 would most probably be similar to the crystal structure, with one long Cu–Met92 bond, while there was less certainty about the structure of reduced Pc at lower pH. Thus PCHI served as an internal reference against which to gauge the reliability of fits to PCLO. Wishing to search for a sulfur scatterer between 2.5 Å and 2.9 Å, but uncertain if scattering from the carbon atoms of the imidazole rings of the ligated histidines would instead be detected, we decided to try fits on Fourier transform windows of various widths, starting from a bare main peak and widening the shell by stages to include the first small peak to higher R, then the second as well (see Figure 5.4, Table 5.3). Since a low-R shoulder of significant height seen in the Fourier transform for the PCLO data could not be removed by splining, fits were also done on a window for both PCHI and PCLO including it.

Various one-, two- and three-wave fits were performed using Cu(I)–N and Cu(I)–S parameters (see Table 5.4, also Appendix I for complete fit results). These fits were done either by floating coordination numbers and fixing Debye-Waller factors (Type 2 fits in Tables 5.5 and 5.6), or by varying Debye-Waller factors and fixing coordination numbers (Type 3 fits in Table 5.7), or occasionally by varying both coordination numbers and Debye-Waller factors (Type 1 fits). Type 1 fits were mainly done in the initial stages of data analysis to obtain a feel for the minima that the data tend towards. For two-wave and three-wave fits, Type 1 fits cannot be relied on to produce physically trustworthy results because of high parameter correlation, and so only Type 2 and Type 3 fits are discussed. As it turned out, results from Type 2 and Type 3 fits led to the same conclusions, so most of the following discussion is in terms of Type 2 fits.

Once again, besides using combinations of waves that we expected to find in the data (such as N+S+S'), we used combinations that we did not expect to find (such as N+N') to test the significance of the fits we obtained.

(b) Results of Two-Wave Fits

For PCHI, Type 2 N+S fits on all windows gave 1.9 N at 2.03 Å and 0.5 S at 2.20 Å. For PCLO, the same fits gave two minima : -0.4 N at 1.85 Å with 0.9 S at 2.16 Å and

1.9–2.4 N at 2.17 Å with 1.4–1.5 S at 2.14 Å. The latter is by far the better fit to the data. Type 3 N+S fits were also done, and in PCHI they tended to come up with longer Cu–N distances (2.08 Å) than the Type 2 fits did. Of the fits tried, the most physically believable fit (2N+1S) did not produce the closest fit, but it did produce the most sensible Debye-Waller factors. In PCLO, there were again two minima, one with essentially no N-wave (a huge Debye-Waller factor) and 1S at 2.13–2.15 Å and another, much better-fitting minimum suggesting 2N (rather than the expected 1N) at 2.13 Å and 1S at 2.15 Å. It is obvious that the poorly-fitting minimum with no or negative N signal is not physically believable. It is only mentioned here because these two minima for PCLO occur again in the three-wave fits *(vide infra)*.

Comparing all the Type 2 two-wave fits done (see Table 5.5, also Appendix I), it is clear that, for PCHI, N+N' and S+S' do not fit the data as well as N+S, but since their fit indices are less than twice that for N+S, the fits may not be considered completely unsuccessful. For fits to PCLO, N+N' produced extremely poor fits, and so N+N' is easily ruled out as a viable fit. However, S+S' actually produced fits as good as N+S, or even slightly better. For both PCHI and PCLO, two minima could be obtained by varying the initial distance for S'. In both these minima, for both PCHI and PCLO, R_S remained constant at 2.16–2.19 Å, but $R_{S'}$ changed considerably, being found at either 2.33–2.37 Å or 2.74–2.96 Å. These two minima are also found in the N+S+S' fits *(vide infra)*. However, unlike in the three-wave fits, the short-S' minimum is a much better fit than the long-S' fit, so the S+long-S' fit can be dismissed as unlikely to be a true solution for either PCHI or PCLO. In PCHI, since S+short-S' is a worse fit than N+S, we may conclude that short-S' is doing its best to fill in for the absent N. In PCLO, S+short-S' fits the data as closely as N+S, so the fit index F cannot be used to choose the more likely fit of the two. However, only 0.4 S' are found at 2.37 Å in the S+short-S' fit, whilst 1.9–2.1 N are found in the N+S fit (~1 S occurs at 2.15 Å for both fits). The N+S fit thus seems more plausible, if we are using only two waves to account for all the ligands coordinated to Cu. If we consider that perhaps two waves are not enough to model all the different contributions to the EXAFS of PCLO, then both the N+S and the S+short-S' fits may be accurately reflecting the contributions of different scatterers.

(c) Results of Three-Wave Fits

The N+S+S' fits (see Tables 5.6 and 5.7) are of particular interest, since they most closely model the Pc site as shown by the crystal structures. We discovered that, simply by varying the initial distance for the S'-wave, different minima could be reached.

If $R_{S'}$ were initally set at 2.5 Å, then the fit would refine to a minimum of $R_{S'}$ = 2.3–2.4 Å. But if $R_{S'}$ was initially set at a higher value (2.8 Å for PCHI, 2.6 Å for PCLO), the fit invariably refined to a value of $R_{S'}$ greater than 2.7 Å. This was true of both PCHI and PCLO, for fits of both Type 2 and Type 3, and it was true for every Fourier window that the N+S+S' fit was performed on (Windows 1–3), even though Windows 1 and 3 do not include data above R' ~ 2.4 Å.

If the short $R_{S'}$ fit were either as good or better than the long $R_{S'}$ fit for PCLO, and the reverse were true for PCHI, then we might be able to conclude that S' in PCLO is indeed at a shorter distance than it appears in the crystal structure at low pH. However, in most of the N+S+S' fits performed, on PCHI as well as on PCLO, the short $R_{S'}$ fit is as good as or better than the long $R_{S'}$ fit. Since we are not expecting to find both sulfurs at short distances in Pc at high pH, we would tend to regard the fit minimum with the short $R_{S'}$ for PCHI as a false minimum not reflecting the true physical arrangement of scatterers about the copper atom. If we so regard this minimum in PCHI, we need good reasons to regard the similar minimum in PCLO differently. In the absence of such reasons, we cannot conclude for sure that the Cu–S' distance is truly now less than 2.4 Å in PCLO.

One possible reason for the good fit with a short $R_{S'}$ is that, in Windows 1 and 3, data from R' > 2.4 Å were not included. However, if we examine Window 2 alone, we still find that, for Type 2 fits, the short-$R_{S'}$ fit is as good or better than the long-$R_{S'}$ fit at both pH's. In the Type 3 fits, however, we do find a possible hint of a meaningful trend (see Table 5.7). In Windows 1 and 3, the short-$R_{S'}$ fits achieve a closer fit to the data (with fit indices being 15–60% lower) than the long-$R_{S'}$ fits. In Window 2, the short-$R_{S'}$ fit has a fit index that is 16% higher than the long-$R_{S'}$ fit for PCHI, but 10% lower for PCLO. This is certainly suggestive of a truly long Cu–S' bond in PCHI and a truly shorter Cu–S' bond in PCLO. However, the differences in the fit indices are not enough to be considered firmly significant, especially since this trend is confounded rather than confirmed by the Type 2 fits.

While the behaviour of the Cu–S' wave in N+S+S' fits is remarkably similar in both PCHI and PCLO, this is not so for the Cu–N wave in these same fits. Considering only Type 2 fits (Table 5.6), in PCHI, the contribution from N remains fairly stable (1.5–1.9 N at 2.01–2.03 Å in all fits except one on Window 3, where 1.0 N occurs at 1.99 Å) for both the long-S' and short-S' minima. Also, no fit component exceeds the magnitude of the total fit (Figures 5.5 and 5.6).

However, in PCLO, in behaviour similar to that in the N+S fits *(vide supra)*, for the short-S' minimum we find 0.3 N at 2.02 Å (except in Window 3), while for the long-S'

minimum we find 1.5–2.3 N at 2.10–2.19 Å. In the corresponding Type 3 fits, the N-wave makes even less of a contribution in the short-S' minimum, disappearing to almost nothing at an improbably short distance of 1.75–1.80 Å in Windows 1 and 2, whereas in the long-S' minimum it acquires a Debye-Waller factor than is far too low for a Cu(I)–N bond of over 2 Å. In Window 3, the presence of the contribution from the large low-R shoulder results in a larger component of N in the fit, about 0.4 N at 1.85 Å. Nor does the N-wave disappear in the Type 3 fits. Overlaying the backtransformed data with the N-, S- and S'-waves in a typical fit (Figures 5.7 and 5.8), it can be seen that massive cancellation occurs in order to produce both minima in the fits to PCLO. In both cases, the S-wave (modelling the short Cu–Cys84 bond) is actually larger than the total EXAFS. For the short-S' minimum, the S-wave is partly cancelled by the S'-wave, while in the long-S' minimum the S-wave is partly cancelled by the N-wave. Thus there is considerable correlation between the N-wave and the S'-wave, and we hesitate to conclude that the numbers for either the N- or S'-wave produced by these fits are a true indication of their location around Cu in PCLO. However, the S-wave is remarkably little affected by the dance that the N- and S'-waves are performing around it; we consistently find it at 2.13–2.17 Å, and in general it shows the same coordination number for both minima, for a given Fourier transform window.

Some N+S+N' fits were also made (see Table 5.6). For both PCHI and PCLO, these fits are slightly better than the N+S+S' fits for Window 1, and slightly worse for Window 2. There is always less than 0.5 N' present, and $R_{N'}$ occurs at up to three different distances for the same window, and so it can be seen that the minima it found are very shallow. On the other hand, a substantial N-wave (more than 1 N, usually closer to 2 N) at about 2.1 Å is always present, along with the stable S-wave at about 2.15 Å. These two waves look rather like the N- and S-waves in the long-S' minima discussed above. The N+S+N' fits may thus be interpreted as basically the same N+S fit found for the long-S' solution above, plus an N'-wave trying to fill up the little spaces left. The uncertainty in $R_{N'}$ shows that no firm conclusions should be based on it. The fact that the N+S+N' fit works about as well as the N+S+S' fit for both PCHI and PCLO also indicates that caution is warranted in believing the S' results in the long-S' N+S+S' fit, even in PCHI.

The results we have obtained so far on PCHI (~2 N at 2.02 Å and ~1 S at 2.20 Å) do not resemble the reduced pH 7.0 crystal structure distances that closely (see Figure 5.1(c)). Some 1N+1N'+1S fits on Window 3 of PCHI were carried out (see Table 5.8), using initial distances (R_N = 2.15 Å, $R_{N'}$ = 2.40 Å and R_S = 2.15 Å) close to the crystal structure distances (R_N = 2.16 Å, $R_{N'}$ = 2.37 Å and R_S = 2.15 Å). When only R's were varied, we

obtained R_N = 2.11 Å, $R_{N'}$ = 2.63 Å and R_S = 2.17 Å. A Type 2 fit (varying R's and CN's) led to the implausible result of 8.4 N at 2.07 Å, 2.3 N' at 2.34 Å and 1.5 S at 2.03 Å. A Type 3 fit gave R_N = 2.11 Å, $R_{N'}$ = 2.04 Å and R_S = 2.17 Å (c_{2N} = -0.0267, $c_{2N'}$ = -0.0326 and c_{2S} = -0.0255). The distances are reasonable in themselves, but we would have expected that if $R_{N'} < R_N$, then $|c_{2N'}| < |c_{2N}|$, and we find that the reverse is true. So this result, also, should be regarded with caution. So, for the N+N'+S fits N and S are well-behaved (though Cu–N is somewhat shorter than the crystal structure value of 2.16 Å), but N' does not fall anywhere near the crystal structure value of 2.37 Å in a reasonable fit.

We also tried adding S' at 2.9 Å for a few N+N'+S+S' fits (see Table 5.8). When only R's were varied, results were similar to the N+N'+S fit (2.11 Å, 2.59 Å, 2.17 Å and 2.91 Å respectively). When all R's and two CN's (N' and S') were varied, the result for N' was again implausible (-0.9 N at 2.37 Å). A Type 3 fit gave R_N = 2.11 Å, $R_{N'}$ = 2.59 Å, R_S = 2.17 Å and $R_{S'}$ = 2.95 Å. So, even with a four-wave fit, N' could not be found anywhere between 2.3 Å and 2.4 Å except with a negative CN.

The crystal structure at pH 7.0 was determined with a resolution of 1.8 Å, which gives a standard deviation σ of 0.07 Å in Cu–X bond lengths, with 3σ being ~0.2 Å. So Cu–S and Cu–S' from EXAFS (2.17/2.95 Å) are not significantly different from Cu–S and Cu–S' in the crystal structure (2.15/2.88 Å). One of the N's is also found by EXAFS at a distance not significantly different from the crystal structure distance (i.e., 2.11 Å and 2.16 Å respectively), while the other N, being at either 2.59 Å or 2.04 Å, may truly occur at a different distance from that in the crystal structure (2.37 Å).

This suggests either that, at pH ~7, the distances of at least one Cu–ligand bond are indeed different in solution from what was found in the crystal structure, or that it is not possible to resolve the true distances of these ligands over this data-fitting range.

D) Conclusion

A thorough and cautious analysis of data from solution samples of reduced Pc at pH 7.2 and pH 4.8 shows that it is difficult to resolve the contribution of the sulfur scatterer from Met92. At pH 7.2, there are 1.5–1.9 N at 2.01–2.03 Å and 0.5–1.2 S at 2.20–2.21 Å. At pH 4.8, all that can be stated with certainty is that there is 0.9–1.6 S at 2.13–2.17 Å.

The distances obtained from the pH 7.2 data differ from those found in crystal structure at pH 7.0, where the 2 N's are found at 2.15 Å and 2.37 Å. Attempts to find a fit with 2 N-waves at these distances failed; reasonable fits found the N's at 2.11/2.59 Å, or possibly 2.11/2.04 Å. So the Cu-ligand distances in our solution sample of reduced Pc at

high pH may truly differ from those found in the crystal structure, or perhaps the data range used for the fits is not sufficient to resolve the true distances of the ligands.

The other question we had was whether we could confirm that there is a shifting equilibrium between two extreme Cu–SMet bond lengths, rather than a gradual shift in the bond length itself, with pH. There are tantalizing indications that S from Met92 might indeed be found at two extreme positions, since two fit minima were found which placed it at either 2.3–2.4 Å or greater than 2.7 Å from Cu. However, since both these minima appeared in the data at high pH as well as at low pH, and also there was correlation with the N-wave in the low-pH data, these minima cannot be confirmed to be physically significant.

We have thus not been able to answer with certainty the questions that we posed at the beginning of this chapter. Indeed, it is doubtful that EXAFS analysis of Pc solutions, at least given the range and quality of the available data, can reliably discern a weak Cu-SMet interaction among so many other stronger contributions occurring at differing distances. It is possible that polarized EXAFS spectroscopy performed upon Pc crystals may be able to discern the methionine S at an orientation where the EXAFS contributions from the other coordinating atoms are reduced. Extreme care must be taken, however, to avoid being deceived by the sort of physically plausible, but not physically significant, solutions that we encountered in this study.

References

(1) Trebst, A. *A. Rev. Pl. Physiol.* **1974**, *25*, 423-458.

(2) Adman, E. T. In *Metalloproteins: Structural Aspects,* Academic Press, Inc.: New York, 1991; Vol. 42; pp 145-192.

(3) Gray, H. B.; Solomon, E. I. In *Copper Proteins*; T. G. Spiro, Ed.; Wiley: New York, 1980; pp 1-39.

(4) Solomon, E. I.; Penfield, K. W.; Wilcox, D. E. In *Copper, Molybdenum and Vanadium in Biological Systems*; P. Hemmerich; M. J. Clarke; J. B. Goodenough; J. A. Ibers; C. K. Jørgensen; J. B. Neilands; D. Reinen; R. Weiss and R. J. P. Williams, Ed.; Springer-Verlag: Berlin, 1983; Vol. 53; pp 1-57.

(5) Malmström, B. G. *Pure Appl. Chem.* **1969**, *24*, 393-406.

(6) Guss, J. M.; Freeman, H. C. *J. Mol. Biol.* **1983**, *169*, 521-563.

(7) Guss, J. M.; Harrowell, P. R.; Murata, M.; Norris, V. A.; Freeman, H. C. *J. Mol. Biol.* **1986**, *192*, 361-387.

(8) Guss, J. M.; Bartunik, H. D.; Freeman, H. C. *Acta Cryst.* **1992**, *B48*, 790-811.

(9) Shadle, S. E.; Penner-Hahn, J. E.; Schugar, H. J.; Hedman, B.; Hodgson, K. O.; Solomon, E. I. *J. Am. Chem. Soc.* **1993**, *115*, 767-776.

(10) Katoh, S.; Shiratori, I.; Takamiya, A. *J. Biochem. (Japan)* **1962**, *51*, 32-39.

(11) Segal, M. G.; Sykes, A. G. *J. Am. Chem. Soc.* **1978**, *100*, 4584-4592.

(12) Ellis, P. J., University of Sydney, Australia, personal communication.

(13) Stern, E. A.; Heald, S. M. *Rev. Sci. Instrum.* **1979**, *50*, 1579-1582.

(14) Clegg, W.; Acott, S. R.; Garner, C. D. *Acta Cryst.* **1984**, *C40*, 768-769.

(15) Kamara, R.; Declercq, J. P.; Germain, G.; Van Meerssche, M. *Bull. Soc. Chim. Belg.* **1982**, *91*, 339-340.

(16) Ottersen, T.; Warner, L. G.; Seff, K. *Inorg. Chem.* **1974**, *13*, 1904-1911.

Table 5.1. Least-squares fits to $Cu^{I}_2((CH_3NCH_2CH_2SSCH_2CH_2N(CH_3)_2)_2(BF_4)_2$ (CUNS2)

Waves used	Fit Type
N	1,2
S	1,2
N + S	(1,2)x3,(3)x2
N + N'	1,(2)x2
S + S'	(1,2)x2
N + N + S'	(2)x2,(3)

1 — Distances, coordination numbers and Debye-Waller factors are varied

2 — Distances, coordination numbers are varied while Debye-Waller factors (c_2 in the EXAFS equation) are fixed at initial (model) values

3 — Distances and Debye-Waller factors are varied while coordination numbers are fixed at various sets of values

( )x2 — 2 fit minima are explored

Table 5.2. Results of Type 2 fits (varying distances and coordination numbers while fixing Debye-Waller factors) made to $Cu^{I}_2((CH_3NCH_2CH_2SSCH_2CH_2N(CH_3)_2)_2(BF_4)_2$ (CUNS2). Fixed values of c_{2N} = -0.0253 and c_{2S} = -0.0216.

				Fit index†
N only :	5.2 N	@	2.13 Å	0.848
S only :	1.9 S	@	2.28 Å	0.354
N + S :	1.6 N	@	2.11 Å	0.134
	1.4 S	@	2.28 Å	
	5.2 N	@	2.13 Å	0.665
	0.6 S	@	2.65 Å	
	0.7 N	@	2.64 Å	0.301
	1.9 S	@	2.27 Å	
N + N' :	2.4 N	@	2.13 Å	0.848
	2.8 N'	@	2.13 Å	
	4.8 N	@	2.13 Å	0.432
	2.5 N'	@	2.51 Å	
S + S' :	-0.3 S	@	2.05 Å	0.172
	1.7 S'	@	2.28 Å	
	1.9 S	@	2.28 Å	0.322
	0.2 S'	@	2.76 Å	
N + N' + S	2.4 N	@	2.13 Å	0.035
	-1.8 N'	@	2.30 Å	
	0.7 S	@	2.29 Å	
	1.2 N	@	2.11 Å	0.134
	0.4 N'	@	2.11 Å	
	1.4 S	@	2.28 Å	

† — The fit index (F) is defined in Chapter 2.

Table 5.3. Fourier transform windows filtering data used in curvefitting of reduced Pc data

Data set	Window 0	Window 1	Window 2	Window 3
PCHI	1.20–2.12 Å	1.20–2.45 Å	1.20–2.85 Å	0.85–2.45 Å
PCLO	1.25–2.12 Å	1.25–2.40 Å	1.25–3.05 Å	0.85–2.40 Å

Table 5.4. Fits made to reduced Pc data at pH 7.2 (PCHI) and pH 4.8 (PCLO)

		Window 0	Window 1	Window 2	Window 3
N	PCHI	1,2	1,2	1,2	
	PCLO	1,2	1,2	1,2	
S	PCHI	1,2	1,2	1,2	
	PCLO	1,2	1,2	1,2	
N+S	PCHI	1,2	1,2,3	1,2,3	1,2,3
	PCLO	1,2	(1,2,3)x2	1,3,(2)x2	1,2,3
N+N'	PCHI	1,2	(1,2)x2	(1,2)x2	
	PCLO	1,2	(1,2)x2	(1,2)x2	
S+S'	PCHI	1,2	(1,2)x2	(1,2)x2	
	PCLO	1,2	(1,2)x2	(1,2)x2	
N+S+S'	PCHI		(2,3)x2	(2,3)x2	(2,3)x2
	PCLO		(2,3)x2	(2,3)x2	(2,3)x2
N+S+N'	PCHI		2,3	2,3	
	PCLO		(2,3)x2	(2)x3,(3)x2	
N+N'+S	PCHI				2,3
	PCLO				
N+N'+S+S'	PCHI				2,3
	PCLO				

1 — Distances, coordination numbers and Debye-Waller factors are varied

2 — Distances, coordination numbers are varied while Debye-Waller factors (c_2 in the EXAFS equation) are fixed at initial (model) values

3 — Distances and Debye-Waller factors are varied while coordination numbers are fixed at various sets of values

( )x2 — 2 fit minima are explored

Table 5.5. Two-wave Type 2 fits (varying distances and coordination numbers while keeping Debye-Waller factors fixed) to reduced Pc at pH 7.2 (PCHI) and pH 4.8 (PCLO). Fixed values of c_{2N} = -0.0253 and c_{2S} = -0.0216.

	Reduced Pc, pH 7.2			Reduced Pc, pH 4.8		
	Window 0		Fit Index	**Window 0**		Fit Index
N + S	1.9 N @ 0.5 S @	2.03 Å 2.20 Å	0.098	-0.3 N @ 0.9 S @	1.85 Å 2.16 Å	0.173
N + N'	0.7 N @ 3.7 N' @	1.87 Å 2.05 Å	0.156	0.6 N @ 1.9 N' @	2.02 Å 2.02 Å	0.400
S + S'	1.3 S @ 0.6 S' @	2.18 Å 2.33 Å	0.144	1.1 S @ 0.3 S' @	2.16 Å 2.35 Å	0.096
	Window 1		Fit Index	**Window 1**		Fit Index
N + S	1.9 N @ 0.5 S @	2.03 Å 2.20 Å	0.167	1.9 N @ 1.4 S @	2.16 Å 2.14 Å	0.094
				-0.4 N @ 0.9 S @	1.86 Å 2.16 Å	0.233
N + N'	0.8 N @ 3.7 N' @	1.87 Å 2.05 Å	0.219	2.6 N @ 0.9 N' @	2.03 Å 2.35 Å	0.324
	3.1 N @ 0.5 N' @	2.04 Å 2.73 Å	0.336	2.6 N @ 0.4 N' @	2.02 Å 2.68 Å	0.427
S + S'	1.4 S @ 0.5 S' @	2.18 Å 2.35 Å	0.221	1.2 S @ 0.4 S' @	2.17 Å 2.37 Å	0.076
	1.1 S @ 0.2 S' @	2.19 Å 2.89 Å	0.428	0.9 S @ 0.1 S' @	2.16 Å 2.78 Å	0.272
	Window 2		Fit Index	**Window 2**		Fit Index
N + S	1.9 N @ 0.5 S @	2.03 Å 2.20 Å	0.201	2.1 N @ 1.4 S @	2.17 Å 2.15 Å	0.163
				-0.4 N @ 0.9 S @	1.86 Å 2.16 Å	0.289
N + N'	0.8 N @ 3.7 N' @	1.87 Å 2.05 Å	0.236	2.6 N @ 0.9 N' @	2.03 Å 2.35 Å	0.356
	3.1 N @ 0.4 N' @	2.04 Å 2.75 Å	0.357	2.6 N @ 0.3 N' @	2.02 Å 2.68 Å	0.463
S + S'	1.4 S @ 0.5 S' @	2.18 Å 2.35 Å	0.239	1.2 S @ 0.4 S' @	2.17 Å 2.37 Å	0.154
	1.1 S @ 0.1 S' @	2.19 Å 2.96 Å	0.454	0.9 S @ 0.1 S' @	2.16 Å 2.74 Å	0.326
	Window 3		Fit Index	**Window 3**		Fit Index
N + S	1.9 N @ 0.5 S @	2.03 Å 2.20 Å	0.375	2.4 N @ 1.5 S @	2.16 Å 2.14 Å	0.336

Table 5.6. Three-wave Type 2 fits (varying distances and coordination numbers while keeping Debye-Waller factors fixed) to PCHI and PCLO. Fixed values of c_{2N} = -0.0253 and c_{2S} = -0.0216.

	Reduced Pc, pH 7.2			Reduced Pc, pH 4.8		
	Window 1			**Window 1**		
			Fit Index			Fit Index
N + S + S'	1.6 N @	2.01 Å	0.108	0.4 N @	2.02 Å	0.060
	0.8 S @	2.21 Å		1.0 S @	2.17 Å	
	0.3 S' @	2.42 Å		0.3 S' @	2.38 Å	
	1.8 N @	2.03 Å	0.135	1.5 N @	2.10 Å	0.059
	0.5 S @	2.20 Å		0.9 S @	2.13 Å	
	0.1 S' @	2.87 Å		0.1 S' @	2.80 Å	
N + S + N'	1.8 N @	2.03 Å	0.101	1.3 N @	2.09 Å	0.026
	0.5 S @	2.20 Å		0.8 S @	2.14 Å	
	0.5 N' @	2.71 Å		0.4 N' @	2.66 Å	
				1.5 N @	2.12 Å	0.079
				1.2 S @	2.14 Å	
				0.4 N' @	2.23 Å	
	Window 2			**Window 2**		
			Fit Index			Fit Index
N + S + S'	1.5 N @	2.01 Å	0.147	0.3 N @	2.02 Å	0.149
	0.8 S @	2.21 Å		1.0 S @	2.17 Å	
	0.3 S' @	2.41 Å		0.3 S' @	2.38 Å	
	1.9 N @	2.03 Å	0.181	2.3 N @	2.19 Å	0.149
	0.5 S @	2.20 Å		1.5 S @	2.16 Å	
	0.1 S' @	3.02 Å		0.1 S' @	2.70 Å	
N + S + N'	1.9 N @	2.03 Å	0.179	2.2 N @	2.17 Å	0.127
	0.5 S @	2.20 Å		1.5 S @	2.15 Å	
	0.4 N' @	2.72 Å		0.5 N' @	2.92 Å	
				2.3 N @	2.21 Å	0.156
				1.6 S @	2.16 Å	
				0.3 N' @	2.55 Å	
				1.7 N @	2.13 Å	0.155
				1.2 S @	2.14 Å	
				0.4 N' @	2.24 Å	
	Window 3			**Window 3**		
			Fit Index			Fit Index
N + S + S'	1.0 N @	1.99 Å	0.317	0.4 N @	1.85 Å	0.301
	1.2 S @	2.20 Å		1.4 S @	2.17 Å	
	0.5 S' @	2.39 Å		0.6 S' @	2.37 Å	
	1.8 N @	2.03 Å	0.360	2.3 N @	2.15 Å	0.334
	0.5 S @	2.20 Å		1.4 S @	2.14 Å	
	0.1 S' @	2.88 Å		0.1 S' @	2.81 Å	

Table 5.7. Results of some Type 3 fits (varying distances and Debye-Waller factors while keeping coordination numbers fixed) to reduced Pc at high pH (PCHI) and low pH (PCLO).

Reduced Pc, pH 7.2				Reduced Pc, pH 4.8			
Window 1				**Window 1**			
	R	c_2	F		R	c_2	F
2 N	2.08	-0.0322	0.140	1 N	2.14	-0.0238	0.139
1 S	2.17	-0.0254		1 S	2.15	-0.0204	
2 N	2.06	-0.0374	0.066	1 N	1.75	-0.0980	0.039
1 S	2.18	-0.0243		1 S	2.15	-0.0206	
1 S'	2.37	-0.0623		1 S'	2.32	-0.0420	
2 N	2.08	-0.0329	0.082	1 N	2.15	-0.0244	0.096
1 S	2.17	-0.0251		1 S	2.15	-0.0201	
1 S'	2.92	-0.0661		1 S'	2.84	-0.0697	
Window 2				**Window 2**			
	R	c_2	F		R	c_2	F
2 N	2.08	-0.0322	0.175	1 N	2.14	-0.0224	0.204
1 S	2.17	-0.0251		1 S	2.14	-0.0199	
2 N	2.06	-0.0373	0.102	1 N	1.80	-0.1086	0.146
1 S	2.18	-0.0242		1 S	2.15	-0.0203	
1 S'	2.37	-0.0614		1 S'	2.33	-0.0407	
2 N	2.08	-0.0319	0.088	1 N	2.20	-0.0061	0.162
1 S	2.17	-0.0254		1 S	2.16	-0.0119	
1 S'	2.98	-0.0609		1 S'	2.98	-0.0819	
Window 3				**Window 3**			
	R	c_2	F		R	c_2	F
2 N	2.07	-0.0333	0.331	1 N	2.12	-0.0172	0.377
1 S	2.17	-0.0253		1 S	2.13	-0.0204	
2 N	2.03	-0.0438	0.258	1 N	1.90	-0.0359	0.291
1 S	2.18	-0.0225		1 S	2.16	-0.0185	
1 S'	2.35	-0.0476		1 S'	2.34	-0.0328	
2 N	2.07	-0.0333	0.302	1 N	2.11	-0.0165	0.355
1 S	2.17	-0.0250		1 S	2.13	-0.0207	
1 S'	2.92	-0.0624		1 S'	2.86	-0.0651	

Table 5.8. Type 2 (varying R's and CN's) and Type 3 (varying R's and c_2's) fits to Window 3 of reduced Pc at pH 7.2 (PCHI), made to compare with the distances found in the crystal structure at pH 7.0. Fixed values of c_{2N} = -0.0253 and c_{2S} = -0.0216.

N+N'+S			**N+N'+S+S'**		
Only R's varied			**Only R's varied**		
		Fit Index			Fit Index
1 N @	2.11 Å	0.477	1 N @	2.11 Å	0.419
1 N' @	2.63 Å		0.6 N' @	2.59 Å	
1 S @	2.17 Å		1 S @	2.17 Å	
			0.13 S' @	2.91 Å	
Type 2 fits (R's and CN's varied)			**Type 2 fits (R's and CN's varied)†**		
		Fit Index			Fit Index
8.4 N @	2.07 Å	0.215	(1 N) @	2.09 Å	0.347
2.3 N' @	2.34 Å		-0.9 N' @	2.37 Å	
1.5 S @	2.03 Å		(1 S) @	2.17 Å	
			0.2 S @	2.90 Å	
Type 3 fits (R's and c_2's varied)			**Type 3 fits (R's and c_2's varied)‡**		
	R	c_2 Fit Index		R	c_2 Fit Index
1 N	@ 2.11 Å	-0.0267 0.331	1 N	@ 2.11 Å	(-0.0253) 0.398
1 N'	@ 2.04 Å	-0.0326	1 N'	@ 2.59 Å	-0.0340
1 S	@ 2.17 Å	-0.0255	1 S	@ 2.17 Å	(-0.0216)
			1 S'	@ 2.95 Å	-0.0497

† — CN's enclosed in brackets (e.g., (1 N)) were not varied

‡ — c_2's enclosed in brackets were not varied

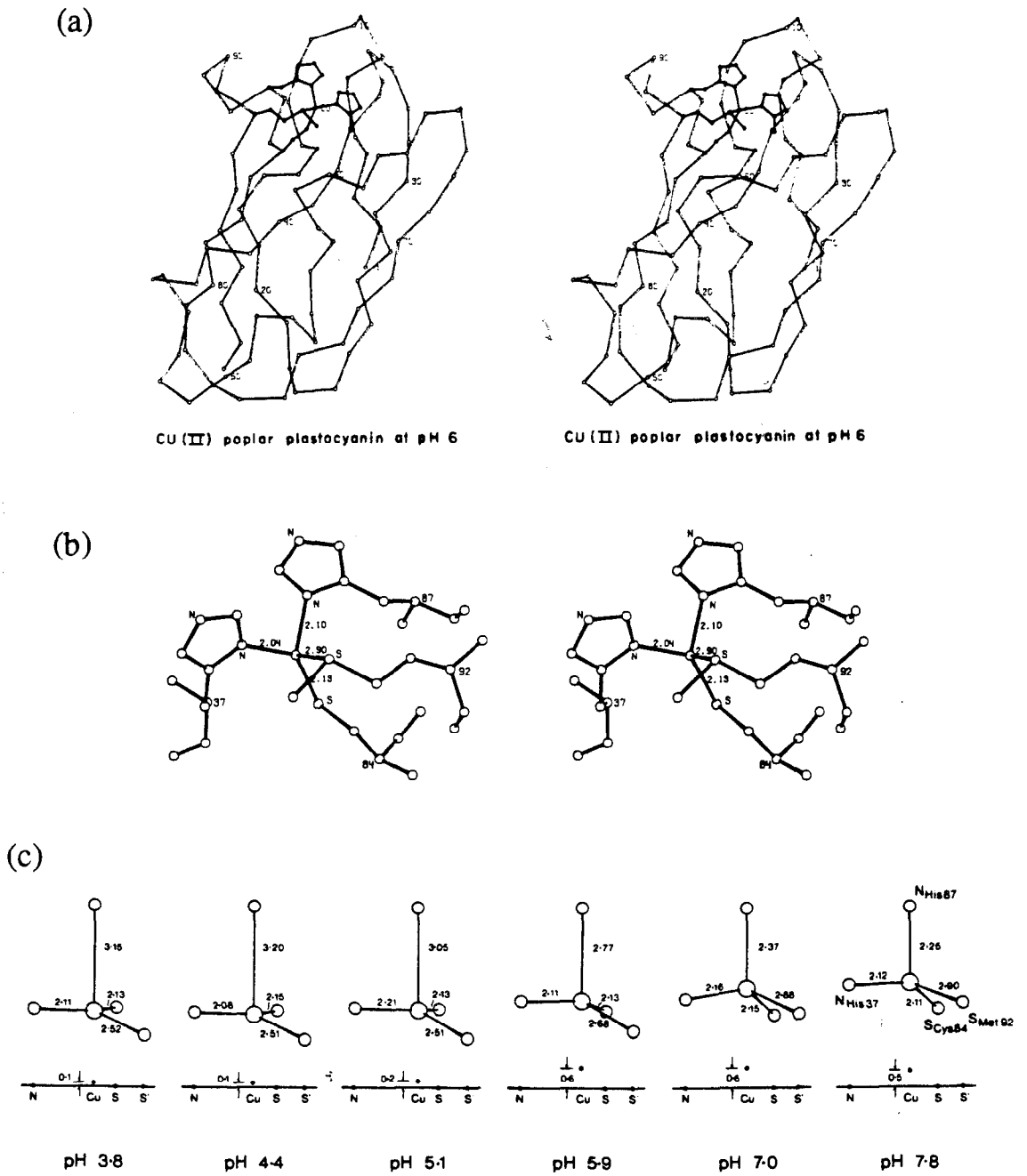

Figure 5.1. (a) A stereoview of the C_α framework of Poplar Cu^{II}-plastocyanin. The Cu-binding residues are drawn in black. (b) Stereoview of the Cu site in Cu^{II}-plastocyanin, showing all non-hydrogen atoms of each ligand residue. (c) Dimensions (in Å) of the copper site in reduced plastocyanin at six pH values. The lower portion of each diagram shows the deviation of the Cu atom from a plane fitted to N–His37, S–Cys84 and S–Met92. (Parts (a) and (b) are reproduced from *J. Mol. Biol.* **1983**, *169*, 521–563 and part (c) from *J. Mol. Biol.* **1986**, *192*, 361–387, by courtesy of H. C. Freeman.)

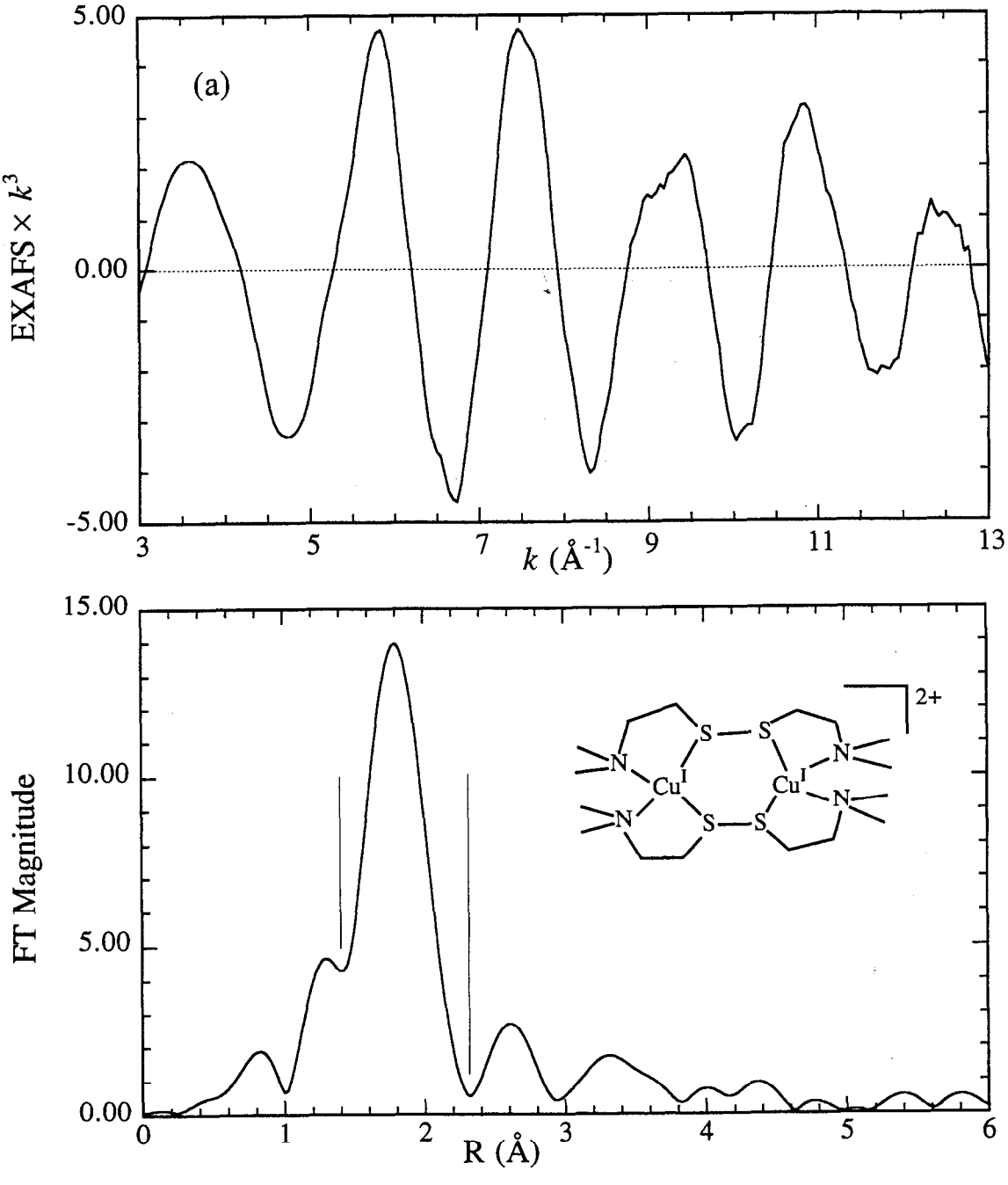

Figure 5.2. EXAFS data and Fourier transform for $Cu^I_2((CH_3NCH_2CH_2SSCH_2CH_2N(CH_3)_2)_2(BF_4)_2$ (CUNS2). Top : Averaged EXAFS data for $Cu^I_2((CH_3NCH_2CH_2SSCH_2CH_2N(CH_3)_2)_2(BF_4)_2$ (CUNS2), with spline applied up to k = 13 Å^{-1}. Bottom : Fourier transform over k = 3.5–12.5 Å^{-1}, with vertical lines showing the Fourier backtransform window (R = 1.35–2.35 (0.1) Å) used to filter data for curvefitting.

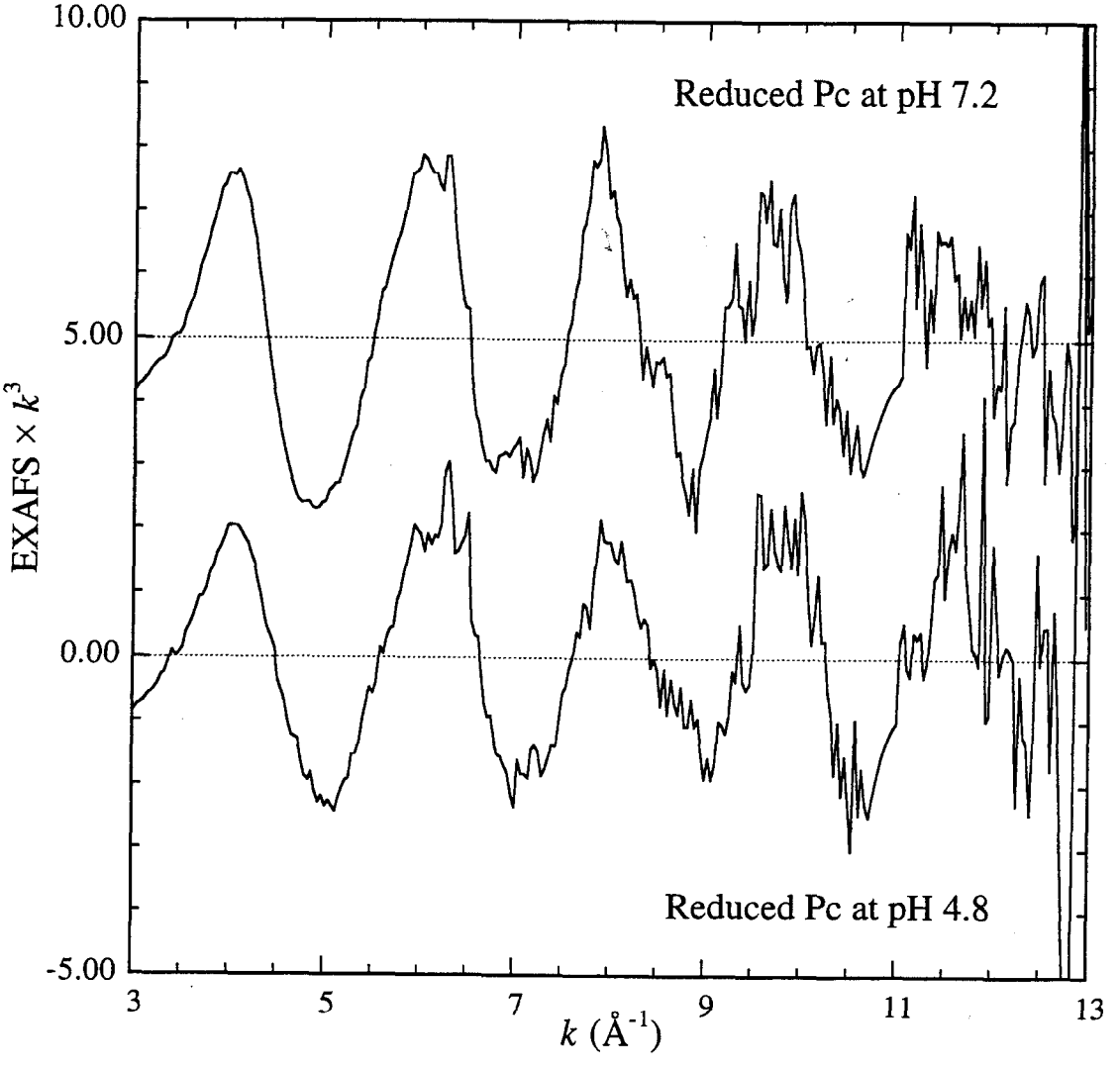

Figure 5.3. EXAFS data and Fourier transform for reduced Pc at pH 7.2 and 4.8. Top : Averaged EXAFS data for reduced Pc at pH 7.2 (PCHI). Bottom : EXAFS data for reduced Pc at pH 4.8 (PCLO). A glitch at k = 10.9 Å^{-1} was removed from both spectra.

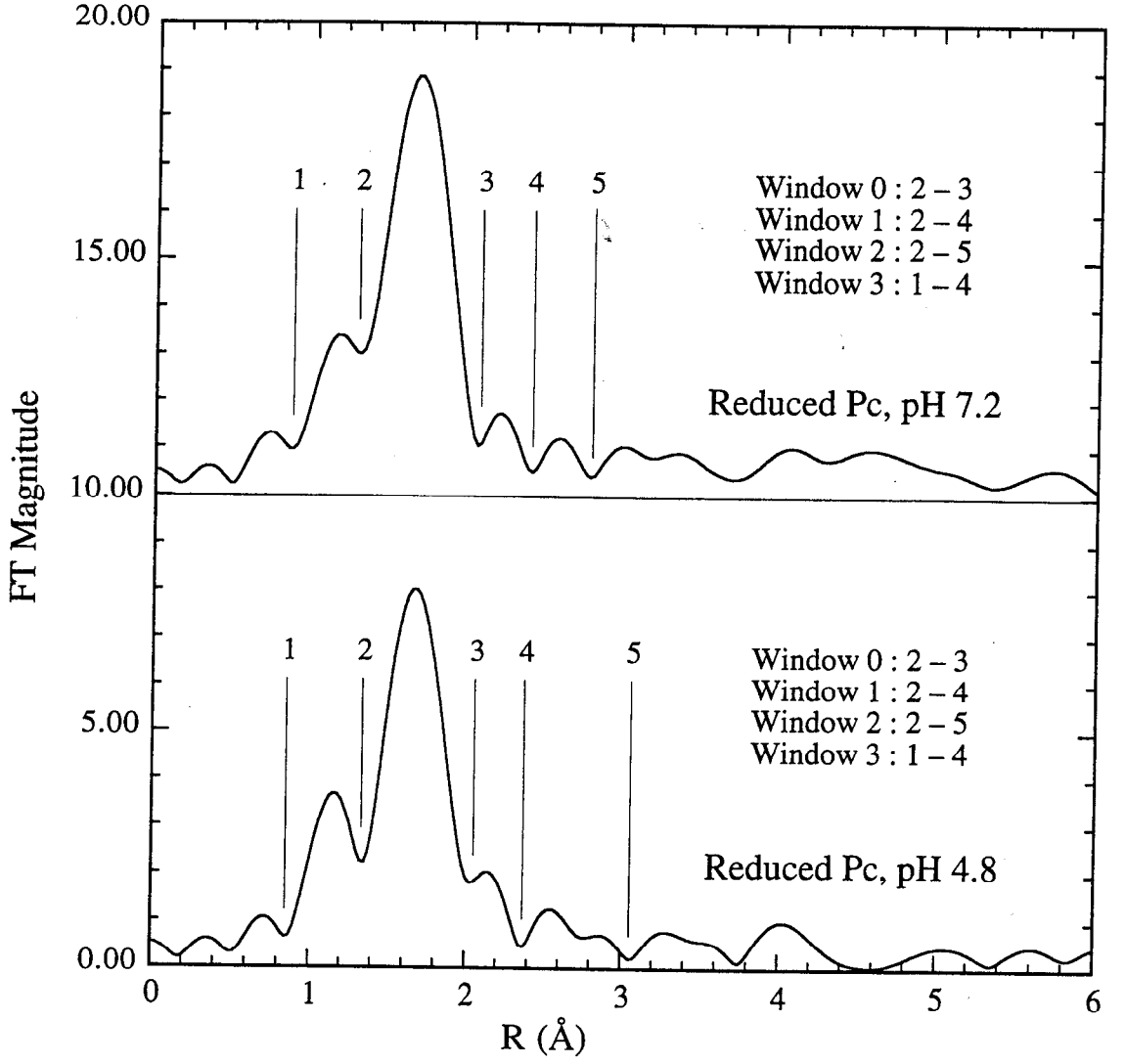

Figure 5.4. Reduced Pc EXAFS data Fourier-transformed over k = 3.5–12.5 (0.1) Å^{-1}. Vertical lines show the Fourier backtransform windows used to filter the data for curvefitting (see also Table 5.3). Top : Reduced Pc at pH 7.2 (PCHI). Bottom : Reduced Pc at pH 4.8 (PCLO).

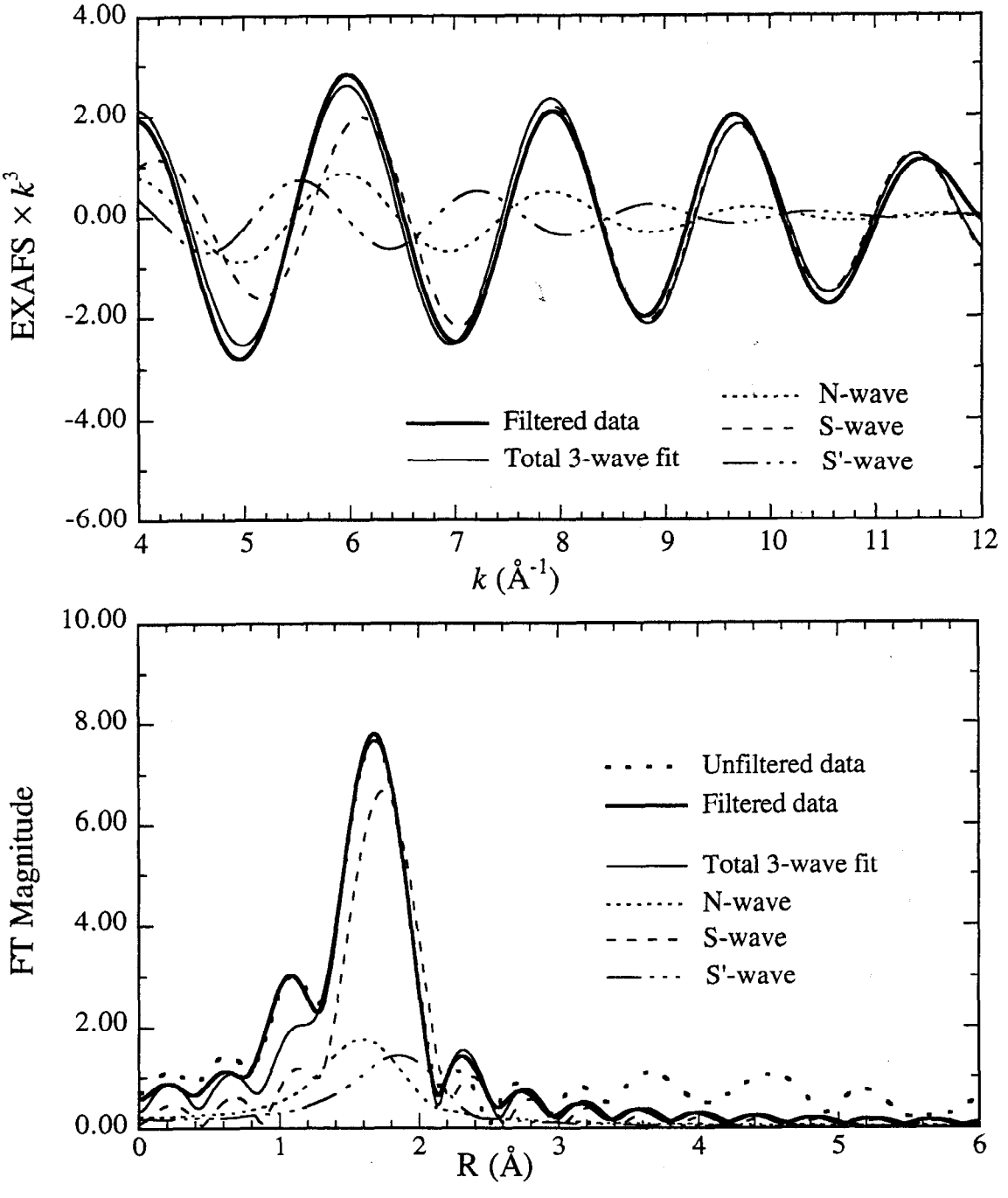

Figure 5.5. N+S+S' fit (short-S' minimum) to Pc data at pH 7.2 (PCHI). Top : Backtransformed PCHI data (Window 3), with the components of the short-S' minimum of the N+S+S' fit (Type 3) and the total fit. Bottom : Fourier transforms over k = 4.25–11.75 (0.1) Å^{-1} of the data and fit components shown above.

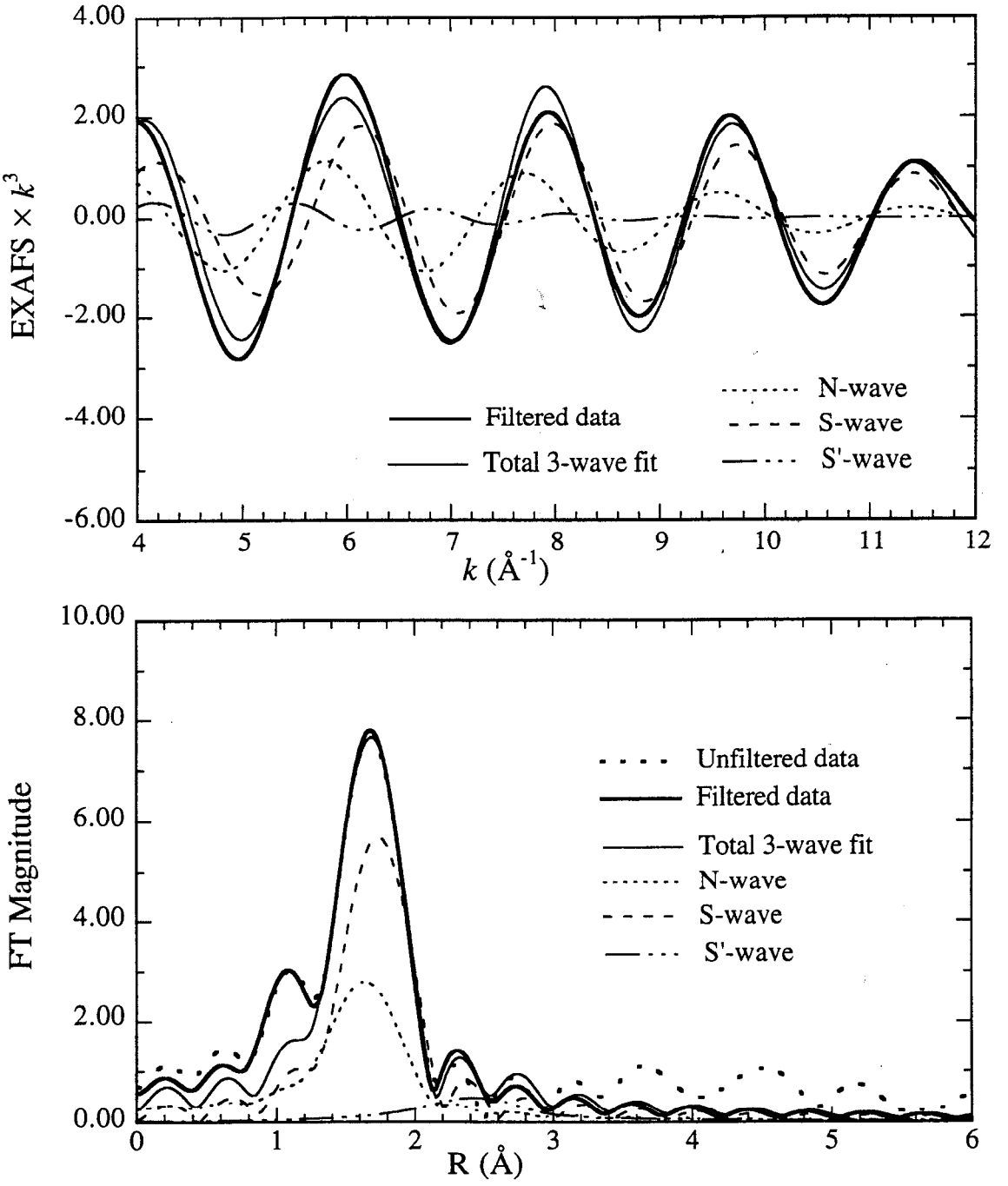

Figure 5.6. N+S+S' fit (long-S' minimum) to Pc data at pH 7.2 (PCHI). Top : Backtransformed PCHI data (Window 3), with the components of the long-S' minimum of the N+S+S' fit (Type 3) and the total fit. Bottom : Fourier transforms over k = 4.25–11.75 (0.1) Å^{-1} of the data and fit components shown above.

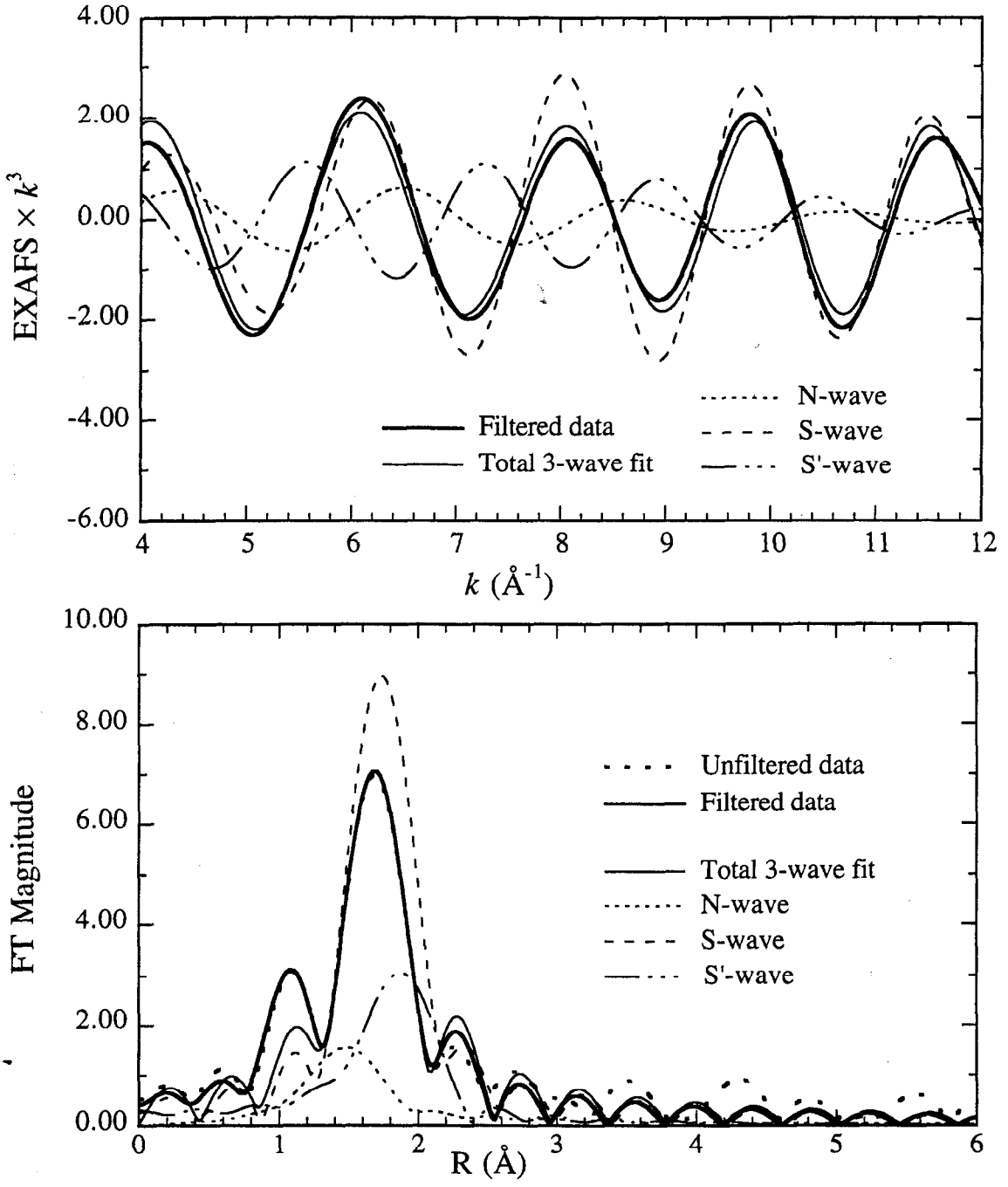

Figure 3.7. N+S+S' fit (short-S' minimum) to Pc data at pH 4.8 (PCLO). Top : Backtransformed PCLO data (Window 3), with the components of the short-S' minimum of the N+S+S' fit (Type 3) and the total fit. Bottom : Fourier transforms over k = 4.25–11.75 (0.1) Å^{-1} of the data and fit components shown above.

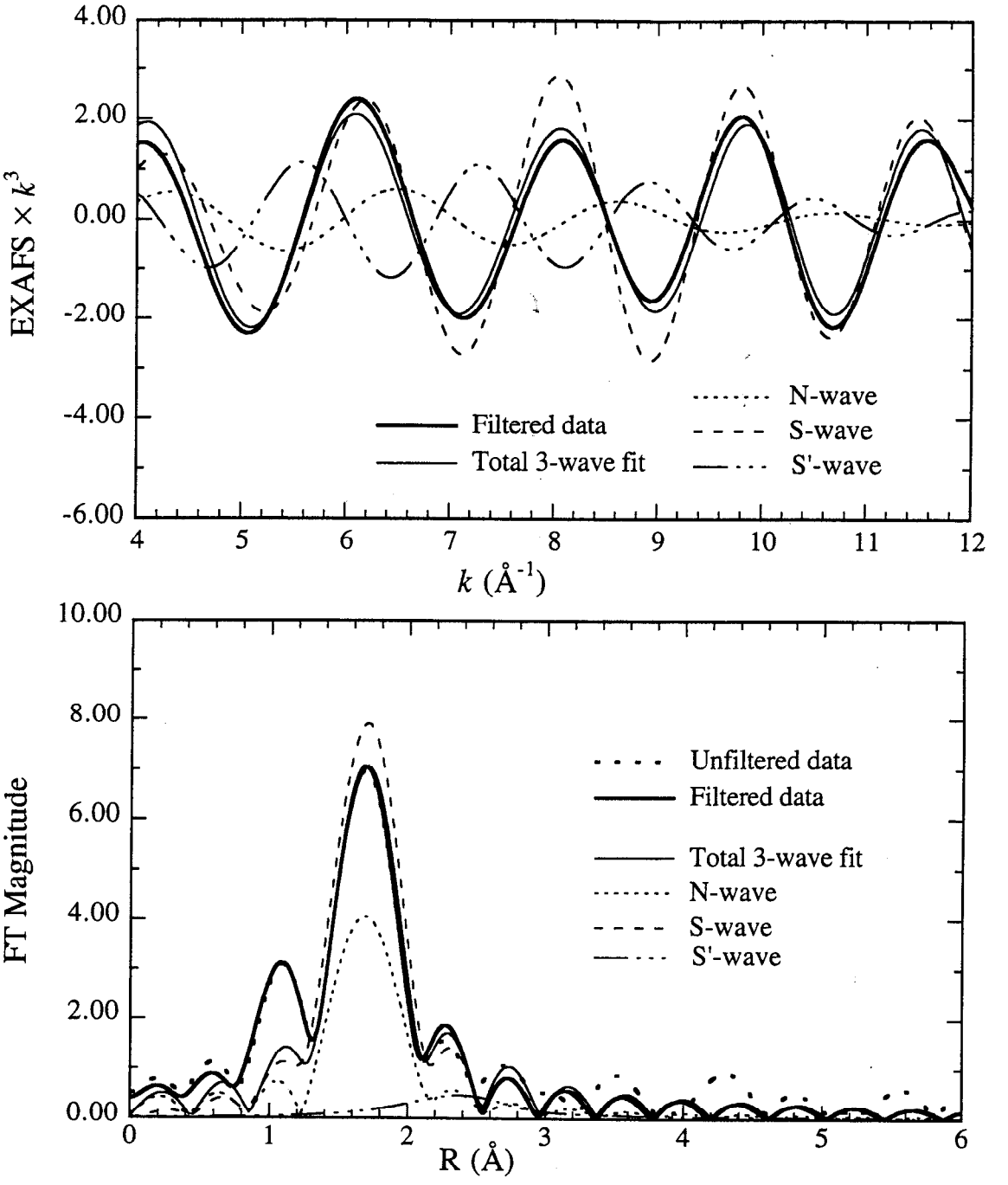

Figure 5.8. N+S+S' fit (long-S' minimum) to Pc data at pH 4.8 (PCLO). Top : Backtransformed PCLO data (Window 3), with the components of the long-S' minimum of the N+S+S' fit (Type 3) and the total fit. Bottom : Fourier transforms over k = 4.25–11.75 (0.1) Å^{-1} of the data and fit components shown above.

Chapter 6

Cu Difference Edge Analysis of *Rhus vernicifera* Laccase — A Continuing Study

(A) A Brief Overview of the Structure and Function of Laccase

(1) Structure and General Reaction Mechanism of Laccase

The multicopper oxidases (laccase, ascorbate oxidase and ceruloplasmin) catalyze the four-electron reduction of dioxygen to water. Laccase is the simplest of these, and it may be found in trees, or in fungi. *Rhus vernicifera* laccase comes from the Japanese lacquer tree, where the reduction of dioxygen to water occurs concommitantly with the oxidation of quinones and catechols in tree sap to radicals which then polymerize, hardening the sap into lacquer. In fungi, laccase, in concert with other fungal enzymes, serves the opposite function of degrading tree lignin.

Each unit of laccase contains four copper atoms, named according to their spectral characteristics : one Type 1 (T1) "blue" copper ($\lambda_{max} \cong 610$ nm, $A_{\|} \leq 95 \times 10^{-4}$ cm^{-1}), one Type 2 (T2) "normal" copper (no known UV-visible absorption band, $A_{\|} > 140 \times 10^{-4}$ cm^{-1}) and two Type 3 (T3), in a coupled binuclear site ($\lambda_{max} \cong 330$ nm, EPR undetectable). Spectroscopic studies of laccase and ascorbate oxidase showed that the T2 and T3 Cu were so close to each other as to form a single trinuclear site.[1-6] This is supported by a recent crystal structure of ascorbate oxidase,[7,8] in which the T1 Cu is 12.2–14.9 Å away from the other three Cu ions, while the T2 and T3 Cu ions form a triangle, with all three Cu ions being within 3.9 Å of each other. The T1 site is linked to the trinuclear site through the amino acid sequence His506–Cys507–His508; the His are each ligated to one of the T3 Cu, while the Cys is ligated to the T1 Cu.

The reaction cycle of laccase may be divided into a reduction leg and an oxidation leg.[9] Each leg can be studied separately, the reduction leg in the presence of anaerobic substrate (catechol, etc.) and the oxidation leg in the presence of dioxygen. In the reduction leg, the T1 Cu receives electrons from the substrate and passes them to the other three Cu. The exact sequence in which the reduction of all the Cu's occurs is pH-dependent.[9] Our studies are concerned with elucidating details of the oxidation leg. In this part of the cycle, dioxygen binds to fully reduced laccase at the trinuclear site. Three electrons are very rapidly transferred to it, so that it forms an "oxygen intermediate" (indicated by an optical absorption band near 360 nm), and at the same time the T1 Cu is reoxidized.[10-12] The oxygen intermediate decays slowly ($t_{1/2}$ ~ 1 to 15 s), and there is a corresponding growing in of the EPR signal due to oxidized T2 Cu.[5] A mass spectroscopic study of the reaction of laccase with $^{18}O_2$ shows that one water molecule is released quickly, but the second oxygen remains bound and is slowly exchanged with the bulk solution with $t_{1/2}$ ~ 30 minutes.[4]

It thus seems clear that, upon binding of O_2 to the trinuclear site, three electrons are quickly transferred to it from the T1 and T3 Cu's. However, the apparent oxidation of the T2 Cu is too slow to be catalytically relevant, and so it was suggested that the T1 Cu was re-reduced and that the fourth electron required to completely reduce O_2 was donated from T1. Nevertheless, there is evidence that T2 Cu has a role to play; both it and the T3 Cu ions are affected when azide is bound to the trinuclear site,[1,2] and the second water molecule formed in the reduction remains bound to the T2 Cu.[6] (A recent study suggests that in the oxygen intermediate the oxygen species has been reduced by four electrons rather than three, and that the fourth electron may come from the T2 Cu.[13])

To shed light on this matter, two enzymatically inactive derivatives of native (four-Cu) laccase have been studied; in one derivative (Type 2-depleted or T2D laccase) the T2 Cu has been removed, and in the other (T1Hg laccase) the T1 Cu has been replaced with Hg. The T1Hg laccase derivative is particularly interesting because it, like native laccase, exhibits an absorption band (at 340 nm rather than 360 nm) due to an oxygen intermediate ($t_{1/2} = 6.4 \pm 2$ min.) when the fully reduced form is exposed to air.[14] Enzymatically active native laccase can easily be reconstituted from T2D laccase, or, indeed, from apo laccase (all four Cu removed) by adding Cu ions. However, it is not possible reconstitute native laccase once Hg has bound to the T1 site.

(2) The Usefulness of X-ray Edge Analysis; Previous Work on Laccase

When probed with optical, MCD or EPR spectroscopy, Cu(I) gives no signal (except for metal-to-ligand charge transfers), since it has a completely filled 3d shell (i.e., $3d^{10}$). Furthermore, the T3 Cu ions in laccase give no EPR signal, even when they are oxidized, because they are then antiferromagnetically coupled, and the T2 Cu has no known UV-visible band in any oxidation state. However, the X-ray absorption edges of Cu(I) compounds can be easily differentiated from those of Cu(II) compounds, and furthermore show features, especially at ~8984 eV, that allow determination of the Cu coordination geometry (see Figure 6.1).

Kau, *et al.*[15] showed that the feature at 8984 eV is a sharp spike for linear two-coordinated Cu(I) compounds, and appears as a shoulder of significant amplitude for three- and four-coordinated compounds (Figure 6.1). The differences in the edges of the three- and four-coordinated compounds can be more accurately discerned by subtracting the edge of a standard Cu(II) compound from the Cu(I) edge and examining the resulting derivative-shaped "difference edge" (Figure 6.2); the difference edges of three-coordinate compounds

show a peak at 8983-8984 eV, while those of four-coordinate compounds show no peak below 8985 eV.

Cu(II) edges show a weak 1s→3d transition at ~8979 eV. Also, the rising edge occurs at higher energy, and so the edge amplitude at 8984 eV is much lower. The covalency of the Cu(II)–ligand bond can be judged from the position of the rising edge; the lower the energy at which it occurs, the greater the covalency of the bond, because the electrons then donated by the ligand lower the effective nuclear charge of Cu. There is some overlap between the possible edge shapes of four-coordinate Cu(I) compounds and those of covalent Cu(II) compounds. In such cases, the 1s→3d transition, together with other methods of spectroscopy, should also be relied on to determine the oxidation state and ligation of Cu.

Besides determining the geometry of reduced Cu (i.e., Cu(I)), difference edges can be used to determine the proportion of reduced Cu in a sample. For example, in previous work done by this group,[15] it was determined that the T3 Cu are 98 ± 22% reduced in resting (i.e., as-prepared) T2D, with three- or (2+4)-coordination, and that oxidation of T3 (as opposed to the formation of a peroxy complex) increases proportionately as T2D is treated with increasing excess (up to 60×) of H_2O_2. This showed that resting T2D laccase does not react with O_2. The same study found that, in resting native laccase, the T3 sites are 22 ± 3% reduced, being completely oxidized upon addition of 30× H_2O_2.

(3) EXAFS Studies on Laccase

Some EXAFS studies have been carried out on laccase. In 1983, Spira *et al.*[16] studied the EXAFS spectrum of met T2D (i.e., oxidized T2D laccase with no O_2 bound) and azide-treated met T2D laccase. In both samples, they found 3.0–3.5 N at 1.99–2.00 Å and 0.33 S at 2.07 or 2.09 Å. When the contribution of the T1 Cu, approximated by a plastocyanin EXAFS spectrum, was subtracted, they found 3.2–3.5 N at 2.01–2.02 Å, and the contribution from S was 0.13 or less. They concluded that 1 S was bound to the T1 site (which is consistent with the subsequent crystal structures of plastocyanin and ascorbate oxidase, since the second Cu–S bond is extremely long). Comparison with the EXAFS results from the Cu binuclear protein, hemocyanin, showed that the N/O-ligation found for the T3 Cu's was similar, but unlike for hemocyanin the T3 site was not much perturbed by the binding of azide, and they could not find any Cu closer than 3.8 Å.

In 1984, Woolery, *et al.*[17] studied the EXAFS of oxidized and reduced native laccase and also the resting (as-prepared) and H_2O_2-oxidized forms of T2D laccase. They made fits to the first shell (i.e. the shell of scatterers directly coordinated to Cu), and obtained results

agreeing with those of Spira, *et al.*, though 0.3 S was found at 2.19 Å rather than 2.09 Å (this difference is within the experimental error, because the contribution of S is small). For both forms of laccase, oxidized and reduced forms gave the same total coordination. The outer-shell EXAFS signals (R = 3–4 Å), were fitted with an imidazole outer-shell wave and a Cu wave. They were able to account for the outer-shell EXAFS of both forms of T2D laccase using imidazole alone, but they needed both imidazole and Cu (0.5 Cu at 3.4 Å) to obtain a good fit of the native laccase outer-shell EXAFS. They thus concluded that the removal of the T2 Cu causes a change in the T3 site, with the two Cu ions perhaps moving further apart from each other.

More recently (1989), Klemens, *et al.*[18] studied the Hg-substituted blue copper site in plastocyanin, azurin, laccase and stellacyanin using EXAFS at the Hg L_3 edge. They provided the first direct evidence that, when incorporated, the Hg occupies only the T1 site, and that T1 coordination in all four proteins was two imidazole groups and one thiolate sulfur. Furthermore, when considered together with the results for the crystal structure of Hg-substituted plastocyanin, the data showed that the coordination geometry in the T1 site was the same, whether Cu or Hg was bound. This confirmed the usefulness of the T1Hg derivative for the study of laccase.

(B) Experimental Details

(1) Preparation of Samples

Rhus vernicifera laccase was isolated from acetone powder (Saito and Co., Osaka, Japan) to a purity ratio of A_{280}/A_{614} = 14.5–15.5.[19] Laccase activity was assayed spectrophotometrically with *N,N*-dimethyl-*p*-phenylenediamine as the substrate. T2D laccase was prepared according to the procedure of Graziani, *et al.*,[20] as modified by Spira-Solomon and Solomon.[19] T1Hg laccase was prepared according to published procedures,[21,22] as modified by Cole, *et al.*[14] Reduction of T2D laccase was carried out in a N_2-purged cuvette by adding 2 equivalents of ascorbate. T1Hg laccase was reduced by anaerobic dialysis against 5 mM dithionite, and excess dithionite was removed by anaerobic dialysis against 0.1 M potassium phosphate buffer (the buffer used for all samples) of pH 7.4 (unless otherwise stated), before the protein was transferred into a cuvette for optical absorption measurements. An aliquot each of fully reduced T2D and T1Hg was transferred under Ar into XAS protein cells (outer dimensions $2 \times 4 \times 28$ mm^3, volume ~180 µl, with an X-ray-transparent front face of 60 µm Mylar tape) and frozen in liquid N_2. Both T2D and T1Hg laccase were then reoxidized by exposing the cuvette to air, and at the time points indicated in Table 6.1, UV-visible spectra were measured, and aliquots of protein

were withdrawn and frozen in lucite XAS cells. EPR spectra were measured on the frozen samples both before and after measuring the XAS spectra, and UV-visible spectra were also re-recorded after thawing the samples to 298 K. For the study on the T1Hg laccase oxygen intermediate, reoxidation of the fully reduced T1Hg laccase was initiated by addition of dioxygen-saturated buffer, and aliquots were withdrawn and frozen in the same manner. For the study on the native laccase oxygen intermediate, dioxygen-saturated buffer and reduced laccase were simultaneously injected into the XAS protein cell, which was then frozen within a few seconds. Several repeat samples of both types of oxygen intermediates were prepared.

(2) Data Collection

Laccase edge data were collected at the Stanford Synchrotron Radiation Laboratory in five sessions from 1987 to 1991 (see Table 6.1), at the unfocussed 8-pole wiggler beam line 7-3 in fluorescence mode, using a Lytle detector[23] with a nickel filter, and argon gas in the chamber, except in March 1989, when N_2 gas was mistakenly used. (N_2 gas is not as readily ionized as Ar gas by Cu Kα fluorescence, and so gives a smaller and noisier signal.) Ring current on these occasions varied between 8 and 69 mA. To maintain consistency with data previously collected, all spectra were run using Si[220] monochromator crystals and a vertical monochromator slit width of 2 mm. The temperature of the samples during data collection was either 10–12 K or 85 K. (The temperature made no difference to the appearance of the edges.) Scans to $k = 9$ Å^{-1} were collected, except in December 1987, when scans were collected to $k = 8$ Å^{-1}. The number of scans collected depended on the concentration of the sample, the ring current at the time, and whether any photoreduction was observed. Photoreduction (manifested by an increase in the edge amplitude at 8984 eV) was not observed in any of the samples of native and T2D laccase. However, it was significant (~1% per scan) in many of the samples of T1Hg laccase (those containing glycerol; see Table 6.1), and only the first scans of these samples were used in subsequent analyses.

(3) Data Analysis

(a) Data Reduction

Data were reduced and analyzed using XFPAKG, in the manner described in Chapter 2. Scans were calibrated using copper foil as an internal standard, taking the first inflection point of the foil as 8980.3 eV. In the laccase samples where no photoreduction was observed, all good scans were averaged. In those T1Hg laccase samples where photoreduction occurred, only the first scan was used in the difference edge analysis.

All laccase spectra were normalized in exactly the same manner as spectra used in previous work : A polynomial of order -2 was fitted to 8770–8970 eV, the pre-edge region of the spectrum, then a one-region spline of order 1 was applied over 9045–9309 eV, or 9045–9243 eV (for spectra ending at $k = 8$ Å^{-1}).

(b) Corrections Applied to the Laccase Edges

In the process of preparing and fully reducing the Cu in the two derivatives, a certain amount of native laccase was reconstituted, and had to be taken into account during data analysis. The native laccase was assumed to be fully reduced before the samples were exposed to air, and then either 89% oxidized (in T2D samples) or fully oxidized (in T1Hg samples) once the samples had been exposed to air (see Table 6.2). The proportion of native laccase (x) remaining in "fully reduced" T2D and T1Hg laccase was determined by several methods : assaying laccase activity (in both T2D and T1Hg), monitoring the absorption band at 600 nm and the EPR signal due to oxidized T1 Cu (which is absent in T1Hg), and atomic absorption measurements (for T2D, where the ratio of copper found to the moles of protein could be solved for x, since native laccase has four copper atoms, while T2D has only three).

The proportion of T1Hg oxidized (y) in the "fully reduced" sample MLRD (*vide infra*) was deduced from quantitating the EPR signal due to oxidized T2 (z) and subtracting x. (So, $y = z - x$.) The EPR signal due to oxidized T2 was also used for determination of z and y for all T1Hg oxygen intermediate samples. See Table 6.2 for values of x and z that were determined for each sample measured.

All T2D and T1Hg laccase edges were "corrected for native" and renormalized in the following manner :

$$\text{Proportion of Cu edge signal due to native laccase} = \frac{\left(\frac{4}{3}\right)x}{\left[\left(\frac{4}{3}\right)x + (1-x)\right]} = x' \qquad \text{.....(6.1)}$$

(The factor 4/3 allows for the native laccase having 4 Cu as opposed to the 3 Cu in the T2D and T1Hg derivatives.)

$$\text{Native-corrected edge} = \frac{[\text{Edge} - x'(\text{Native edge})]}{1-x'} \qquad \text{.....(6.2)}$$

(The $(1-x')^{-1}$ factor scales the corrected edge back to 1. Table 6.2 shows which native edge was appropriate for which sample. Generally, the fully reduced

native edge NTFRD was used on fully reduced samples, and the fully oxidized native edge NTFOX was used on the rest.)

Where necessary (see Table 6.2 and next section), the reduced T2D and T1Hg samples were further corrected to "100% reduction" in the following way :

100% reduced corrected edge

$$= \left[(\text{Native - corrected edge}) - \frac{y}{(1-x)}(\text{Native - corrected fully oxidized edge}) \right] \frac{1-x}{1-z}$$

$$= \frac{[(1-x)(\text{Native - corrected edge}) - y(\text{Native - corrected fully oxidized edge})]}{1-z} \qquad \text{..(6.3)}$$

(Table 6.2 shows which fully oxidized edge was appropriate for which sample. T2D and T1Hg samples treated with sufficient excess of H_2O_2 were considered fully oxidized. These edges were themselves corrected for native before being used here. The $(1-x)/(1-z)$ factor renormalizes the corrected edge to 1.)

After carrying out these corrections, the edges were ready to be used in difference edge analysis.

(c) Construction of Difference Edges

In the discussion below, difference edges are denoted by "Δ" to distinguish them from regular edges.

Difference edges were made for two purposes : (i) for quantitation of the amount of reduced copper in a sample; (ii) for estimation of the possible geometry of Cu.

In Case (i), "100% reduced Δ standards" were first made by subtracting a 100% oxidized edge from a 100% reduced edge :

"100% reduced Δ standard" = "Corrected totally reduced edge"

– "Corrected totally oxidized edge" ....(6.4)

In this way, "100% reduced Δ standards" were made for native laccase, T2D laccase, T1Hg laccase and "T3 Cu" (see Table 6.3). Then, the amount of reduced Cu in a sample could be determined by subtracting the appropriate 100% oxidized edge from it and comparing the height of the resulting difference edge at 8984 eV to the height of the "100% reduced Δ standard".

In Case (ii), we used the criteria of height and edge slope at 8984 eV set forth in Table III of the paper by Kau, *et al.*[15] (reproduced in part here in Table 6.5) to estimate the geometry of Cu(I). Difference edges were made for this purpose by subtracting the same Cu(II) compound edge that they had used in their analysis, namely that of $[Cu_2(L_8\text{-}Et)(OAc)](ClO_4)_2$,[24] hereafter referred to as CUL2 :

"Difference edge Δ wrt CUL2" = "Corrected laccase edge" – CUL2 .....(6.5)

In some cases, say for T3 or T2 Cu, the difference edges had to be scaled up to "one full Cu". Here CUL2 could not be directly subtracted from the edge. Instead, the "difference edge Δ wrt CUL2" (wrt = "with respect to") had to be constructed by adding together two other difference edges, so :

"Difference edge Δ wrt CUL2" = q["Difference edge Δ wrt fully oxidized laccase"]
+ "Difference edge Δ of fully oxidized wrt CUL2"
.....(6.6)

where q is the factor needed to scale the difference edge back up to 1.

e.g., "ΔT3 Cu wrt CUL2" = 1.5("resting T2D"$_{corr}$ – "T2D + 60× H_2O_2"$_{corr}$)
+ ("T2D + 60× H_2O_2"$_{corr}$ – CUL2)

(The factor 1.5 was required because the T1 Cu is oxidized in both resting T2D and fully oxidized T2D, and so we produced a difference edge of only 2 out of 3 Cu when one was subtracted from the other.)

Results for Cases (i) and (ii) are given in Tables 6.3, 6.4 and 6.5.

An error analysis was carried out for the work reported in Section (C.1) below when it was published in 1990.[14] This analysis is repeated with some corrections in Appendix II. No error analysis was carried out for the work reported in Sections (C.2) and (C.3), but the errors are almost certainly greater, since the difference edge analysis proceeded through more steps of adjustment, subtraction and addition.

(C) Results and Discussion

(1) Reaction of T2D and T1Hg Laccase with Dioxygen

In 1987, the T1Hg derivative had not yet been much characterized, and we measured two samples, of resting T1Hg and H_2O_2-treated T1Hg, to determine the redox states of the various Cu ions. After due correction for native content as described above, and assuming that the H_2O_2-treated sample was 100% oxidized, we found that only 1 ± 8% of all Cu's in

the resting T1Hg were reduced (as compared with resting T2D laccase, in which T1 was 100% oxidized and T3 was 100% reduced, see Figure 6.3). This was an indication that the resting T1Hg, unlike resting T2D, might have completely reacted with dioxygen.

It remained to be seen how the fully reduced derivatives would react with dioxygen. So, in 1989, we collected two series of data on laccase, one each on T2D and T1Hg laccase at various times after exposing the fully reduced protein to air.

The T2D series consisted of fully reduced T2D (T2D1), T2D exposed to air for 15 minutes (T2D2) and T2D exposed for 63 hours (T2D3). A small amount of oxidation was observed between T2D1 and T2D2. This can be entirely accounted for by the rapid reoxidation of native laccase. After correction for native, it can be seen that T2D1 and T2D2 were both equally reduced (Figure 6.4). T2D3 was oxidized to a greater extent, but by no means totally oxidized. EPR and optical spectra showed that the T1 Cu in T2D3 was completely oxidized. Taking the difference edge of T2D3 with respect to H_2O_2-treated T2D (T26A), we calculated that 88 ± 14% of the T3 Cu were still reduced, even after 63 hours (Figure 6.4).

The T1Hg series consisted of a 90% reduced sample (MLRD) and a sample exposed to air for 30 minutes (MLOX). MLRD was corrected for native content and for 10% oxidation. Using corrected MLRD as the standard for 100% reduction, we found that the reoxidized sample (MLOX) contained 2 ± 11% reduced Cu (see Figure 6.5, Table 6.4).

It is clear that the oxidation of the T3 site in T2D laccase proceeds too slowly to be biologically relevant. On the other hand, all the Cu(I) ions in T1Hg laccase were completely oxidized within 30 minutes. This shows that the trinuclear T2+T3 site, rather than the T1+T3 assembly suggested by kinetic studies, is the minimal active site required for the multielectron reduction of dioxygen.[14]

(2) The T1Hg Laccase Oxygen Intermediate

It is known that, when O_2 binds to fully reduced native laccase, the T2 Cu is oxidized more slowly than the T1 and T3 Cu ions, and that when the reaction with O_2 is completed all the Cu are oxidized. We hoped that if we could freeze the reaction at the point when the oxygen intermediate was formed, we might catch the system in a state wherein the T2 Cu had not yet oxidized. We have not yet been able to achieve reproducible results for native laccase, but the kinetics of T1Hg laccase are somewhat slower than those of native laccase, and we have consistent results, obtained in 1991, for this oxygen intermediate.

Two corrections were applied to the O_2 intermediate spectra. The first was the correction for totally oxidized native laccase, as explained above. This correction was quite

small, being between 3.5% and 7%. However, there was 12–22% of oxidized T2 (see Table 6.2), with the proportion of oxidized T2 increasing with the time the sample had been exposed to air. This was considered to be due to protein that had passed through the O_2 intermediate stage and was now fully oxidized. The contribution of this state of T1Hg laccase was thus subtracted using fully oxidized T1Hg laccase (MLFOX, itself corrected for native laccase), in the manner shown in Equation 6.3.

All five O_2 intermediate samples appeared very similar, even before any corrections were applied, and it was clear that the majority of the Cu ions in the samples were oxidized (Figure 6.6). Indeed, when their heights at 8983.4 eV were measured against a "100% reduced T1Hg Δ standard", we found that only 13–17% of copper was in the Cu(I) state (Figure 6.7). However, this is only an overall number which assumes that all the Cu in T1Hg laccase are equivalent. For the true percentage of reduced Cu, we had to break down the contributions of the different Cu ions to the edge.

Based on our understanding of laccase chemistry, we assumed that 100% of the T3 Cu ions were oxidized, so that any difference between the edges of the O_2 intermediates and fully oxidized laccase would be due to reduced T2 Cu. We attempted to determine what percentage of T2 was reduced in the oxygen intermediates, by comparing difference spectra of the T1Hg O_2 intermediates ("ΔT1Hg O_2 int." = "T1Hg O_2 $int._{corr}$" – "$T1Hg(ox)_{corr}$") with a "100% reduced Δ standard" for reduced T2 ("ΔT2 Cu"). Unfortunately, "ΔT2 Cu" could not be directly obtained from the data we had collected. The best we could do was to construct the "ΔT2 Cu" standard out of other difference edges (which were in turn constructed according to Equation 6.4). Two ways were found for doing this :

$$\text{"}\Delta T2\ Cu\text{"}_1 = 4\text{"}\Delta T1_{red}T2_{red}2(T3_{red})\text{"} - 3\text{"}\Delta T1_{red}2(T3_{red})\text{"}$$

$$= 4(\text{"100\% reduced native } \Delta \text{ standard"}) - 3(\text{"100\% reduced T2D } \Delta \text{ standard"})$$

.....Method (i)

$$\text{"}\Delta T2\ Cu\text{"}_2 = 3[\text{"}\Delta T2_{red}2(T3)_{red}\text{"} - \text{"}\Delta 2(T3)_{red}\text{"}]$$

$$= 3[\text{"100\% reduced T1Hg } \Delta \text{ standard"}$$

$$- (\text{"Corrected resting T2D"} - \text{"Corrected fully oxidized T2D"})]$$

$$= 3[\text{"100\% reduced } \Delta T1Hg\text{"} - 2/3(\text{"100\% reduced } \Delta T3\ Cu\text{"})]$$

.....Method (ii)

The "ΔT2 Cu" difference edges constructed by these two methods have some similar features below 8986 eV, but also look considerably different at 8990 eV (Figure 6.8). A third "Δ standard" ("$\Delta T2\ Cu\text{"}_{avg}$) was also constructed by averaging these two. The peak

heights at 8983.4 eV of the O_2 intermediate difference edges were evaluated against all three standards, and by these criteria between 59% and 106% of T2 was reduced (see Tables 6.3, 6.4). However, the shapes of the "ΔT2 Cu" standards we constructed do not closely resemble the shapes of the O_2 intermediate difference edges, and so we should regard these percentages as a first guess at the redox state of T2 Cu in the T1Hg oxygen intermediate, rather than the final word.

Although the "ΔT2 Cu" standard is not very firm, it is nevertheless clear from visual inspection that all the T1Hg O_2 intermediate samples contain a small but reproducible amount of Cu(I), which possibly represent a reduced T2 Cu.

(3) Probable Geometry of T2 and T3 Cu in Laccase Samples

For estimation of Cu (I) geometry, difference edges with respect to CUL2 were constructed according to Equations 6.5 and 6.6. Since the "ΔT2 Cu" standards were constructed out of native, T1Hg and T2D edges, there was no clear candidate for the appropriate "difference edge Δ of fully oxidized wrt CUL2", and NTFOX was used. The difference edges thus constructed (see Figure 6.9) were then compared with Table III in the paper by Kau, *et al.* (reproduced in part here in Table 6.5). The results are given in Table 6.5. They show that the fully reduced native, T2D and T1Hg edges are remarkably similar, and they would fit into two of the possible geometries listed by Kau, *et al.* : (i) 3-coordinate, or (ii) (3 and 2+4)-coordinate (i.e., (3+3+2+4)-coordinate). The "ΔT3 Cu" difference edge fits well with a 2+3 Cu geometry, but the "ΔT2 Cu" we constructed does not fit into any of the categories of Cu(I) geometry surveyed by Kau, *et al.* This is not that surprising when we consider how many difference edges were pasted together to construct "ΔT2 Cu wrt CUL2", with small residuals furthermore being scaled up, magnifying the errors in the resultant edge.

We can thus conclude that the reduced T3 Cu ions in T2D laccase are probably 2+3-coordinated. Since the native, T2D and T1Hg laccase forms are (3 and 2+4)-coordinate (or its 3-Cu equivalent), and the T1 Cu (a blue copper site) is almost certainly 4-coordinate, it is possible that T2 is either 3- or 4-coordinate. However, we could not confirm this by examining our "ΔT2 Cu" standards.

(D) Conclusion

We have been able to show that reduced T1Hg is completely oxidized by dioxygen, while under the same conditions the T3 Cu in T2D laccase remain reduced. This shows that the trinuclear T2+T3 site, rather than the T1+T3 combination, is the minimal active site required for reduction of dioxygen.

We have also found that a small amount of Cu is reduced in the oxygen intermediate of T1Hg laccase. This reduced Cu is from chemical considerations most probably T2, but we were not able to confirm this because we did not have a reliable standard against which to measure the reduced Cu in the T1Hg O_2 intermediate.

The difficulty in obtaining a reliable "ΔT2 Cu" reduced standard shows that, in trying to determine one copper out of three, we are operating near the limit to which we can trust the method of difference edges. The amplitude of "ΔT2 Cu" is small enough so that errors in spline, noise and sample variation can and do distort it significantly, as attested by the fact that "ΔT2 Cu wrt CUL2" does not at all resemble any known class difference edges.

On the other hand, conclusions reached about the overall geometries of native, T2D, and T1Hg laccase (3-and-2+4-coordinate), as well as T3 Cu ions in T2D laccase (2+4-coordinate), can be held with some confidence, because the difference edges obtained are large in comparison to the errors they contain. This is also true of the conclusions reached in the study comparing the reactivities of T2D and T1Hg laccase with dioxygen.

Thus, the method of difference edge analysis of X-ray absorption spectra has proven extremely useful in elucidating details of the chemistry of laccase that would otherwise have been inaccessible to study, since it provides direct information on the averaged oxidation states and geometries of the Cu ions present in laccase. In our use of the difference edge method to study laccase, XAS edge studies complement information from more conventional forms of spectroscopy to an even greater extent than is usual in studies of metalloproteins. However, care should be taken not to push this method beyond what its inherent errors allow.

References

(1) Spira-Solomon, D. J.; Allendorf, M. D.; Solomon, E. I. *J. Am. Chem. Soc.* **1986**, *108*, 5318-5328.

(2) Allendorf, M. D.; Spira, D. J.; Solomon, E. I. *Proc. Natl. Acad. Sci. USA* **1985**, *82*, 3063-3067.

(3) Farver, O.; Goldberg, M.; Pecht, I. *Eur. J. Biochem.* **1980**, *104*, 71-77.

(4) Brändén, R.; Deinum, J.; Coleman, M. *FEBS Lett.* **1978**, *89*, 180-182.

(5) Brändén, R.; Deinum, J. *Biochim. Biophys. Acta* **1978**, *524*, 297-304.

(6) Brändén, R.; Deinum, J. *FEBS Lett.* **1977**, *73*, 144-146.

(7) Messerschmidt, A.; Ladenstein, R.; Huber, R.; Bolognesi, M.; Avigliano, L.; Petruzzelli, R.; Rossi, A.; Finazzi-Agró, A. *J. Mol. Biol.* **1992**, *224*, 179-205.

(8) Messerschmidt, A.; Rossi, A.; Ladenstein, R.; Huber, R.; Bolognesi, M.; Gatti, G.; Marchesini, A.; Petruzzelli, R.; Finazzi-Agró, A. *J. Mol. Biol.* **1989**, *206*, 513-529.

(9) Reinhammar, B. In *Copper Proteins and Copper Enzymes*; 1st ed.; R. Lontie, Ed.; CRC Press, Inc.: Boca Raton, Florida, 1984; Vol. III; pp 1-35.

(10) Andréasson, L.-E.; Reinhammar, B. *Biochim. Biophys. Acta* **1976**, *445*, 579-597.

(11) Andréasson, L.-E.; Brändén, R.; Reinhammar, B. *Biochim. Biophys. Acta* **1976**, *438*, 370-379.

(12) Andréasson, L.-E.; Brändén, R.; Malmström, B. G.; Vänngård, T. *FEBS Lett.* **1973**, *32*, 187-189.

(13) Clark, P. A.; Solomon, E. I. *J. Am. Chem. Soc.* **1992**, *114*, 1108-1110.

(14) Cole, J. L.; Tan, G. O.; Yang, E. K.; Hodgson, K. O.; Solomon, E. I. *J. Am. Chem. Soc.* **1990**, *112*, 2243-2249.

(15) Kau, L.-S.; Spira-Solomon, D. J.; Penner-Hahn, J. E.; Hodgson, K. O.; Solomon, E. I. *J. Am. Chem. Soc.* **1987**, *109*, 6433-6442.

(16) Spira, D. J.; Co, M. S.; Solomon, E. I.; Hodgson, K. O. *Biochem. Biophys. Res. Commun.* **1983**, *112*, 746-753.

(17) Woolery, G. L.; Powers, L.; Peisach, J.; Spiro, T. G. *Biochemistry* **1984**, *23*, 3428-3434.

(18) Klemens, A. S.; McMillin, D. R.; Tsang, H.-T.; Penner-Hahn, J. E. *J. Am. Chem. Soc.* **1989**, *111*, 6398-6402.

(19) Spira-Solomon, D. J.; Solomon, E. I. *J. Am. Chem. Soc.* **1987**, *109*, 6421-6432.

(20) Graziani, M. T.; Morpurgo, L.; Rotilio, G.; Mondovì, B. *FEBS Lett.* **1976**, *70*, 87-90.

(21) Morris, M. C.; Hauenstein, B. L., Jr.; McMillin, D. R. *Biochim. Biophys. Acta* **1983**, *743*, 389-393.

(22) Morie-Bebel, M. M.; Morris, M. C.; Menzie, J. L.; McMillin, D. R. *J. Am. Chem. Soc.* **1984**, *106*, 3677-3678.

(23) Stern, E. A.; Heald, S. M. *Rev. Sci. Instrum.* **1979**, *50*, 1579-1582.

(24) McKee, V.; Dagdigian, J. V.; Bau, R.; Reed, C. A. *J. Am. Chem. Soc.* **1981**, *103*, 7000-7001.

(25) Tan, G. O.; Hodgson, K. O.; Hedman, B.; Clark, G. R.; Garrity, M. L.; Sorrell, T. N. *Acta Cryst.* **1990**, *C46*, 1773-1775.

(26) Sorrell, T. N.; Malachowski, M. R.; Jameson, D. L. *Inorg. Chem.* **1982**, *21*, 3250-3252.

(27) Clegg, W.; Acott, S. R.; Garner, C. D. *Acta Cryst.* **1984**, *C40*, 768-769.

Table 6.1. Samples of laccase for which edge spectra were collected (continued on the next two pages).

Date collected	Name of data set	Description	Concentration, buffer, pH	Comments
Dec 1987	1ML01	Resting T1Hg laccase	3.2 mM Cu, pH 6.0, 100 mM potassium phosphate buffer	Photoreduction occurred; only the 1st scan was used
Dec 1987	2ML01	T1Hg laccase + H_2O_2	3.2 mM Cu, pH 6.0, 100 mM potassium phosphate buffer	Photoreduction occurred; only the 1st scan was used
Dec 1987	1T2D*	Fully reduced T2D		Analysis not reported here
Dec 1987	2T2D*	T2D exposed to air for 15 minutes		Analysis not reported here
Dec 1987	2T2D*	T2D exposed to air for 3.5 days		Analysis not reported here
Mar 1989	MLOX	Fully reduced and reoxidized T1Hg	4.5 mM Cu, pH 6.0, 100 mM potassium phosphate buffer	N_2 in the Lytle detector
Mar 1989	MLRD	Fully reduced T1Hg	4.5 mM Cu, pH 6.0, 100 mM potassium phosphate buffer	N_2 in the Lytle detector
Mar 1989	NLRD	Fully reduced native	3.6 mM Cu, pH 6.0, 100 mM potassium phosphate buffer	N_2 in the Lytle detector
Mar 1989	T2D1	Fully reduced T2D	3.3 mM Cu, pH 6.0, 100 mM potassium phosphate buffer	N_2 in the Lytle detector
Mar 1989	T2D2	T2D exposed to air for 15 minutes	3.3 mM Cu, pH 6.0, 100 mM potassium phosphate buffer	N_2 in the Lytle detector
Mar 1989	T2D3	T2D exposed to air for 63 hours	3.3 mM Cu, pH 6.0, 100 mM potassium phosphate buffer	N_2 in the Lytle detector

* — Too much reductant (i.e., 5 eq. ascorbic acid) was added to these samples, putting their reliability in doubt.

Table 6.1. Samples of laccase on which edge spectra were collected (continued from the previous page, continued next page)

Date collected	Name of data set	Description	Concentration, buffer, pH	Comments
Apr 1990	MLEX	T1Hg reduced and reoxidized	10.2 mM Cu, pH 6.0, 50% glycerol, 50% 200 mM potassium phosphate buffer	EXAFS sample, 13 good scans meaaured on BL 4-2, ~20% photoreduction
Apr 1990	MLOI‡	T1Hg O_2 intermediate	2.2 mM Cu, pH 6.0, 100 mM potassium phosphate buffer	Analysis not reported here
Apr 1990	NLO1†	Native O_2 intermediate #1, frozen 5.6 s after mixing	~4 mM Cu, pH 7.4, 100 mM potassium phosphate buffer	Detailed analysis not done
Apr 1990	NLO2†	Native O_2 intermediate #2, frozen 3.9 s after mixing	~4 mM Cu, pH 7.4 100 mM potassium phosphate buffer	Detailed analysis not done
Jun 1991	MLFRD	Fully reduced T1Hg	3.5 mM Cu, pH 7.4, 100 mM potassium phosphate buffer	
Jun 1991	MLFOX	Fully oxidized T1Hg	1.8 mM Cu, pH 7.4, 100 mM potassium phosphate buffer	
Jun 1991	O21ML	T1Hg O_2 intermediate #1 — exposed to O_2 for 8 minutes	1.8 mM Cu, pH 7.4, 100 mM potassium phosphate buffer	
Jun 1991	O22ML	T1Hg O_2 intermediate #2 — exposed to O_2 for 27 minutes	1.8 mM Cu, pH 7.4, 100 mM potassium phosphate buffer	
Jun 1991	NTFRD	Fully reduced native	7–8 mM Cu, pH 7.4, 50% ethylene glycol, 50% potassium phosphate buffer	
Jul 1991	NTFOX	Fully oxidized native (with 30× H_2O_2)	7–8 mM Cu, pH 7.4, 50% ethylene glycol, 50% potassium phosphate buffer	

‡ — This edge was different from edges of T1Hg O_2 intermediates run the following year.

† — Reproducible edges of native laccase O_2 intermediates could not be obtained.

Table 6.1. Samples of laccase on which edge spectra were collected (continued from the previous pages).

Date collected	Name of data set	Description	Concentration, buffer, pH	Comments
Jul 1991	O21NT†	Native O_2 intermediate #1, rapid mix, 6–8 s	2.4 mM Cu, pH 7.4, 50% ethylene glycol, 50% 100 mM potassium phosphate buffer	Detailed analysis not done
Jul 1991	O22NT†	Native O_2 intermediate #2, rapid mix, 8–10 s	2.4 mM Cu, pH 7.4, 50% ethylene glycol, 50% 100 mM potassium phosphate buffer	Detailed analysis not done
Jul 1991	O23NT†	Native O_2 intermediate #3, partially oxidized past the intermediate stage	2.4 mM Cu, pH 7.4, 50% ethylene glycol, 50% 100 mM potassium phosphate buffer	Detailed analysis not done
Oct 1991	ML11	T1Hg O_2 intermediate #1 — exposed to O_2 for 9 minutes	2.1 mM Cu, pH 7.4, 20% glycerol, 80% 100 mM potassium phosphate buffer	Photoreduction occurred; only the 1st scan was used
Oct 1991	ML21	T1Hg O_2 intermediate #1 — exposed to O_2 for 27 minutes	2.1 mM Cu, pH 7.4, 20% glycerol, 80% 100 mM potassium phosphate buffer	Photoreduction occurred; only the 1st scan was used
Oct 1991	ML31	T1Hg O_2 intermediate #1 — exposed to O_2 for 90 minutes	2.1 mM Cu, pH 7.4, 20% glycerol, 80% 100 mM potassium phosphate buffer	Photoreduction occurred; only the 1st scan was used

† — Reproducible edges of native laccase O_2 intermediates could not be obtained.

Table 6.2. Edge spectra of laccase used in difference edge analysis, with corrections (see text) for native content and oxidation of samples as indicated (continued next page).

Name of data set	Description	Percentage of native ($100x$)	Data file used for native correction	Percentage of oxidized Cu† ($100z$)	Data file used for oxidation correction£
NTVL‡	Resting native laccase	------	------	100 (T1, T2) 78 (T3)[15]	------
NT30‡	Native + 30× H_2O_2 (fully oxidized)	------	------	100	------
T2DS‡	Resting T2D laccase	7–8	NTVL	100 (T1) 98 (T3)[15]	------
T26A‡	T2D + 60× H_2O_2 (fully oxidized)	7–8	NT30§, NTFOX¤	100 (T1) 0 (T3)[15]	------
1ML01	Resting T1Hg laccase	15	NTVL	See Table 6.4	------
2ML01	T1Hg + 30× H_2O_2	15	NT30	100	------
NLRD	Fully reduced native	------	------	~4 (T2)	------
MLOX	Fully reduced and reoxidized T1Hg	4–7 (T1)	NTVL	See Table 6.4	------
MLRD	Fully reduced T1Hg	4–7 (T1)	NLRD	10 (T2) T3 assumed to be 10	2ML01
T2D1	Fully reduced T2D	10 (AA)	NTFRD	~0 (T1)	------
T2D2	T2D exposed to air for 15 minutes	10 (AA)	NTVL	15–20 (T1)	------
T2D3	T2D exposed to air for 63 hours	10 (AA)	NTVL	100 (T1)	------

† — the type of Cu on which these figures are based is shown in brackets. Oxidized T1 was measured either by optical absorption spectra or by EPR, usually the former, oxidized T2 was measured by EPR alone, and oxidized T3 by optical spectra alone. AA : atomic absorption

£ — These data sets were themselves first corrected for native content

‡ — These data sets were collected by previous workers

§ — This data set was used where corrected T26A (denoted $T26A_{corr1}$) was subsequently subtracted from T2DS for "T3 Cu" difference edge (see text, Table 6.3), so that all the data going into the difference edge was collected at the same time (Nov 1983).

¤ — This data set was used where corrected T26A (denoted $T26A_{corr2}$) was subsequently subtracted from the 1989 T2D edges.

Table 6.2. Edge spectra of laccase used in difference edge analysis, with corrections (see text) for native content and oxidation of samples as indicated (continued from previous page).

Name of data set	Description	Percentage of native (100x)	Data set used for native correction	Percentage of oxidized Cu† (100z)	Data set used for oxidation correction£
NTFRD	Fully reduced native	------	------	0	------
NTFOX	Native +30× H_2O_2	------	------	100	------
MLFRD	Fully reduced T1Hg	7 (T1)	NTFRD	0 (T2)	------
MLFOX	Fully oxidized T1Hg	7 (T1)	NTFOX	100 (T2)	------
O21ML	T1Hg O_2 intermediate #1 — exposed to O_2 for 8 minutes	7 (T1)	NTFOX	22.4 (T2)	MLFOX
O22ML	T1Hg O_2 intermediate #2 — exposed to O_2 for 27 minutes	7 (T1)	NTFOX	21.4 (T2)	MLFOX
ML11	T1Hg O_2 intermediate #1 — exposed to O_2 for 9 minutes	3.5 (T1)	NTFOX	12 (T2)	MLFOX
ML21	T1Hg O_2 intermediate #1 — exposed to O_2 for 27 minutes	3.5 (T1)	NTFOX	15 (T2)	MLFOX
ML31	T1Hg O_2 intermediate #1 — exposed to O_2 for 90 minutes	3.5 (T1)	NTFOX	18 (T2)	MLFOX

£ — These data sets were themselves first corrected for native content

† — the type of Cu on which these figures are based is shown in brackets. Oxidized T1 was measured either by optical absorption spectra or by EPR, usually the former, oxidized T2 was measured by EPR alone, and oxidized T3 by optical spectra alone. AA : atomic absorption

Table 6.3. Difference edges constructed from corrected laccase edges — "100% reduced Δ standards".

No.	Description	Edge data sets used	Height at 8984 eV	% of Cu reduced
I	100% reduced T1Hg, 1989	$MLRD_{corr} - 2ML01_{corr}$	0.4496	100
II	100% reduced T1Hg, 1991	$MLFRD_{corr} - MLFOX_{corr}$	0.4787 0.5000†	100
III	100% reduced native, 1989	NLRD – NT30	0.4524	100
IV	100% reduced native, 1991	NTFRD – NTFOX	0.4234	100
V	100% reduced T2D, 1989	$T2D1_{corr} - T26A_{corr2}$	0.4751	100
VI	100% reduced "T3 Cu"	$1.5(T2DS_{corr} - T26A_{corr1})$	0.6188	100
VII	100% reduced "T2 Cu"$_1$	4×[III] – 3×[IV]	0.2582 0.3184†	100
VIII	100% reduced "T2 Cu"$_2$	3×[II] – 2×[V]	0.2037 0.2415†	100
IX	100% reduced "T2 Cu"$_{avg}$	0.5"T2 Cu"$_1$ + 0.5"T2 Cu"$_2$	0.2319 0.2831†	100

† — This difference edge height was measured at 8983.4 eV (where the 100% reduced T1Hg standard is maximum) for greater accuracy.

Table 6.4. Difference edges constructed from corrected laccase edges — amount of reduced Cu is determined from standards in Table 6.3.

Description	Edge data sets used	Height at 8984 eV	% of Cu reduced‡
T2D exp. 15 min.	$T2D2_{corr} - T26A_{corr1}$	0.4776	100 wrt [V]
T2D exp. 63 hrs.	$T2D3_{corr} - T26A_{corr1}$	0.3628	76 wrt [V], 88 wrt 2/3[VI]
Resting T1Hg	$1ML01_{corr} - 2ML01_{corr}$	0.0060	1 wrt [I]
Reduced and reoxidized T1Hg	$MLOX_{corr} - 2ML01_{corr}$	0.0082	2 wrt [I]
T1Hg O_2 int. #1	$O21ML_{corr} - MLFOX_{corr}$	0.06303†	13 wrt [II] 59 wrt 1/3[VII] 78 wrt 1/3[VIII] 67 wrt 1/3[IX]
T1Hg O_2 int. #2	$O22ML_{corr} - MLFOX_{corr}$	0.07564†	15 wrt [II] 71 wrt 1/3[VII] 94 wrt 1/3[VIII] 80 wrt 1/3[IX]
T1Hg O_2 int. #3	$ML11_{corr} - MLFOX_{corr}$	0.07730†	15 wrt [II] 73 wrt 1/3[VII] 96 wrt 1/3[VIII] 82 wrt 1/3[IX]
T1Hg O_2 int. #4	$ML21_{corr} - MLFOX_{corr}$	0.08498†	17 wrt [II] 80 wrt 1/3[VII] 106 wrt 1/3[VIII] 90 wrt 1/3[IX]
T1Hg O_2 int. #5	$ML31_{corr} - MLFOX_{corr}$	0.08498†	17 wrt [II] 80 wrt 1/3[VII] 106 wrt 1/3[VIII] 90 wrt 1/3[IX]

† — These difference edge heights were measured at 8983.4 eV (where the 100% reduced T1Hg standard is maximum) for greater accuracy.

‡ -- "wrt" = "with respect to"

Table 6.5. Normalized difference edge energies and amplitudes at peak maxima (the first part is from Table III in the Cu edge analysis paper by Kau, *et al.*[15]).

Coordination Number	Energy† (eV)	Amplitude†	Slope§ (units/eV)
2	8983.6–84.2	0.99 ± 0.13	-0.20 to -0.45
3	8983.1–83.8	0.54 ± 0.08	0.0 to -0.06
4	8984.7–86.3	0.49 ± 0.11	0.10 to 0.08
covalent Cu(II)	8985.8–88.0	0.42 ± 0.05	0.12 to 0.09
2 + 3	8983.6–84.2	0.75 ± 0.10	-0.07 to -0.11
2 + 4	8983.6–84.4	0.65 ± 0.07	-0.05 to -0.08
3 + 4	8983.7–85.8	0.48 ± 0.10	0.03 to 0.04
3 and 2 + 4	8983.1–84.4	0.59 ± 0.13	0.0 to -0.08
2 + 3 and 2 + 4	8983.6–84.4	0.71 ± 0.13	-0.05 to -0.11
100% reduced native laccase£	8983.6	0.58	-0.047◊
100% reduced T2D laccase£	8983.7	0.57	-0.045◊
100% reduced T1Hg laccase£	8983.6	0.58	-0.044◊
100% reduced "T3 Cu"‡	8983.7	0.72	-0.08
100% reduced "T2 Cu"$_1$‡	8982.5	0.46	-0.08
100% reduced "T2 Cu"$_2$‡	8982.8	0.39	-0.02
100% reduced "T2 Cu"$_{avg}$‡	8982.8	0.43	-0.05

† — at peak maxima

§ — The slope is defined as the best fit line extending between 8984 and 8986 eV of the spectrum and the unit is (normalized difference edge amplitude)/(eV)

£ — This difference edge is constructed by direct subtraction of the edge of the Cu(II) model compound $[Cu_2(L_8\text{-Et})(OAc)](ClO_4)_2$[24] (CUL2), as described in Equation 6.5.

‡ — This difference edge is scaled up to "one full Cu" and is with respect to the Cu(II) model compound $[Cu_2(L_8\text{-Et})(OAc)](ClO_4)_2$[24] (CUL2), as described in Equation 6.6.

◊ — The extra decimal place is included to reveal the similarity of the slopes obtained for the three different forms of laccase.

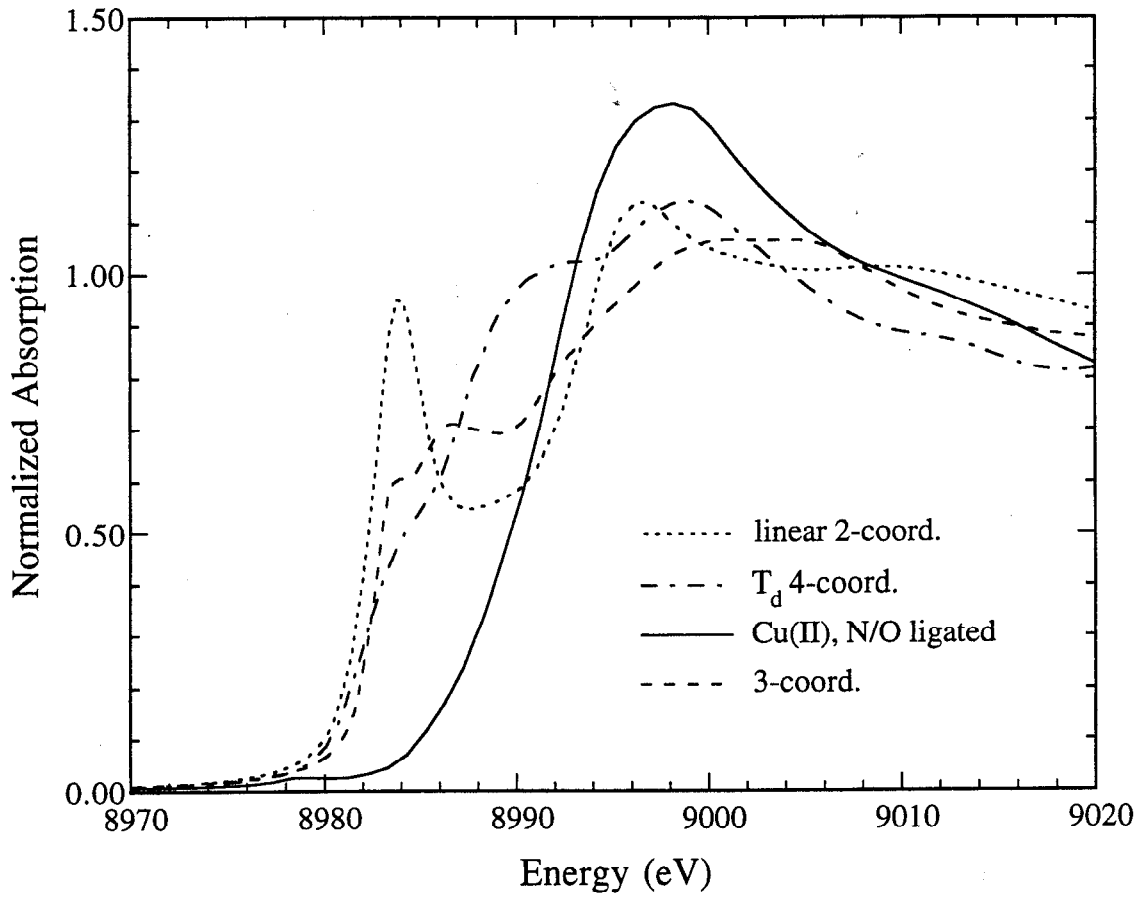

Figure 6.1. X-ray absorption edges of Cu(I) model compounds : Cu(I)(*N*-methylimidazole)$_2$BF$_4$,[25] linear 2-coordinate (- - - -); [Cu(I)$_2$(mxyN$_6$)](BF$_4$)$_2$,[26] 3-coordinate (– – -); Cu(I)(*N*-methylimidazole)$_4$ClO$_4$,[27] tetrahedral 4-coordinate (— - — - —); and [Cu$_2$(L$_8$-Et)(OAc)](ClO$_4$)$_2$,[24] Cu(II) N/O-ligated (CUL2) (——).